Melting and structural transformations of carbonates and hydrous phases in Earth's mantle

by

Zeyu Li

A dissertation submitted in partial fulfillment
of the requirements for the degree of
Doctor of Philosophy
(Geology)
in the University of Michigan
2015

Doctoral Committee:

Associate Professor Jie Li, Chair
Professor Udo Becker
Professor Edwin A. Bergin
Professor Rebecca A. Lange
Professor Peter E. Van Keken

To Menglian, my mum and dad

Acknowledgements

First I would like to sincerely thank my advisor, associate professor Jie Li. During my Ph.D study, she supports and encourages me all the time, constantly saving me from getting lost. I would also like to thank Professors Edwin Bergin, Udo Becker, Rebecca Lange and Peter van Keken for serving on my dissertation committee. Especially I would like to thank Dr. Hongwu Xu providing me with the chance and financial support to collaborate with them on hydrous mineral study.

In addition, I appreciate the collaborations and student life spent with Jiachao Liu, Elisabeth Tanis and all the other peer graduate students. I also thank previous or current faculties Dr. Bin Chen, Dr. Fuxiang Zhang and Dr. Gordon Moore for their helps with my experiments. I also thank staff Anne Hudon and Nancy Kingsbury for their kind helps with academic affairs. I spent six wonderful years in the University of Michigan with all the professors, fellow students and friends here, I really appreciate everything the University offered to me.

At last, I'd like to thank my girlfriend Menglian Zhou and my Mum and Dad. Because of their love and support, I can make to this step.

Table of Contents

List of Tables

List of Figures

Abstract

This dissertation addresses questions about carbon and hydrogen transport and storage in the mantle through experimental investigations of the melting behaviors of carbonates under high pressure and phase stability of dense hydrous germanate.

In Chapter II, a new technique was developed to measure melting temperatures at high pressures by monitoring the sudden change of capacitive current through ionic compounds upon melting.

In Chapter III, the melting curve of NaCl up to 20 GPa was measured using the capacitive current technique. New results are consistent with previous data on melting temperature of NaCl up to 6.5 GPa, thus validating the accuracy of capacitive current based measurement.

In Chapter IV, we measured the melting curve of $CaCO_3$ between 3 and 22 GPa. The melting temperature of $CaCO_3$ was found to decrease between 7 and 15 GPa and then increase with pressure between 15 and 21 GPa. The negative melting slope was attributed to the melt/solid density crossover at 7 GPa and the positive melting slope at higher pressures can be explained by calcite V to aragonite phase transition at 15 GPa. The melting curve of $CaCO_3$ may cross a hot adiabatic geotherm at the transition zone depth in an upwelling setting, producing carbonate melt in the transition zone.

In Chapter V, the melting curves of two more carbonates, Na_2CO_3 and K_2CO_3, were measured between 3 and 20 GPa. Above 9 GPa the melting temperature of K_2CO_3 was found to increase with pressure at a much higher rate than Na_2CO_3. Results from high pressure *in situ* X-

ray diffraction experiments indicated two solid phase transitions of K_2CO_3 at ~3 and ~9 GPa, respectively.

In Chapter VI, the stability of three new dense hydrous magnesium germanate (DHMG) minerals were reported on the basis of phase equilibrium experiments using i*n situ* synchrotron X-ray diffraction and hydrothermal diamond anvil cell. One of them was determined as germanate analogue of phase D, and the other two were likely germanium analogues of superhdrous B and phase H.

CHAPTER I

Introduction

Volatile elements, including hydrogen, carbon, sulfur, fluorine, chlorine play important roles in the Earth's mantle processes. Even at low concentrations, their presence lowers the solidus temperature of mantle rock and induces melting in the mantle. Without them, there would be no arc volcanism that constantly reshapes the Earth. The fates of these volatile elements, especially carbon and hydrogen, in the deep mantle are still not well understood. In this dissertation I will address the questions of carbon and hydrogen storage in the mantle from high pressure melting and phase equilibrium experiments.

1.1 Deep carbon cycle

Carbon is one of the most important volatiles in the mantle. Besides participating in the carbon cycle in exosphere which is crucial to the Earth's climate and life activities, carbon is moving in another deep cycle on the planetary level. Carbon enters the Earth's interior though subduction in forms of organics in seafloor sediments or carbonates in oceanic basalts (Alt et al. 2012). When the subduction slab goes deep into the mantle and is heated up, some of the carbon escapes from the slab and goes into a highly mobile fluid phase in the form of CO_2, CO and CH_4 (Manning et al. 2013) along with H_2O. Some carbonates in

the slab dissolve into the fluid (Ague and Nicolescu, 2014) and eventually get back to the atmosphere through volcanism (Dasgupta and Hirschmann, 2010). Some of the carbon in the form of carbonates will survive in the slab (e.g. Poli et al. 2009; Conolly 2005) and continue to dive deeper into the mantle. At certain depths, if the slab is warmed up and reaches the solidus temperature of carbonated mantle rock, melting may happen and creates carbonatitic melt, a small portion of which ascends fast to the Earth's surface, forming kimberlite and carbonatite (Jones et al. 2013). The solidus temperature varies with alkaline content and Ca number (molar Ca/(Ca+Mg+Fe)%) (Dasguputa et al. 2005). The solidus of carbonated eclogite with a normal composition seems higher than the temperatures of most of the Earth's subduction systems (Dasguputa and Hirschmann, 2010), which indicates carbonates can enter the transition zone and lower mantle. With a low oxygen fugacity in the lower mantle (Frost and McCammon, 2008), carbonates may get reduced to graphite or diamond (Rohrbach and Schmidt, 2011; Stagno et al. 2013). Carbon in the lower mantle can be brought back to a shallower depth by upwelling mantle. With increasing oxygen fugacity upon ascending, diamonds may be oxidized back to carbonates and experience melting (Rohrbach and Schmidt, 2011; Stagno et al. 2013). Some questions about deep carbon cycle are still unknown, such as carbon exchange between core and mantle, the interaction between hydrogen and carbon in deep mantle, carbon bearing phases in lower most mantle and etc. Phase equilibrium experiment is one of the most widely used approaches to study melting of carbonated mantle rock. But large discrepancies exist among those results from phase equilibrium experiments, especially the solidus temperatures of carbonated mantle rocks (Kiseeva et al. 2013), which lead to different scenarios of deep carbon cycle. The discrepancies could be caused by the composition variations of starting materials, which

reflects the complexities of the system. Another approach to study melting of carbonated mantle rock is thermodynamic modeling (e.g. Kerrick and Connolly, 2001; Connoll 2005). By building a thermodynamic model which is calibrated upon results of phase equilibrium experiments, one can predict solidus temperature and mineral assemblage under any given starting composition and pressure. However, a comprehensive thermodynamic model requires thermodynamic parameters of every species in the system, such as heat capacity, enthalpy of fusion, compressibility, thermal expansibility, etc. Even though there are relatively complete models for silicate melting (e.g. Ghiorso et al. 2002), carbonates still lack crucial data such as compressibility of their melts to be incorporated into the model. By addressing this problem, we started to work on end member carbonates, $CaCO_3$, Na_2CO_3, K_2CO_3, which are of the most important carbonates in the mantle. By studying the melting curves of these end member carbonates, the compressibility of each species can be calculated from the slope of the curve by method such as fusion curve analysis (Ghiorso, 2004). The melting curve can provide other information, e.g., the sub-melting solid phase transition can be discovered from the sudden change of melting curve slope.

To accurately measure melting temperatures of carbonates under upper mantle condition, we developed a new technique for high pressure melting temperature measurement by monitoring sudden change of capacitive current through the sample upon melting. Details about this new technique are reported in Chapter II. This new technique is an *in situ* approach and the measurement is non-destructive to the sample, so the melting curve of an ionic crystal over the entire pressure range of the upper mantle can be measured in a single high pressure experiment. Besides its efficiency, this technique also has advantages such as high signal/noise ratio and simple implementation.

In Chapter III, the melting curve of NaCl up to ~20 GPa is reported using the new technique described in Chapter II. The results from our measurement closely resemble previous data on melting temperature of NaCl up to 6.5 GPa (Clark 1959; Pistorius 1966; Akella et al. 1969), which validates the accuracy of this capacitive current based measurement. New data about melting temperature of NaCl up to ~20 GPa was acquired and several melting equations were fitted the new data set.

In Chapter IV, the melting curve of $CaCO_3$ is reported up to ~22 GPa using the new technique described in chapter II. The new results densely cover the pressure range from ~3 to ~22 GPa. Two features of the $CaCO_3$ melting curve were discovered for the first time: the melting curve reached a local maximum at ~7 GPa and started to decrease slowly until 15 GPa, which we interprets as the melt/solid density crossover at 7 GPa; the melting curve has a sudden change in slope at 15 GPa from decreasing to increasing with higher pressure, which we interprets as the solid/melt density overturn caused by calcite V to aragonite phase transition. The melting curve of $CaCO_3$ keeps within 1700-1800 °C over 4 -20 GPa, and may cross over with a hot adiabatic geotherm at the transition zone depth in a upwelling setting, indicating carbonate induced melting in the transition zone.

In Chapter V, the melting curves of two more carbonates, Na_2CO_3 and K_2CO_3, are reported up to ~20 GPa using the same method described in Chapter II. With a similar structure and chemical properties, the Na_2CO_3 and K_2CO_3 were expected to behave similarly, but our results show that even starting with similar melting temperature below 3GPa, the melting temperature of Na_2CO_3 increases at a much slower rate than K_2CO_3. The melting temperature of K_2CO_3 based on our measurement has caught up with that of $MgCO_3$ (Katsura and Ito, 1990) at ~ 17 GPa. The melting curve of K_2CO_3 shows a deflection point at ~ 9 GPa, which may indicate a sub-melting

solid transition. In order to further investigate the high pressure polymorphs of K_2CO_3 suggested by the deflection of its melt curve, *in situ* X-ray diffraction experiments with laser heated diamond anvil cells were conducted. Two new phase transitions of K_2CO_3 at ~ 3 GPa and ~9 GPa are reported.

1.2 Deep hydrogen cycle

Hydrogen enters the Earth interior through subduction, in the form of H_2O (Peacock, 1990). Most of pore H_2O in the ocean sediment and crust is lost in the initial dehydration in the subduction prism (Rüpke et al. 2004). The chemically bounded water, in the form of serpentine, can reach a depth of ~ 200 km and a temperature of ~600 °C (Rüpke et al. 2004) before deserpentinization, releasing the chemically bounded water, which are commonly believed to trigger arc melting. Some serpentine will survive the deserpentinization (Van Keken et al. 2002), and experiences a series of phase transitions towards higher pressure and higher temperature. These phases are a group of minerals called the dense hydrous magnesium silicates (DHMS), such as phase A, phase B (Ringwood and Major, 1967), phase superhydrous B (Gasparik, 1990), phase D (Liu, 1986), phase E (Kudoh et al. 1993), phase H (Nishi et al. 2014) and δ phase (Suzuki et al. 2000). These DHMS can carry water all the way to the lower mantle (Ohtani et al. 2014). The nominally anhydrous minerals, wadsleyite and ringwoodite, were found to able to contain up to 1% H_2O in their structures (Smyth, 1987; Kohlstedt et al. 1996). The recent discovery of diamond inclusion containing ringwoodite with up to 1% wt H_2O (Pearson et al. 2014) suggested that the transition zone is the largest water reservoir inside the Earth.

Research interests on deep water cycle focus on phase equilibrium (e.g. Irifune et al. 1998; Ohtani et al. 2000; Shieh et al. 2000; Angel et al. 2001), crystal structures (e.g. Yang et al. 1997;

Bindi et al. 2014) and physical properties (e.g. Sanchez-Valle et al. 2008; Mao et al. 2012) of those hydrous minerals stable in the mantle condition. One of the problems that some of these studies faced was the limited sample volume. Because most of these DHMS minerals require higher than 10 GPa to synthesize, and phase D and phase H even require more than 20 GPa (Ohtani et al. 2014), the sample volume which can be acquired through high pressure syntheses is limited to only a few micrograms. Some experimental techniques, such as neutron diffraction and calorimetry, require at least tens of micrograms of sample to work. Germanate analogues of DHMS can be used to circumvent this problem. With similar crystal structures and properties, hydrous magnesium germanates (DHMG) minerals can be synthesized with much lower pressure (Thomas et al. 2008). In Chapter VI, the stability of several DHMG minerals based on phase equilibrium experiments are reported, one of which has been determined to be germanate analogue of phase D. The acquired pressure and temperature stability map of those DHMG can be the guide for future syntheses of DHMG.

References

Ague, J.J., and Nicolescu, S. (2014) Carbon dioxide released from subduction zones by fluid-mediated reactions, Nature Geosciences, 7, 355-360.

Akella, J., Vaidya, S. N., and Kennedy, G. C., (1969) Melting of sodium chloride at pressures to 65 kbar. Physical Review, 185, 1135–1140.

Angel, R.J., Forst, D.J., Ross, N.L., and Hemley, R.J. (2001) Stabilities and equations of state of dense hydrous magnesium silicates. Physics of the Earth and Planet Interiors,127, 181-196.

Bindi, L., Nishi, M., Tsuchiya, J., and Irifune, T. (2014) Crystal chemistry of dense hydrous magnesium silicates: The structures of phase H, $MgSiH_2O_4$, synthesized at 45 GPa and 1000 °C. American Mineralogist, 99, 1802-1805.

Clark, S. P. J. (1959) Effect of pressure on the melting points of eight alkali halides. Journal of Chemical Physics, 31, 1526-1531.

Connlly J.A.D. (2005) Computation of phase equilibria by linear programming: a tool for geodynamic modeling and its application to subduction zone decarbonation. Earth Planetary Science Letters, 236, 524-541.

Dasgupta, R., Hirschmann, M.M., and Dellas, N. (2005) The effect of bulk composition on the solidus of carbonated eclogite from partial melting experiments at 3 GPa, Contributions to Mineralogy and Petrology, 149, 288-305.

Dasgupta, R., and Hirschmann, M. M. (2010) The deep carbon cycle and melting in Earth's interior. Earth and Planetary Science Letters (Frontiers), 298, 1-13.

Forst, D.J., and McCammon, C.A. (2008) The redox state of the Earth's mantle. Annual Review of Earth and Planetary Sciences, 36, 389-420.

Gasparik, T. (1990) Phase relations in the transition zone. Journal of Geophysical Research, 95, 1575 l-15769.

Ghiorso, M.S. (2004) An equation of state for silicate melts. III analysis of stoichiometric liquids at elevated pressure: shock compression data, molecular dynamics simulations and mineral fusion curves. American Journal of Science, 304, 752-810.

Ghiorso M.S., Hirschmann, M.M, Reiners, P.W., and Kress, V.V. III (2002) The pMELTS: A revision of MELTS for improved calculation of phase relations and major element partitioning related to partial melting of the mantle to 3 GPa. Geochemistry Geophysics Geosystems, 3, 10.1029/2001GC000217.

Irifune, T., Kubo, N., Isshiki, M., and Yamasaki, Y. (1998) Phase transformations in serpentine and transportation of water into the lower mantle. Geophysical Research Letters, 25, 203-206.

Jones, A.P., Genge, M., and Carmody, L. (2013) Carbonate melts and carbonatites. Reviews in Mineralogy & Geochemistry, 75, 289-322.

Katsura, T., and Ito, E. (1990) Melting and subsolidus phase relations in the $MgSiO_3$–$MgCO_3$ system at high pressures: implications to evolution of the Earth's atmosphere. Earth and Planetary Science Letters, 99, 110–117.

Kerrick, D.M., and Connolly J.A.D. (2001) Metamorphic devolatilization of subducted marine sediments and transport of volatiles into the Earth's mantle. Nature, 411, 293-296.

Kiseeva, E.S., Litasov K.D., Yaxley, G.M., Ohtani, E., and Kamenetsky, V.S. (2013) Melting and phase relations of carbonated eclogite at 9-21 GPa and the petrogenesis of alkali-rich melts in the deep mantle.

Kohlstedt, D. L., Keppler, H. & Rubie, D. C. (1996) Solubility of water in the α, β and γ phases of $(Mg,Fe)_2SiO_4$. Contributions to Mineralogy Petrology, 123, 345–357.

Kudoh, Y., Finger, L.W., Hazen, R.M., Prewitt, C.T., Kanzaki, M., and Veblen, D.R. (1993) Phase E: a high pressure hydrous silicate with unique crystal chemistry. Physics and Chemistry of Minerals, 19, 357- 360.

Liu, L. (1986) Phase transformations in serpentine at high pressures and temperatures and implications for subducting lithosphere. Physics of the Earth and Planetary Interiors, 42, 255-262.

Manning, C.E., Shock, E.L., and Sverjensky, D.A. (2013) The chemistry of carbon in aqueous fluids at crustal and upper-mantle conditions: experimental and theoretical constraints. Reviews in Mineralogy and Geochemistry, 75, 109-148.

Mao, Z., Lin, L., Jacobsen, S.D., Duffy, T.S., Chang, Y., Smyth, J.R., Forst, D.J., Hauri, E.H., Prakapenka, V.B. (2012) Sound velocities of hydrous ringwoodite to 16 GPa and 673 K. Earth and Planetary Science Letters, 331-332, 112-119.

Nishi, M., Irifune, T., Tsuchiya, J. Tange, Y., Nishihara, Y. Fujino, K., and Higo, Y. (2014) Stability of hydrous silicate at high pressures and water transport to the deep lower mantle, Nature Geoscience, 7, 224-227.

Ohtani, E., Mizobata, H., and Yurimoto, H. (2000) Stability of dense hydrous magnesium silicate phases in the systems Mg_2SiO_4-H_2O at pressures up to 27 GPa, 27, 533-544.

Ohtani, E., Amaike, Y., Kamada, S., Sakamaki, T., and Hirao, N. (2014) Stability of hydrous phase H $MgSiO_4H_2$ under lower mantle conditions. Geophysical Research Letters, 41, 8283-8287.

Pearson, D.G., Brenker, F.E., Nestola, F., McNeill, J., Nasdala, L., Hutchison, M.T., Matveev, S., Mather, K., Silversmit, G., Schmitz, S., Vekemans, B., and Vincze, L. (2014) Hydrous mantle transition zone indicated by ringwoodite included within diamond. Nature, 507, 221-224.

Pistorius, C. W. F. T. (1966) Effect of pressure on the melting points of the sodium halides. Journal of Chemical Physics, 45, 3513-3519.

Poli, S., Franzolin, E., Fumagalli, P., and Crottini, A. (2009) The transport of carbon and hydrogen in subducted oceanic crust: An experimental study to 5 GPa. Earth and Planetary Science Letters, 278, 350-360.

Ringwood, A.E., and Major, A. (1967) High-pressure reconnaissance investigations in the system Mg_2SiO_4-MgO-H_2O Earth Planetary Science Letters, 2, 130-133.

Rohrbach, A., and Schmidt, M.W. (2011) Redox freezing and melting in the Earth's deep mantle resulting from carbon-rion redox coupling, Nature, 339, 456-458.

Rüpka, L.H., Mogan, J.P., Hort, M., and Connolly, J.A.D. (2004) Serpentine and the subduction zone water cycle. Earth and Planetary Science Letters, 223, 17-34.

Sanchez-Valle, C., Sinogeikin, S.V., Smyth, J.R., and Bass, J.D. (2008) Sound velocities and elasticity of DHMS phase A to high pressure and implications for seismic velocities and anisotropy in subducted slabs. Physics of the Earth and Planetary Interiors, 170, 229-239.

Shieh, S.R., Mao, H., Hemley, R.J. and Ming, L. (2000) *In situ* X-ray diffraction studies of dense hydrous magnesium silicates at mantle conditions. Earth Planetary Science Letters, 177, 69-80.

Stagno, V, Ojwang, D.O., McCammon, C.A., and Frost, D.J. (2013) The oxidation state of the mantle and the extraction of carbon from Earth's interior. Nature, 493, 84-88.

Smyth, J.R. (1987) Beta-Mg2SiO4 – a potential host for water in the mantle. American Mineralogist, 72, 1051-1055.

Suzuki, A., Ohtani, E., and Kamada., T. (2000) A new hydrous phase δ-AlOOH synthesized at 21 GPa and 1000 °C. Physics and Chemistry of Minerals, 10, 689-693.

Thomas, S., Koch-Müller, M., Kahlenberg, V., Thomas, R., Ehede, D., Wirth, R., and Wunder, B. (2008) Protonation in germanium equivalents of ringwoodite, anhydrous phase B , and superhydrous phase B. American Mineralogist, 93, 1282-1294.

Thompson, A.B. (1992) Water in the Earth's upper mantle. Nature, 358, 295-302.

Van Keken, P., Kiefer, B., and Peacock, S. (2002) High resolution models of subduction zones: Implications for mineral dehydration reactions and the transport of water into the deep mantle, Geochemistry Geophysics and Geosystems, 3, 1056.

Yang, H., Prewitt, C.T., and Frost D.J. (1997) Crystal structure of the dense hydrous magnesium silicate, phase D. American Mineralogist, 82, 651-654.

Chapter II

High pressure melting temperature measurement through electrical measurement of capacitive current

2.1 Introduction

Melting plays a critical role in planetary differentiation and dynamics. Knowledge of the pressure-dependent melting temperatures of Earth materials is of fundamental importance for constraining the Earth's thermal structure, understanding geochemical cycles, and interpreting seismic observations (Boehler 1996). Many experimental methods have been developed to investigate melting at high pressure. As a first order phase transition, melting is characterized by the loss of long-range atomic order, which manifests as the disappearance of reflections from lattice planes and appearance of diffuse scattering signal in X-ray diffraction patterns (Anzellini et al. 2013). Melting is associated with significant changes in lattice dynamics, which lead to vanishing Lamb-Mossbauer factor (Jackson et al. 2013). The latent heat of melting gives rise to enhanced absorption of heating power (Boehler et al. 1997; Lord et al. 2010) and may be detected through differential thermal analysis (DTA) (Akella et al. 1969). Furthermore, melting results in loss of shear strength and precipitous reduction in viscosity, which can be detected through textural change (Boehler 1997, Chen et al. 2008), from the sinking of a dense sphere marker (Dobson et al. 1996), or from discontinuous change in electrical resistivity (Brand et al. 2006). Measuring the melting temperatures of materials at the pressure conditions of deep Earth

poses considerable technical challenges and consequently experimental data are limited and often uncertain (e.g., Anzellini et al. 2013; Boehler 1996; Shen and Lazor 1995).

Of those techniques for measuring melting temperature at high pressure, *in situ* X-ray diffraction is most widely used. *In situ* X-ray diffraction is able to combine with laser heated diamond anvil cell for measuring melting temperature at lower mantle and core pressure (Shen et al. 2001). However, it is limited by relatively large error in temperature determination (Campbell, 2008). Melting detection through monitoring change in lattice dynamic only works on materials containing Mossbauer active elements. In addition, its requirement for synchrotron Mossbauer spectroscopy limits its use. Thermal differential analysis is sensitive over melting but needs large amount of sample to have detectable thermal effect on the heating power, which limits its use only in piston cylinder. Detecting melting though quenched texture and sinking spheres provide the most direct and convicting results, but requires recovery of samples and multiple experiments to bracket the melting temperature at one pressure, which demands a great deal of work. Melting detection through visual observation of texture change within a diamond anvil cell is prone to subjective judgment and false signals from other unknown pre-melting effects (Cheng et al. 2003). For studying melting of minerals in upper mantle and transition zone depth, which correspond to a pressure range of 0-23 GPa, an efficient, easily implemented, and accurate high pressure melting temperature measurement technique is needed.

Except quartz, diamond, graphite and etc., the majority of geologic interesting minerals are ionic crystals. Ionic crystals are consisted of cations and anions which are locked in the crystal lattice and cannot move freely. Without charge carriers, ionic crystals are usually insulators at room temperature. When ionic crystals are heated to melt, ions are freed and able to move freely in the melt. These mobile ions can be charge carriers, and when an electrical field is applied on

the melt, cations and anions are moving in the electrical field, creating a current. So an ionic melt is a conductor whose electrical conductivity is several orders of magnitude higher than that of its solid form. With a pair of electrodes contacted with an ionic melt and a voltage on the electrodes, the current in the circuit can be measured by an ammeter. When the voltage on the electrodes are higher than the redox potentials of ions in the melt, the ions can be oxidized or reduced at the surface of the electrodes, which generates a continuous current, called Faradic current. However, if the voltage on the electrodes is below the redox potentials of any ions in the melt, the cations and anions are attracted by the electrical field and move close to cathode and anode respectively but without any redox reactions happening. This movement of ions will create a spontaneous current, called capacitive current (Reiger, 1994). But because this separation of charges creates an opposite direction electrical field counteracts the electrical field from electrodes, the separation of ions and related capacitive current will eventually stop.

This dramatic electrochemical change associated with the melting of ionic crystal can be used to detect melting. And because the electrical conductivity can be measured by a pair of electrodes contacting with the sample, it is suitable for implementation in high pressure experiment, such as piston cylinder, multi-anvil and diamond anvil cell. In a high pressure experiment the electrical conductivity of the sample can be measured *in situ* by simple external equipment while heating, so eliminating the need for limited accessible experiment facilities such as synchrotron radiation.

In this study, a new high pressure melting temperature measurement technique based on electrical measurement of capacitive current is developed, fine-tuned and implemented in multi-anvil experiments.

2.2 Method

2.2.1 Ambient pressure tests

In the beginning of this study, a series of ambient pressure experiments were conducted to test the best approach of detecting melting through electrical conductivity change during melting of ionic crystal. These tests were done using a platinum crucible and two platinum wire electrodes (Fig. 2.1). The 1st and 2nd tests used NaCl as sample, and the 3rd test used Na_2CO_3 as sample. All 3 ambient temperature tests used a small art-clay furnace to heat the sample up to 1000°C, and the heating rate was 20°C/min. The sample was heated until melting happened, which was visually checked, then the sample was cooled and heated again if necessary. Temperature was recorded using a type K thermocouple. The conductivity change was measured using different functions of a Fluke 289 multimeter. The data was recorded every 1 second. In the 1st test, the sample was NaCl and the conductivity through the melt was measured use the ohmmeter function of the multimeter. In the 2nd test, a DC 10V voltage was applied on electrodes, and the current through the melt was recorded using the ammeter function of the multimeter. To prevent current overloading the multimeter, a resistor rated at 100 ohms was added to the circuit. In the 3rd experiment, an AC 11.6V voltage was applied on electrodes and the voltammeter function of the multimeter was used to monitor the voltage drop on the melt during melting. In the 2nd and 3rd experiments the electrodes were fixed in an alumina 4 bole.

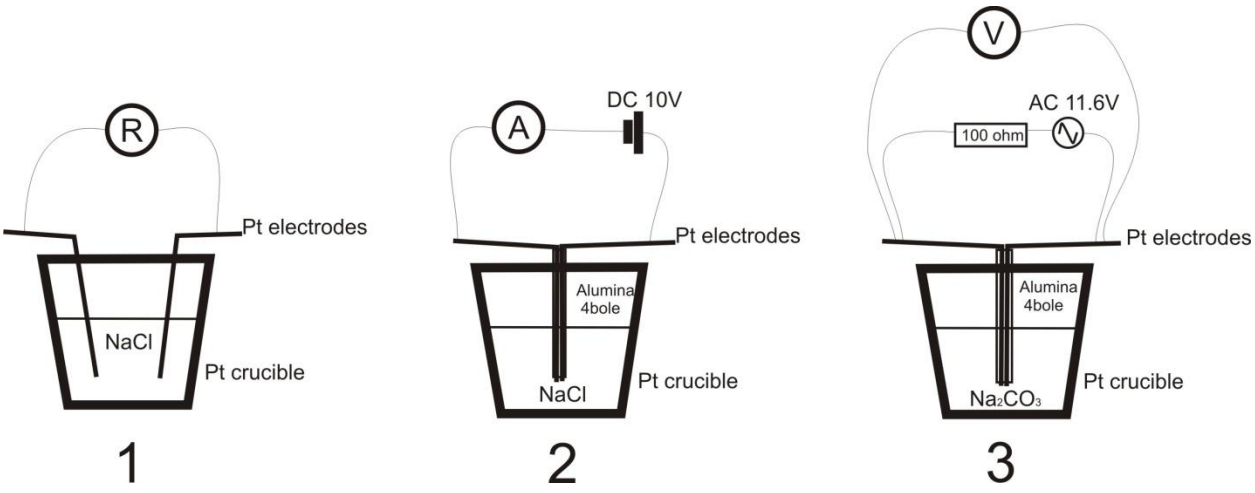

Figure 2.1 Schematic diagrams showing the experiment setups of the resistance, current and voltage measurement tests at ambient pressure.

2.2.2 High pressure tests

High pressure tests were conducted after gaining basic insights from ambient pressure experiment. High pressure experiments were conducted using a 1000-ton Walker-style multi-anvil apparatus at the University of Michigan. Fansteel tungsten carbide cubes with 8-mm truncation edge length (TEL) and octahedron-shaped pressure medium casted from Aremco 584 old-style material (Walker 1991) were used in these experiments (Fig. 2.2). The relation between the sample pressure and applied ram pressure was established using the Bi I-II, II-III and III-V transitions at room temperature (Decker et al. 1972) and the known phase boundaries at 1473 K including quartz-coesite-stishovite (Bohlen and Boettcher 1982; Zhang et al. 1996), $CaGeO_3$ garnet-perovskite (Susaki et al. 1985) and forsterite-wadsleyite- ringwoodite transitions (Katsura and Ito 1989). The sample pressure (P) is calculated from the ram force (p) according to the following formulae:

$$P \text{ (GPa)} = -0.03 + 3.21 \bullet 10^{-2} \bullet p \text{ (US ton)} - 1.40 \bullet 10^{-5} \bullet p^2 \quad \text{(8mm TEL)}$$

The precision in pressure calibration is estimated at ±5% on the basis of duplication experiments.

High temperature was generated using cylindrical-shaped foil of rhenium, with a thickness of 0.0015 inch. A standard type-C thermocouple (W26%Re and W5%Re, 0.005 inch or 0.127 mm in diameter) was used to monitor the temperature. The uncertainty in the measured temperature is estimated at ±1% for experiments up to 10 GPa and 2200 K, which includes the precisions in the thermocouple calibration and the positioning of the thermocouple junction relative to the sample (Li et al. 2003) and does not include the effect of pressure on the electromotive force (emf).

The sample used in these tests was reagent $CaCO_3$ from Aldrich (99.99%). The sample was dried in a vacuum oven at ~ 400 K for more than one week before being packed inside a Pt

tubing, which served as the sample container and helped to reduce the temperature gradient. The complete assembly was dried in the vacuum oven at 400 K for at least 24 hours before loading into the multi-anvil apparatus. In a typical high-pressure experiment, the ram pressure was increased at the rate of 100 US ton per hour during compression, and decreased at the rate of 35 US ton per hour during decompression. Data were acquired at target pressure. At target pressure the assembly was heated at the rate of 60 K per minute until melting was detected, and then cooled rapidly to 1000 K and heated again at the same rate of 60 K per minute to replicate melting detection if necessary.

For the electrical measurements, both 74%W-26%Re (from type C thermocouple) and platinum wires were tested and evaluated as electrodes. The pair of 200 μm-thick wires were inserted into a four-bore alumina holder and used as the electrodes (Fig. 2.2). Two different AC voltages, 11.6V and later 0.1V, were tested and evaluated as probing voltage applied on electrodes to induce current through the sample. In several experiments the positions of the thermocouple junction and electrode tips were purposely manipulated to investigate the influence of thermal gradient on the results (Fig. 2.2). The detailed running conditions of each experiment were listed in Table 2.1.

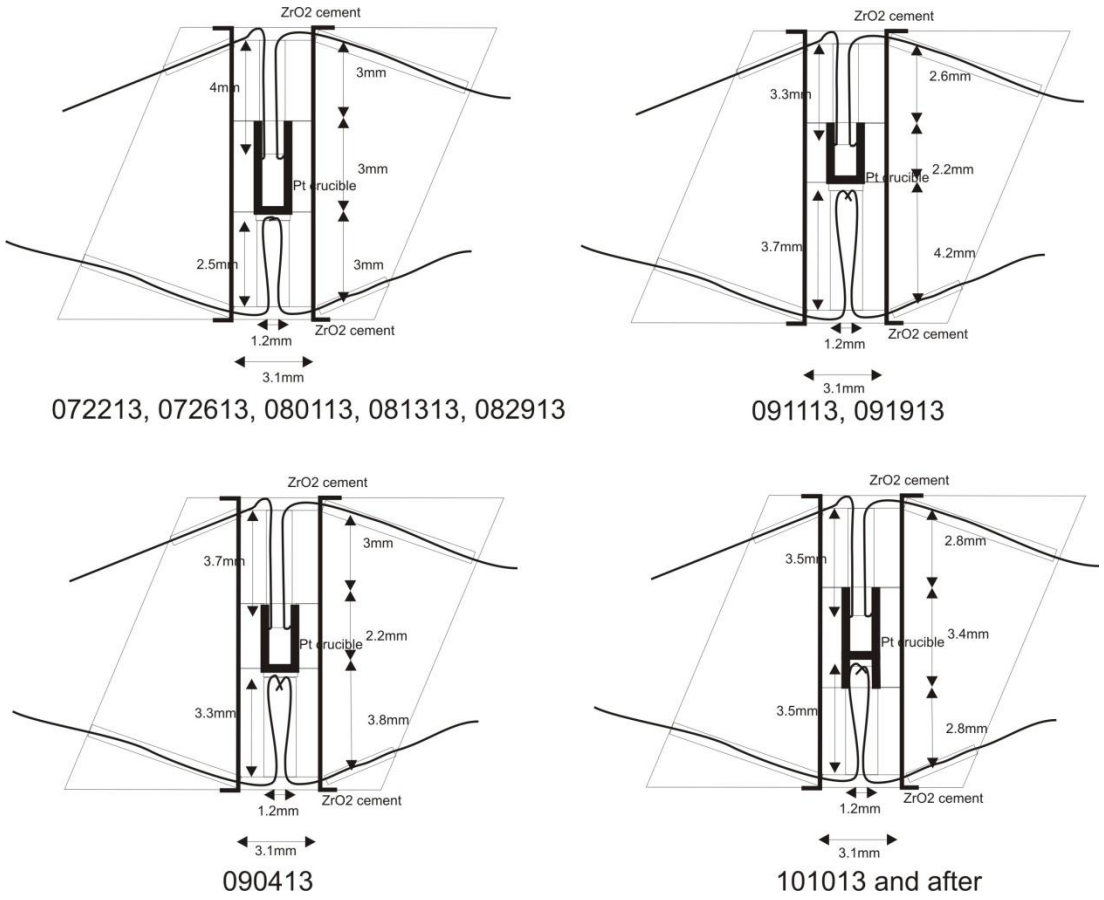

Figure 2.2 Schematic diagrams of 8mm TEL pressure assemblies used in high pressure tests (the 6-digit numbers are experiment IDs using this setup). The two wires inserted from the bottom are type C thermocouple, and two wires inserted from the top are Pt electrodes. The sample is in the Pt crucible at the center of the assembly.

Table 2.1 summary of experiment conditions of high pressure

Experiment ID	Target Pressure, GPa	Probing voltage, V	Electrode material
072213	2.7	AC* 11.6	76%W-24%Re
072613	8.0, 10.0	AC 11.6	76%W-24%Re
080113	2.7, 6.0, 8.0	AC 11.6	76%W-24%Re
081313	2.7	AC 11.6	Pt
082913	2.7, 4.5, 7.2, 9.0	AC 0.1	Pt
090413	2.7, 4.5, 6.3, 7.2, 8.1, 9.0	AC 0.1	Pt
091113	1.8, 2.7, 4.5, 6.3, 7.7, 9.0	AC 0.1	Pt
091913	1.8, 2.7, 4.5, 6.3, 7.7, 9.0	AC 0.1	Pt
101013	4.5, 6.4, 8.6	AC 0.1	Pt
111513	2.7, 4.1, 5.4, 6.8, 7.7 , 9.0	AC 0.1	Pt
112513	2.7, 4.1, 5.4, 6.8, 7.7 , 9.0	AC 0.1	Pt
121813	2.7, 4.1, 5.4, 6.8, 7.7 , 9.0	AC 0.1	Pt

* AC-Alternating current

2.3 Results and discussion

2.3.1 Ambient pressure tests

The 1st ambient pressure test using ohmmeter to measure the resistance of NaCl sample showed generally decreasing resistance over increasing temperature, but with several turbulences on the curves at around 200-300 °C and 400-700 °C (Fig. 2.3). At around 800 °C (melting temperature of NaCl), there was no large drop in resistance. However, there were two suspicious resistance drops at around 750°C and 840 °C which might indicate melting, but with all the other turbulences these small drops were too indistinct. Using an ohmmeter directly to measure resistance did not work well was probably due to the polarization of electrodes. When the ohmmeter functions, the ohmmeter itself gives a small DC probing voltage, but the DC voltage on the electrodes is too small to induce Faradic current but only polarize the electrodes immersed in ionic melt immediately. There was no continuous current going through the melt, thus the ohmmeter cannot read the resistance of the melt. The probing voltage of this ohmmeter (Fluke 289) was found to be adjusting automatically between 1.8V-5.1V, and this adjusting under the hood might cause the turbulences appearing on the curves.

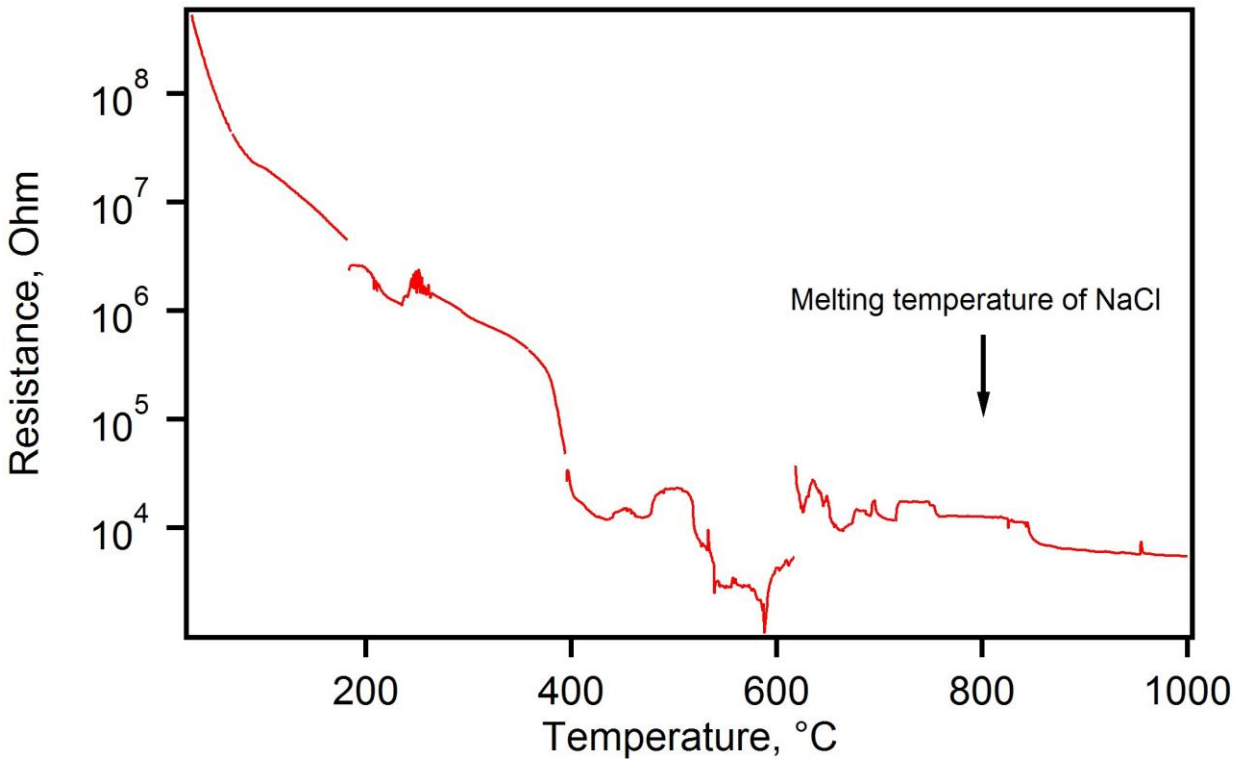

Figure 2.3 Resistance versus temperature relationship of NaCl during heating in the ambient pressure test using an ohmmeter.

The 2nd ambient pressure test used constant DC 10V as probing voltage and an ammeter to record current through NaCl sample. The recorded current versus temperature curve showed a clear current jump when melting happened (Fig. 2.4). The increase of current upon melting was sharp and more than 2 order of magnitude, which told melting temperature precisely. Visually checking of the molten sample and electrodes found that tiny liquid metal droplets escaping from the anode and floating to the surface of NaCl melt, which were supposed to be metal sodium from electrolysis reaction on the anode. After melting happens, the current was oscillating between 50 and 125 mA, which might be caused by metal sodium percolating and escaping from the surface of the electrodes disturbing the contacting area of electrodes

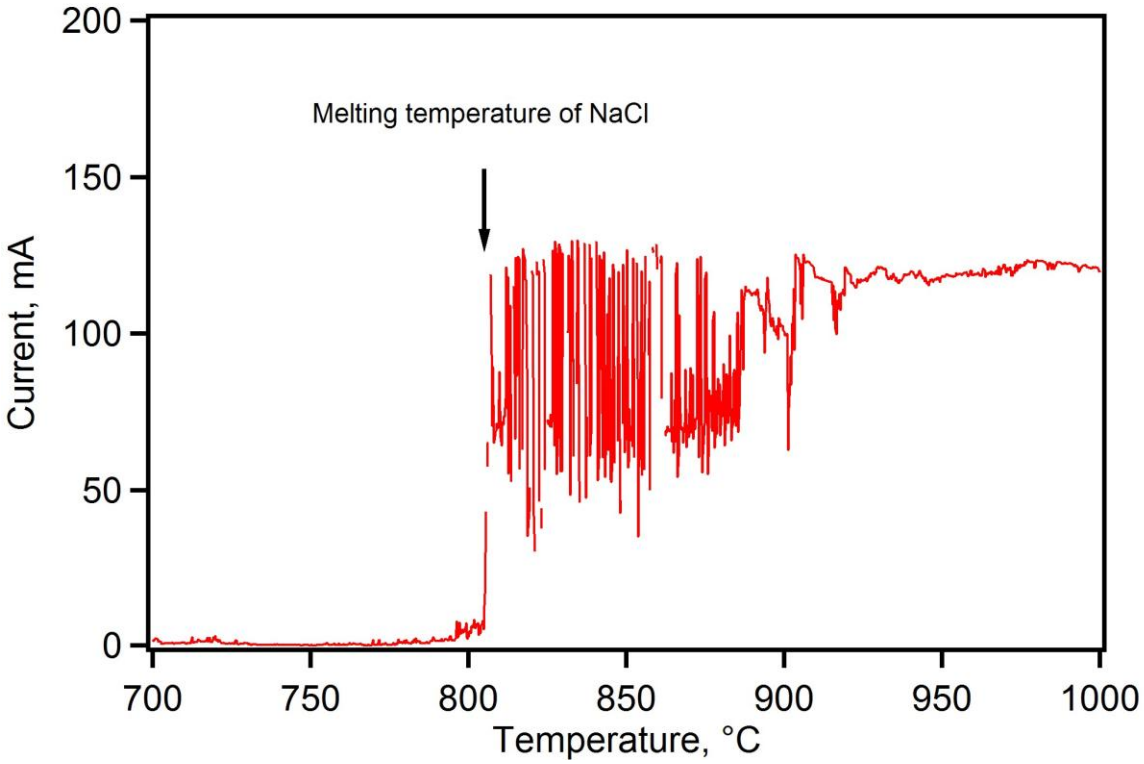

Figure 2.4 Current versus temperature relationship of NaCl during heating in the ambient pressure test using DC 10V and an ammeter.

The 3rd ambient pressure test used AC 11.6V probing voltage and a voltmeter to record the voltage drop on Na_2CO_3 sample. The recorded voltage versus temperature curve successfully detected melting (Fig. 2.5). In the 1st heating cycle, when melting happens (~850°C for Na_2CO_3), the voltage fraction on the sample dropped from ~10 V to ~2V, but there was a small voltage drop of 1-2 V starting from 680°C before melting. After melting, the sample was cooled until solidified and then heated 2 more times. Pre-melting voltage drops also happened at the 2nd and 3rd heating cycles and were in greater magnitude. In the 3rd heating cycle, the pre-melting voltage drop was difficult to tell from the drop resulted from melting. The pre-melting voltage drops were likely caused by solid ionic conduction (West, 1995), and the sodium metal from electrolysis reaction probably contaminated the sample close to electrodes and enhanced the ionic conduction in 2nd and 3rd heating cycles.

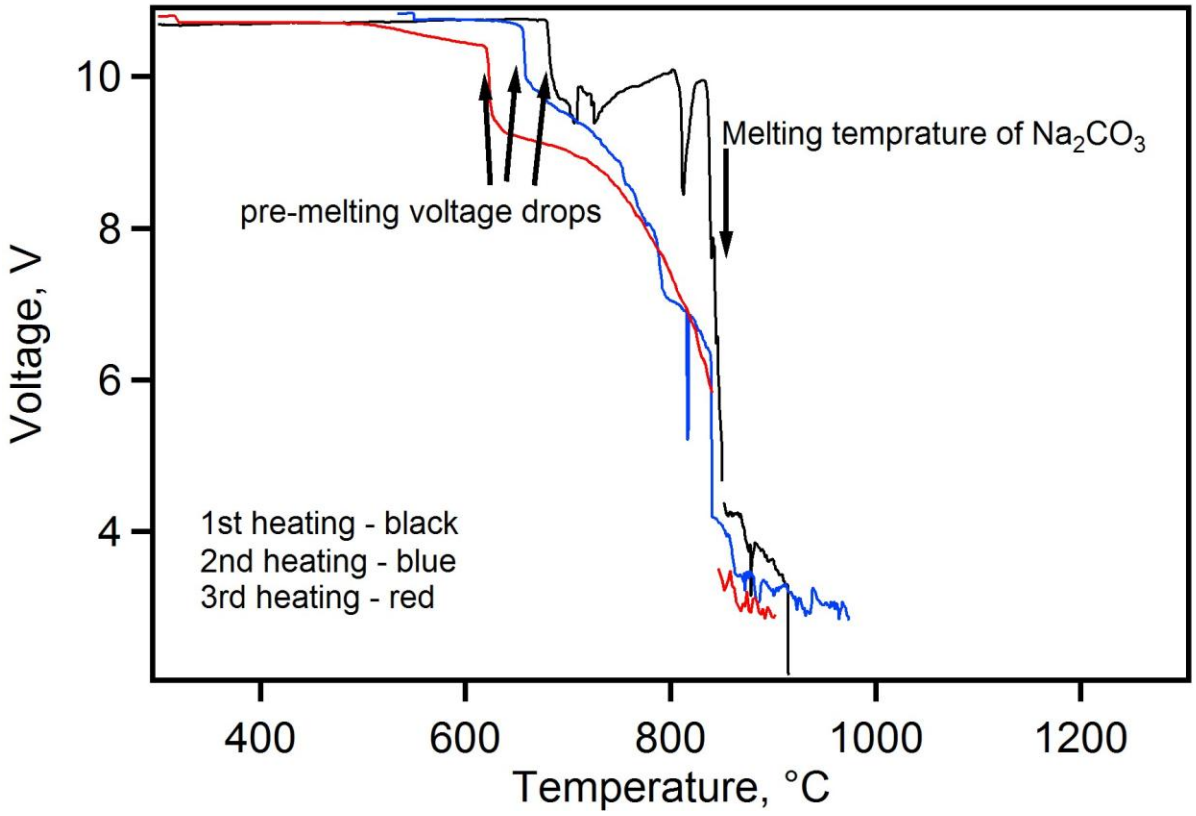

Figure 2.5 Voltage versus temperature relationship of Na_2CO_3 during heating in the ambient pressure test using AC 11.6V and voltammeter.

In summary, these ambient pressure tests proved the feasibility of detecting melting through conductivity change. Both AC and DC voltages can induce Faradic current through the melt which can be detected directly through an ammeter or by voltage drop on the sample thought a voltammeter. But the product from electrolysis reactions associated with Faradic current might contaminate the sample, which will lead degradation of melting signal in laser heating cycles.

2.3.2 High pressure tests

In Experiment 072213, 072613, 080113 (Table 2.1) 76%W-24%Re wire was tested as electrodes. The recovered charges were analyzed by electron microprobe in EDS mode (Fig. 2.6). The analyses revealed that 76%W-24Re% electrodes were oxidized due to electrolysis reactions happened on the surface of electrodes, when 11.6V AC voltage was applied on the electrodes. The 11.6 V AC voltage was apparently higher than the redox potientials of W and Re, which were oxidized to produce Ca-W-O and Ca-Re-O minerals (Fig. 2.6(b)). The dendritic textures of quenched $CaCO_3$ melt (Fig. 2.6(c)) indicated these newly formed minerals along with $CaCO_3$ experienced eutectic melting, which lowered the measured melting temperature of $CaCO_3$. Pt electrodes used in Experiment 081313 were not found to be oxidized by electrolysis reactions (Fig. 2.6(d)).

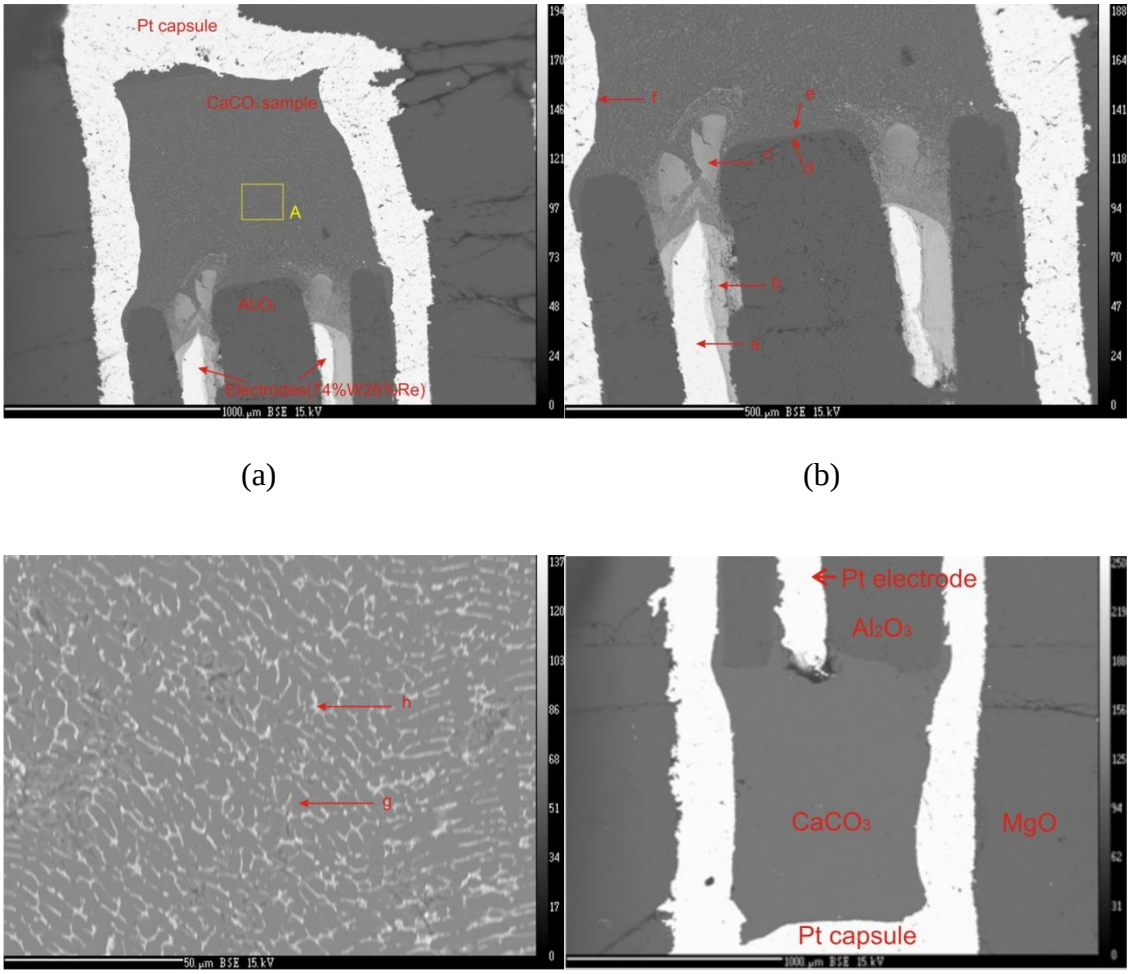

(a) (b)

(c) (d)

Figure 2.6 (a) SEM image of recovered charge of Experiment 072613 (the area in the yellow box was enlarged and shown in (c);
(b) An enlarged image showing electrodes (EDS results: a-76%W-24%Re, b-CaWxOy , c-CaRezOw , d-Al2O3, e-$CaCO_3$, f-Pt);
(c) Magnified image showing dendrites (EDS results: g-$CaCO_3$, h-CaWxOy);
(d) SEM image of recovered Experiment 081313, whose Pt electrodes were not affected by electrolysis reactions.

Experiments with varying positions of thermocouple and electrodes (Fig. 2.7(a)) showed strong correlation between relative positions of thermocouple junction and electrode tips to the equator of tube rhenium heater and the measured results (Fig. 2.7(b)). The equator of the rhenium tube heater is the hottest position in the pressure assembly, away from which temperature decreases gradually (Leinenweber et al. 2012). Assuming the temperature profiles on the two sides of the heater's equator are symmetric, if the thermocouple junction and the electrode tips sat at the same distance to the heater's equator (120813, 111513 in Fig. 2.2), the measured temperature by thermocouple should be the same as the temperature where the electrode tips sit. If the thermocouple junction sat closer to the heater's equator than the electrode tips (091113, 091913 in Fig. 2.2), the measured temperature should be higher than the temperature where the electrode tips sat, so the temperature was overestimated. If the thermocouple junction sat farther to the heater's equator than the electrode tips (082913, 090413 in Fig. 2.2), the measured temperature was underestimated. The measured melting curves (Fig. 2.7 (b)) of $CaCO_3$ from multiple experiments with varying relative positions of thermocouple junction and electrode tips were consistent with the above reasoning. All the measured melting curves in Fig. 2.7 (b) have similar curvatures, but shift in temperature. The tight brackets of $CaCO_3$ melting temperature by Irving and Wyllie (1976) provided a good anchor point to our data. The melting curves from experiments with most symmetric setups of thermocouple and electrode (111513, 120813, 120813) were also most consistent with Irving and Wyllie's brackets (Fig. 2.7 (b)).

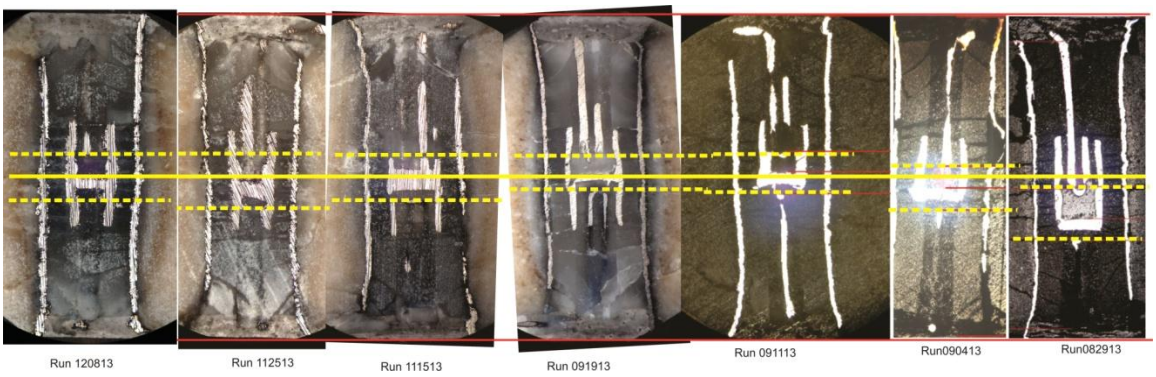

(a)

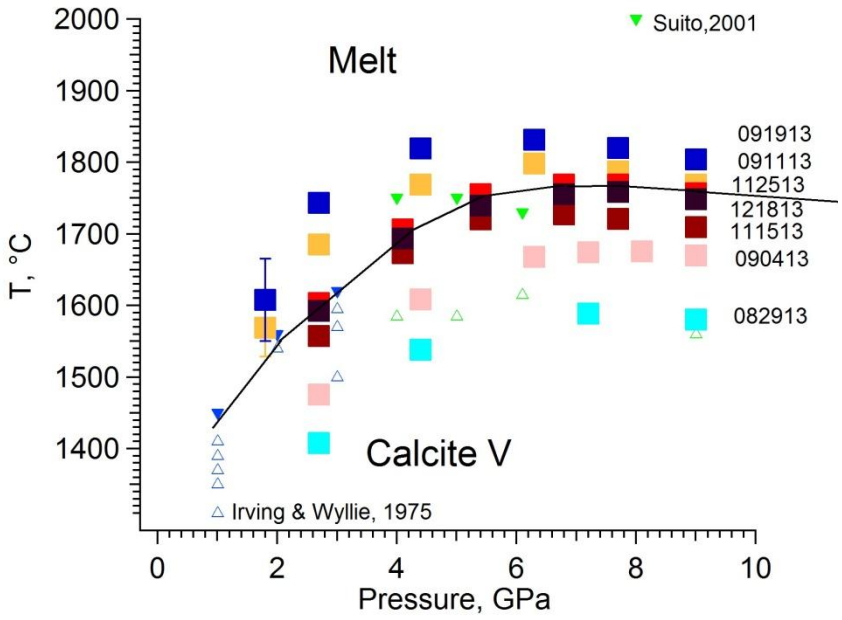

(b)

Figure 2.7 (a) Reflected light microscopic images of recovered experiment charges. The solid yellow line marks the positions of rhenium tube heater's equator, the upper dashed lines mark the positions of electrode tips in each charge and the lower dashed lines mark the positions of thermocouple junctions.
(b) Measured melting curves of $CaCO_3$ from corresponding experiments in (a).

2.4 Conclusions

Through ambient pressure and high pressure experiments, the best combination of probing voltage and electrode material were found as AC 0.1V and platinum. This voltage stays below the thresholds of oxidizing or reducing the ions at the electrodes, so an ionic melt can support capacitive current, with ions move back and forth between the two electrodes, resembling the charging and discharging of a capacitor (Rieger 1994). Compared with the existing methods (e.g., Anzellini et al. 2013; Jackson et al. 2013; Boehler et al. 1997; Chen et al., 2008; Akella et al. 1969), the capacitive current approach is characterized by its high signal/noise ratio and high efficiency. The experimental procedure only generates non-destructive capacitive current through the sample so that the sample can be melted more than 20 times before failure because of electrodes shorting in a single experiment to yield results that are reproducible within ±5 K at a given pressure. By using this approach, we can repeat measurements at each pressure and collect data at multiple pressures in each experiment.

References

Akella, J., Vaidya, S. N., and Kennedy, G. C., (1969) Melting of sodium chloride at pressures to 65 kbar. Physical Review, 185, 1135–1140.

Anzellini, S., Dewaele, A., Mezouar, M., Loubeyre, P., and Morard, G. (2013) Melting of iron at Earth's inner core boundary based on fast X-ray diffraction. Science, 340, 464-466.

Boehler, R. (1996) Melting temperature of the Earth's mantle and core: Earth's thermal structure. Annual Review of Earth Planetary Sciences, 24, 15-40.

Boehler, R., Ross, M., and Boercker, D.B. (1997) Melting of LiF and NaCl to 1 Mbar: systematics of ionic solids at extreme conditions. Physical Review Letters, 78, 4589-4592.

Bohlen, S.R., and Boettcher, A.L. (1982) The quartz ⇆ coesite transformation: a precise determination and the effects of other components. Journal of Geophysical Research: Solid Earth, 87(B5), 7073-7078.

Brand, H., Dobson, D.P., Vočadlo L. and Wood, I.G. (2006) Melting curve of copper measured to 16 GPa using a multi-anvil press. High pressure research, 26(3), 185-191.

Campbell, A.J. (2008) Measurement of temperature distributions across laser heated samples by multispectral imaging radiometry. Review of Scientific Instruments, 79, 015108.

Chen, B., Gao, L., Leinenweber, K., Wang, Y., Sanehira, T., and Li, J. (2008) *In situ* investigation of high-pressure melting behavior in the Fe-S system using synchrotron X-ray radiography. High Pressure Research, 28(3), 315-326.

Cheng, X., Liu, Z., Cai, L., and Zhang, F. (2003) Simulated melting curve of NaCl up to 200 kbar. Chinese Physics Letters, 20, 2078-2080.

Decker, D.L., Bassett, W.A., Merrill, L., Hall, H.T., and Barnett, J.D. (1972) High-pressure calibration: A critical review. Journal of Physical and Chemical Reference Data, 1, 773–835.

Dobson, D. P., Jones, A.P., Rabe, R., Sekine, T., Kurita, K., Taniguchi, T., Kondo, T., Kato, T., Shimomura, O., and Urakawa, S. (1996) *In-situ* measurement of viscosity and density of carbonate melts at high pressure. Earth and Planet Science Letters, 143, 207–215.

Jackson, J.M., Sturhahn, W., Lerche, M., Zhao, J., Toellner, T.S., Alp, E.E., Sinogeikin, S.V., Bass, J.D., Murphy, C.A., and Wicks, J.K. (2013) Melting of compressed iron by monitoring atomic dynamics, Earth and Planetary Science Letters, 362, 143-150.

Katsura, T., and Ito, E. (1989) The system Mg_2SiO_4-Fe_2SiO_4 at high pressures and temperatures: precise determination of stabilities of olivine, modified spinel and spinel. Journal of geophysical Research, 94, 15663–15670.

Leinenweber, K.D., Tyburczy, J.A., Sharp, T.G., Soignard, E., Diedrich, T., Petuskey, W.B., Wang, Y., and Mosenfelder, J.L. (2012) Cell assemblies for reproducible multi-anvil experiments (the COMPRES assemblies). American Mineralogist, 97, 353-368.

Li, J., Hadidiacos, C., Mao, H., Fei, Y., and Hemley, R. (2003) Behavior of thermocouples under high pressure in a multi-anvil apparatus. High Pressure Research, 23 (4), 389-401.

Lord, O.T., Walter, M.J., Dobson, D.P., Armstrong, L., Clark, S.M., and Kleppe, A. (2010) The FeSi phase diagram to 150 GPa, Journal of Geophysical Research: Solid Earth, 115, B06208.

Reiger, P.H. (1994) Electrochemistry 2nd ed., Chapman & Hall, 180pp.

Susaki, J., Akaogi, M., Akimoto, S., and Shimomura, O. (1985) Garnet-perovskite transformation in $CaGeO_3$: *in-situ* X-ray measurements using synchrotron radiation. Geophysical Research Letters, 12, 729-732.

Shen, G., and Lazor, P. (1995) Measurement of melting temperatures of some minerals under lower mantle pressures. Journal of Geophysical Research, 100(B9), 17699-17713.

Shen, G., Rivers, M.L., Wang, Y., and Sutton, S.R. (2001) Laser heated diamond cell system at the Advanced Photon Source for *in situ* X-ray measurements at high pressure and temperature. Review of Scientific Instruments, 72(2), 015130.

Walker, D. (1991) Lubrication, gasketing and precision in multianvil experiments. American Mineralogist, 76, 1092-1100.

West, A.R. (1995) Crystalline solid electrolytes I: General considerations and the major materials, Solid State Electrochemistry, Cambride University Press, 7pp.

Zhang, J., Li, B., Utsumi, W., and Liebermann, R.C. (1995) *In situ* X-ray observations of the coesite-stishovite transition: reversed phase boundary and kinetics. Physics and Chemistry of Minerals, 23, 1-10.

Chapter III

Melting curve of NaCl to 20 GPa from electrical measurements of capacitive current

3.1 Introduction

As a simple ionic compound, sodium chloride (NaCl) has been investigated extensively in an attempt to gain insights into its melting mechanism and melt structure (e.g., Clark 1959; Boehler et al. 1997; An et al., 2006). In high-pressure research, NaCl is widely used as a thermal insulating material and pressure marker in diamond-anvil cell (DAC) experiments, and therefore knowledge of its melting curve helps to assess its applicable ranges of pressure and temperature (e.g., Shen et al. 2001). Furthermore, monitoring the melting of NaCl offers an appealing alternative for pressure calibration of large-volume apparatus such as the piston-cylinder apparatus and multi-anvil press (e.g., Leinenweber et al. 2012), with several advantages including 1) melting occurs much more rapidly than solid-state phase transition; 2) melting can be readily recognized using a sinking marker such as a Pt sphere; 3) high-purity NaCl is readily available and less expensive than gold, the melting curve of which has been used for pressure calibration.

Earlier studies have determined the melting curve of NaCl to 6.5 GPa using the piston-cylinder apparatus and DTA method (Clark 1959; Pistorius 1966; Akella et al. 1969). The pressure coverage was subsequently extended to 100 GPa using the diamond anvil cell technique (Boehler et al. 1997). On the other hand, molecular dynamics (MD) calculations have been

performed to constrain the high-pressure melting curve of NaCl (e.g., Belonoshko and Dubrovinsky 1996; Vočadlo and Price 1996; Chen et al. 2004; Cheng et al. 2003; An et al. 2006). At 20 GPa the calculated melting temperatures from MD simulations exceed the measured values by as much as 25% and the discrepancies were attributed to superheating and surface melting effects (An et al. 2006; Vočadlo and Price 1996).

We aimed to establish the melting curve of NaCl up to ~ 20 GPa using the multi-anvil apparatus and the capacitive current based measurement. The previous results up to 6.5 GPa (Clark 1959; Pistorius 1966; Akella et al. 1969) can be good standards to test validity and estimate error of our newly developed technique discussed in Chapter II. The new data above 6.5 GPa can be used to examine if the Simon equation (Simon 1929), the Kraut-Kennedy equation (Kraut and Kennedy 1966), and the Gilvarry-Lindemann equation (Gilvarry 1956, 1966; Poirier 2000) can adequately describe the melting behavior of ionic compounds at high pressures.

3.2 Method

The high pressure experiments used in this study is similar as those in Chapter II. However, besides 8 mm TEL experiments, for experiments at pressures up to 21 GPa we used Toshiba-Tungaloy F-grade tungsten carbide cubes with 5-mm TEL and the COMPRES 10/5 assembly (Leinenweber et al. 2012), which was modified for the electrical measurements (Fig. 3.1(a)). The relation between the sample pressure and applied ram pressure was established using the Bi I-II, II-III and III-V transitions at room temperature (Decker et al. 1972) and the known phase boundaries at 1473 K including quartz-coesite-stishovite (Bohlen and Boettcher 1982; Zhang et al. 1996), $CaGeO_3$ garnet-perovskite (Susaki et al. 1985) and forsterite-wadsleyite- ringwoodite

transitions (Katsura and Ito 1989). The sample pressure (P) is calculated from the ram force (p) according to the following formulae:

P (GPa) = $5.65 \cdot 10^{-2} \cdot p$ (US ton) - $3.80 \cdot 10^{-5} \cdot p^2$ for 5-mm TEL.

The precision in pressure calibration is estimated at ±5% on the basis of duplication experiments and does not include the effect of temperature, which will be discussed later.

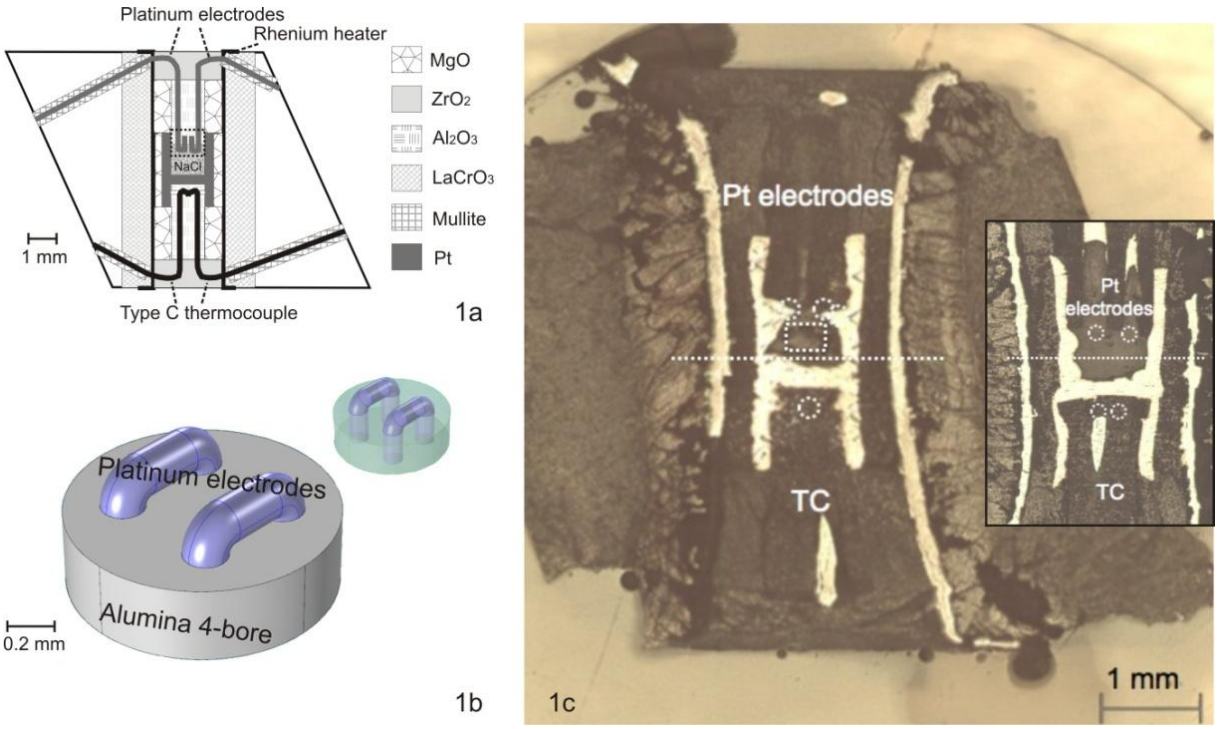

Figure 3.1 Experimental configurations for NaCl melting detection using capacitive current method.
(a) Schematic configuration of the 5-mm assembly used in this study.
(b) Illustrations of the platinum electrodes in four-bore alumina in opaque and translucent views.
(c) Reflected light microscopic images of recovered charges of Run 021314 (left) showing symmetric placement of the electrode tips and thermocouple (TC) junction (circles) with respect to the mid-length of the heater (horizontal line), and the Run 071614 (right), showing that the TC junction is located further away from the mid-length of the heater than the electrode tips

High temperature was generated using cylindrical-shaped foil of rhenium, with a thickness of 0.0015 inch or 0.038 mm for 8-mm experiments and 0.0025 inch or 0.064 mm for 5-mm experiments. A standard type-C thermocouple (W26%Re and W5%Re, 0.005 inch or 0.127 mm in diameter) was used to monitor the temperature. The uncertainty in the measured temperature is estimated at ±1% for experiments up to 15 GPa and 2600 K, which includes the precisions in the thermocouple calibration and the positioning of the thermocouple junction relative to the sample (Li et al. 2003) and does not include the effect of pressure on the electromotive force (emf), which will be discussed later.

For the electrical measurements, a pair of 200 μm-thick Pt wires were inserted into a four-bore alumina holder and used as the electrodes (Fig. 3.1 (b)). The electrode tips and thermocouple junction were placed along the rotational axis of the cylindrical-shaped heater and at the same distance to the equator of the heater, in order that the thermocouple measured the same temperature where the electrode tips sit, and they were kept within the middle third of the heater length, where the temperature variation was expected to be less than 100 K (Leinenweber et al. 2012). The measurement circuit consisted of a Mastech variac power supply, which converted 110 V, 60 Hz AC voltage from the wall outlet to 0.1 to 1 V, 60 Hz AC voltage, and a Fluke 289 multi-meter, which recorded the current through the sample. For most measurements, the AC voltage was set to 0.1 V to prevent electrolysis reactions and irreversible changes in sample composition. In order to avoid the electromagnetic perturbation from the heating current and the motor for pressure control, the voltage was occasionally raised to 1 V, which was found to be still below the threshold for electrolysis reactions.

Powder of NaCl from Aldrich (99.99%, #38,886-0) was dried in a vacuum oven at ~ 400 K for more than one week before being packed inside a Pt tubing, which served as the sample

container and helped to reduce the temperature gradient. The complete assembly was dried in the vacuum oven at 400 K for at least 24 hours before loading into the multi-anvil apparatus. In a typical high-pressure experiment, the ram pressure was increased at the rate of 100 US ton per hour during compression, and decreased at the rate of 35 US ton per hour during decompression. Data were acquired at several target pressures along the compression path. At each target pressure the assembly was heated at the rate of 60 K per minute until melting was detected, and then cooled rapidly to 1000 K and heated again at the same rate of 60 K per minute to replicate melting detection at least once. At the highest pressure and temperature of each run, we quenched the sample by turning off the power. The run products were recovered and inspected for the positioning of the electrode tips and thermocouple junctions with a Zeiss microscope with the reflected light and 10x magnification objective lens. A number of run products were examined for chemical contamination through semi-quantitative energy-dispersive spectroscopy analyses using the CAMECA SX100 electron microprobe at the University of Michigan.

To test the validity of the *in situ* electrical measurements, we performed two experiments using Pt sphere markers, one quench experiment at the University of Michigan and another synchrotron radiography experiment at GSECARS, the Advanced Photon Source at the Argonne National Laboratory. The quench experiment used the 8-mm configuration and was run at 6 GPa and 1923 K, following similar pressure and temperature paths as described above. The synchrotron experiment used the COMPRES 10/5 on-line design with graphite-filled linear slots in the lanthanum chromite sleeve as windows for X-ray diffraction and radiography measurement (Chen et al. 2008; Leinenweber et al. 2012). The experiment was compressed at room temperature to the target oil load and then heated to 750 K at the rate of 60 K per minute, where an X-ray diffraction pattern was collected on crystalline NaCl sample for *in situ* pressure

determination. During further heating at the rate of 60 K per min, we monitored the X-ray radiograph until the Pt marker sank and then quenched the experiment by turning off the power.

3.3 Results and discussion

The melting temperatures of NaCl were determined between 1.8 and 21 GPa (Table 3.1). In a typical experiment, we saw a rise in the current during heating from a few μA at temperatures below 1000 K to a few hundred μA upon melting (Fig. 3.2). Assuming that melting leads to the sharpest rise in the measured current, we took the starting point of the steepest segment of the current-temperature curve as the melting point. As the heating cycle was repeated multiple times in the same experiment, melting was detected within ±5 K. The measured melting temperatures from duplicate experiments at the same condition agree within ±30 K. At pressures below 4 GPa, the measured melting temperature sometimes shifted up by 10 to 40 K during the first two or three heating cycles, which may result from thermal relaxation of internal stress in the assembly. In these cases heating cycles were repeated until the melting temperature reached a stable value, except at 1.8 GPa where the electrodes failed shortly after melting during the first heating cycle (Fig. 3.2). The current-temperature relation was reversed upon cooling at up to 20 K lower in temperature (Fig. 3.2). The hysteresis between the heating and cooling cycle can be attributed to super-cooling, which is caused by kinetic barrier in nucleation, but there is not a counterpart effect upon melting (Galiński et al. 2006), so the melting temperatures in the study were all picked up from heating ramps.

Table 3.1 Experimental condition and results

Experiment ID	Pressure, GPa	Melting T, K
071614_5[1]	5.0[4]	1738 ± 40[5]
	9.0	1963
	12.0	2064
	15.0	2129
	18.0	2181
	21.0	2215
070114_5	5.0	1789
	9.0	2027
	12.0	2058
	15.0	2130
021314_5	9.0	2031
	12.0	2140
	15.0	2205
	17.0	2233
	19.0	2268
100313_8[2]	3.6	1552
	4.5	1719
	5.4	1791
	6.3	1850
	7.2	1911
	8.1	1955
	9.0	1993
092613_8	1.8	1348
Synchrotron Pt marker		
	4.4 at 300 K	
T1103	4.2 at 780 K	1643 to 1648
Quench Pt marker		
012411_8[3]	6	1923

[1]Data from this experiment were not used for fitting because the thermocouple junction was located at a significantly colder position than the electrode tips.
[2]At 3.6 GPa, the melting temperature is taken from the second heating cycle and it is higher than that from the first heating cycle by 40 K.
[3]The marker sank at this temperature.

[4] The pressure uncertainty can be 2 GPa at maximum at ~20 GPa and generally smaller than 2 GPa at lower pressure;
[5] The temperature error applies for all temperature data in this table and includes the error caused by pressure shift during heating;

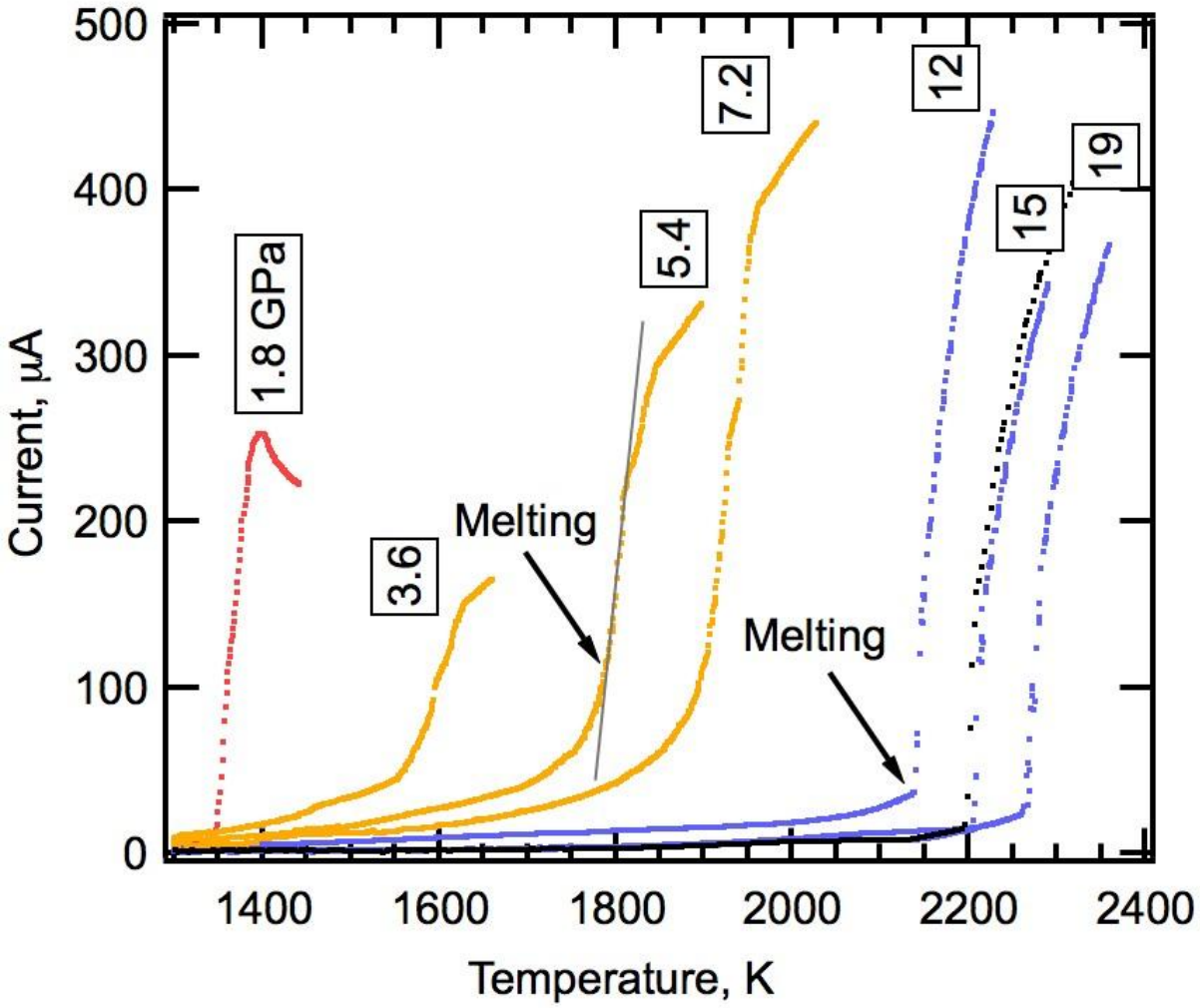

Figure 3.2 Representative current-temperature curves at selected pressures. Melting is located the abrupt take-off point of each blue curve (Run 021314), or as the starting point of the steepest segment for each yellow curve (Run 100313). The black curve represents data collected along the cooling path at 15 GPa in Run 021314. The down-going part of the red curve (Run 092613) indicates instability of the electrodes before they failed by contacting each other or with adjacent Pt capsule.

Electron microprobe analyses of several recovered samples showed no contamination from the four-bore alumina, which was in direct contact with the sample, or from any other components in the assembly, which might diffuse into the sample. Optical inspection of the experimental products revealed that in Experiment 071614 the thermocouple junction was positioned further away from the center of the heater than the electrode tips (Fig. 3.1 (c)). As a result, the measured temperatures from this experiment shifted systematically to lower values (Table 3.1). These data were not included in the fitting of melting equations.

The melting temperature of NaCl was found to increase continuously with pressure from ~ 1100 K at 1.8 GPa to ~ 2300 K at 19 GPa (Table 3.1, Fig. 3.1 (a)). In the synchrotron radiography experiment (Experiment T1103), melting was detected between 1643 and 1648 K at 4.2 GPa, whereas the quench sinking sphere experiment (Experiment 012411) indicated that melting occurred below 1923 K at 6.0 GPa. These results are consistent with the *in situ* electrical measurements.

As mentioned earlier, our measurements are subject to uncertainties arising from the effect of pressure on the emf of thermocouple, which is poorly known and hence not corrected. Limited data suggest that the type C thermocouple underestimates the temperature with a systematic error that generally increases with pressure and temperature and could amount to tens of degrees or even more than 100 K at 15 GPa and above 2000 K (Li et al. 2003). Consequently, our melting temperatures may need to be corrected upwards by tens to 100 K, especially at high pressures.

Another source of uncertainty in the data may result from pressure drift during heating. Recent synchrotron experiments showed that the sample pressure at constant applied ram pressure drifted upwards or downwards as temperature increased from 1473 to 2273 K (Fei et al. 2004a, 2004b; Leinenweber et al. 2012). The direction and magnitude of the pressure drift varied

with the TEL, configuration, temperature, pressure and heating history in a complicated manner, making it difficult to correct for the effect of temperature on pressure calibration. For the COMPRES 10/5 assembly, on which our experiments were based, available data showed that upon heating from 1473 K to 1800 K the sample pressure drifted downwards by 0.2 GPa at 20 GPa, and by 1 GPa at 15 and 17 GPa. On the other hand, the sample pressure was found to drift upwards by 2 GPa when heated from 1473 K to 2273 K at 23 GPa after experiencing a previous heating cycle (Fei et al. 2004a). Synchrotron experiments may be more susceptible to pressure drifts because the cell configurations were modified to allow X-ray access to the sample, which introduced additional heat sinks and mechanical weakness. In this study, the melting temperature at 3.6 GPa was found 30 K higher in the second heating cycle, probably because the sample pressure shifted up by about 0.3 GPa. On the other hand, experiments above 4 GPa yielded consistent melting temperatures (within ±5 K) among multiple heating cycles, indicating little pressure drift. For these reasons, we expect that the sample pressures in this study deviate from the calibration curve at 1473 K by less than 1 GPa at 15GPa and by less than 2 GPa at ~20 GPa, no greater than synchrotron experiments mentioned above. At low pressures where the melting temperature increases rapidly with pressure at a rate of ~200 K per GPa, any pressure drift would lead to large errors in the measured melting temperature. Fortunately, pressure drift generally scales with temperature (e.g., Fei et al. 2004b), and therefore smaller pressure drifts are expected at lower pressures where the melting temperatures are lower. At high pressures where the rate drops to 20 K per GPa at ~15 GPa and 10 K per GPa at ~20 GPa, a pressure drift of ±1 GPa at 15 GPa or ±2 GPa at 20 GPa would introduce an additional error of ±20 K. The combined uncertainties in the measured melting temperature, including the precision of the type C thermocouple, the reproducibility within a single experiment and among duplicate experiments,

and the pressure drift at high temperature, are estimated at ±40 K, assuming that the sources of uncertainties are random and independent.

Comparison with existing data

The melting curve of NaCl determined in this study agrees well with the existing experimental results at pressures up to 6.5 GPa and is marginally consistent with those at higher pressures (Fig. 3.1 (a)). The results reproduced the existing data from piston-cylinder experiments (Akella et al. 1969) within ±20 K, suggesting that emf correction and melting temperature change caused by pressure drift are smaller than ±20 K within the relevant pressure and temperature ranges, unless the two effects cancel out. At pressures above 12 GPa, the melting temperatures determined in this study exceed the DAC results (Boehler et al. 1997) by 100 K to 200 K. The discrepancies between the two sets of data, however, generally fall within the estimated uncertainty of ±40 K in this study and the reported uncertainties of ±50 K up to 15 GPa and ±100 K up to 20 GPa in the DAC study. Heating-induced pressure drifts in the positive direction would bring our results into better agreements with the DAC data, whereas emf corrections and pressure drifts in the negative direction are expected to do the opposite. Further studies are necessary to quantify the effect of pressure on emf and to reduce the uncertainties in sample pressure, for example, by using an internal pressure marker. Vočadlo and Price (1996) suggested that DAC measurements tend to underestimate the melting temperature because of observational biases under extreme conditions. If corrected upwards by about 10% to account for surface melting effect (Cheng et al. 2003), the DAC data would agree well with the results of this study.

Compared with the latest theoretical results (An et al. 2006), the melting temperatures reported here are in agreement at 5 GPa, 100 K lower at 10 GPa, and 150 K lower at 20 GPa

(Fig. 3.1 (a). Earlier results from MD simulations exceed that from DAC experiments by as much as 500 K at 20 GPa, well beyond the estimated uncertainty of ±100 K using the supercell methodology (Vočadlo and Price, 1996). Cheng et al. (2003) proposed that the melting temperature from simulation should be corrected downward by about 20% to account for superheating effect resulting from small system size and short time scale. More recent MD simulation (An et al. 2006) yielded substantially lower melting temperatures for NaCl, which requires no more than 5% correction for superheating to match the melting temperature at 20 GPa determined in this study.

Fitted melting equations

The empirical Simon equation has been widely used to fit pressure-dependent melting temperature in the form of $(T/T_0)^c = (P-P_0)/A + 1$, where A and c are constants with values ≥ 1, T_0 and T are the melting temperatures at the reference pressure P_0 and P, respectively. The Simon equation stands out in its simplicity and has the advantage of not requiring any knowledge of the equation-of-state (EoS) of the solid phase. It has the drawbacks that the fitting parameters A and c have no clear meanings and that they correlate with each other. Consequently, the equation works well for interpolation but cannot be used for extrapolating melting temperatures beyond the experimental pressure range. Indeed, the parameters that fitted data up to 6.5 GPa (Akella et al. 1969) differ considerably with that of this study (Table 2) and the melting curve extrapolated from the low-pressure fitting over-predicts the data by nearly 100 K at 20 GPa (Fig. 3a).

The Kraut-Kennedy melting equation describes how the melting temperature scales with volume and it can be written in the form of $T/T_0 = C \bullet \Delta V/V_0 + 1$, where $\Delta V = V_0 - V$ is the volume reduction of the solid resulting from compression, T and T_0 are the melting temperatures at V and

V_0 respectively, C is a constant that relates to the vibrational Grüneisen parameter γ_0 at V_0 and it equals to $2\bullet(\gamma_0 - 1/3)$. In this equation V and V_0 refer to the 300 K volumes of the solid phase at a given pressure and 0 GPa, respectively. For NaCl, we used the EoS parameters from Birch (1986) to calculate V from V_0 and found that γ_0 is 2.52±0.05. These values are in general agreement with existing results (Table 2). For example, by using the EoS parameters from Bridgman (1940), Akella (1969) reported a γ_0 value of 2.78, which is similar to the fitted value of 2.62±0.02 using the EoS parameters from Birch (1986).

Lindemann's law (1910) provides a semi-empirical scaling relation to fit discrete measurements of melting temperatures for interpolation, and in the absence of data it is often used together with an equation of state to predict T_m at high pressures (Poirier, 2000). Given that Lindemann (1910) only used the equation to calculate the vibrational frequency of a solid from its melting point, and that Gilvarry (1956, 1966) developed the theory of melting from Lindemann's law, we will call it Gilvarry-Lindemann melting equation. The equation takes the form $T_m \sim 0.00321\bullet M\bullet f^2\bullet \Theta_D^2\bullet V^{2/3}$, where M (the molar mass in grams) and f (the critical Gilvarry-Lindemann factor) are independent of pressure, and Θ_D (the Debye temperature) varies with V (the molar volume in cubic centimeter). The volume dependence of Θ_D can be described by the vibrational Grüneisen parameter $\gamma = -\partial \ln \Theta_D / \partial \ln V$. It is commonly assumed that γ itself scales with volume in the form $\gamma/\gamma_0 = (V/V_0)^q$, where γ and γ_0 are the Grüneisen parameters at V and V_0, respectively, and q is a constant that is usually assumed to be one in shock wave data reduction (Fei et al. 2004b). The equation can then be expressed as $T_m \sim 1.689\bullet f^2\bullet \Theta_0^2\bullet (V_0/V)^{(2\gamma_0\cdot(V_0/V)^{-q} - 1/3)}$, where Θ_0 is the Debye temperature at V_0. In this form, the equation has four fitting parameters (f, Θ_0, γ_0, q), all of which may be obtained from or compared

with independent measurements, and an isothermal EoS at 300 K is used to calculate the volume at a given pressure.

By using the EoS parameters from Birch (1986), two sets of fitting parameters were obtained: one for a fixed q at 1, and the other allowing q to be fitted by the data (Table 2). The parameters f and Θ_0 correlate with each other and cannot be uniquely fitted. With Θ_0 fixed at 302 K (Poirier, 2000), the fitted Gilvarry-Lindemann factor $f \sim 0.08$ is lower than the known value of 0.11 for alkali halides (Martin and O'Connor, 1977). If f is fixed at 0.11, the fitted Θ_0 value is 228 K, which is closer to 279±11 K, which is cited in Decker (1971). We found that holding q at 1 failed to reproduce the curvature of the melting curve between 0 and 20 GPa, whereas a good fit is obtained when q is allowed to vary. Recent experimental and theoretical studies on MgO demonstrated that variable q is required to satisfy the high P-T static and shock wave data (Fei et al. 2004b). For NaCl, a volume-dependent q value may be needed to describe the thermoelastic behavior, or it may indicate that extending the Gilvarry-Lindemann melting equation to ionic crystals does not work well because the Debye-Waller theory is limited to monoatomic solids (Gilvarry, 1956).

As widely recognized the Kraut-Kennedy melting equation can be derived from the Lindemann equation by assuming that the volume dependence of melting temperature is constant and equals to the value at V_0 (e.g. Akella et al. 1969). This approximation does not apply at higher pressures, where the measured melting temperatures deviated from the fitted curve towards lower temperatures due to the volume dependence of gamma (Akella et al. 1969). In our study, the measured melting temperature began to deviate from a linear trend at pressures above 14 GPa, where the Grüneisen parameter is expected to be higher because of the reduced volume.

3.4 Implications

The melting temperatures of NaCl between 0 and ~20 GPa, determined using a newly developed *in situ* capactive current method and the multi-anvil apparatus and, reproduce existing data up to 6.5 GPa but show considerable discrepancies with both diamond-anvil-cell and theoretical results at higher pressures. The discrepancies suggest that superheating effect in molecular dynamic calculations may be as much as 150 K at about 20 GPa. Alternatively, the discrepancies may originate from pressure effect on the emf of type C thermocouple, which was expected to underestimate the melting temperatures and are uncertain at pressures above 4 GPa (e.g., Li et al. 2003; Fei et al. 2004b). In high-pressure experiments, temperatures are commonly measured with a thermocouple or spectral radiometry. While the thermocouple method is subject to poorly constrained pressure effect on emf, the spectral radiometry also suffers from limited knowledge of wavelength dependent emissivity and optical aberration (Shen et al., 2001), leading to errors that are more than 100 K (Campbell, 2008). An independent evaluation of the pressure effect on emf remains a challenge.

The capacitive current method can be applied to determine the melting temperatures of ionic compounds at high pressures. This method uses Pt as the electrodes and sample container and is applicable below the melting point of Pt, which increases from 2042 K at 0 GPa to 2600 to 2900 K at 20 GPa (Belonoshko and Rosengren 2012). Compared with the existing methods (e.g., Anzellini et al. 2013; Jackson et al. 2013; Boehler et al. 1997; Chen et al., 2008; Akella et al. 1969), the capacitive current approach is characterized by its high signal/noise ratio and high efficiency. The experimental procedure has been optimized to generate non-destructive capacitive current through the sample so that it can be melted more than 20 times before failure because of electrodes shorting in a single experiment to yield results that are reproducible within

±5 K at a given pressure. By using this approach, we can repeat measurements at each pressure and collect data at multiple pressures in each experiment. The melting curve of NaCl may be used for hot pressure calibration of piston cylinder and multi-anvil apparatus up to about 7 GPa. At higher pressures, the melting slope becomes rather shallow, increasing by only 20 K per GPa at 15 GPa. Considering the weak dependence of melting temperature on pressure and significant uncertainties the melting temperature of NaCl, the melting curve of NaCl does not appear to be a good candidate for pressure calibration above 10 GPa.

In this study the frequency of the test voltage is 60 Hz, which is readily available and adequate for detecting melting. In impedance spectroscopy studies, a wide range of frequencies from 1 Hz to 1 MHz have been used (e.g., Gaillard et al. 2008; Yoshino et al. 2010). The signal/noise ratio may improve at higher frequencies that match ionic relaxation more closely. In future development, a waveform generator may be used to optimize the frequency of the test voltage. The design of the pressure assembly can also be modified to further reduce the random errors in temperature by improving the positioning precision and minimizing the size of the thermocouple junction. Finally, this approach may be integrated with other high-pressure devices such as diamond anvil cells to extend the pressure coverage.

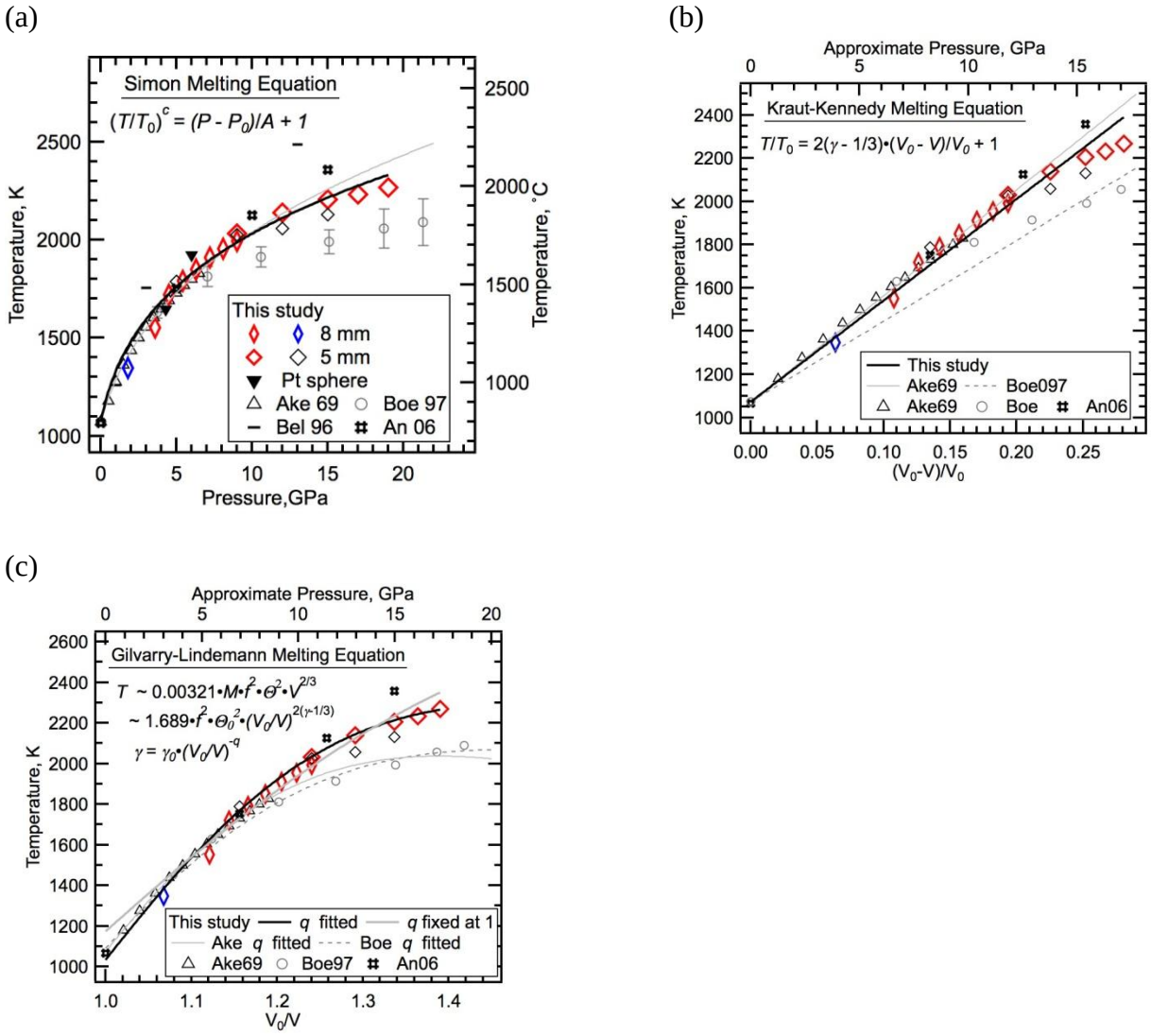

Figure 3.3 Fittings of NaCl experimental data to melting equations. Results from this study (Table 3.1) are shown as narrow diamonds for 8-mm experiments 092613 (red) and 100313 (blue), regular diamonds for 5-mm experiments 021314 (red) and 070114 (black), and solid triangles for the experiments using Pt sphere markers. Open triangles and circles represent experimental data from Akella et al. (1969) and Boehler et al. (1997), respectively.Bars and pounds represent theoretical results from Belonoshko and Dubrovinsky (1996) and An et al. (2006), respectively.

(a) Simon's equation fittings for data from this study (black thick solid curve) and for those of Akella et al. (1969) (gray thin solid curve).The melting curve of platinum (Pt) is shown as the dashed line (Belonoshko and Rosengren, 2012).

(b) Kraut-Kennedy equation fittings for data from this study (black thick solid line), for those of Akella et al. (1969) (gray thin solid curve), and those of Boehler et al. (1997) (gray thin dashed line).

(c) Gilvarry-Lindemann equation fittings for data from this study with q fitted by the data (black thick solid line) or q fixed at 1 (gray thick solid line), for those of Akella et al. (1969) (gray thin solid curve), and those of Boehler et al. (1997) (gray thin dashed line)

Table 3.2 Fitting parameters of melting equations

Simon equation				
	This study	Akella et al. 1969[1]	Pistorius 1966	Clark 1959
A	1.6(5)	0.94(4)	1.5	1.62
c	4.5(4)	3.65(8)	2.969	2.81
Kraut-Kennedy equation				
	This study	Akella et al. 1969[2]		
g	2.52(5)	2.62(2)		
Gilvarry-Lindemann equation				
	This study	This study	Akella et al. 1969[2]	Boehler 1997[2]
Q_0, K	302 (fixed)	302 (fixed)	302 (fixed)	302 (fixed)
f	0.082(1)	0.087(1)	0.0835(1)	0.0841(1)
g_0	2.9(2)	1.93(9)	2.75(3)	2.4(2)
q	1.9(1)	1 (fixed)	2.27(5)	1.9(2)

[1]Fitted for the reported data.
[2]Fitted for the reported data using Birch (1986) EoS parameters.
Numbers in parentheses are uncertainties on the last digits.

References

Akella, J., Vaidya, S. N., and Kennedy, G. C., (1969) Melting of sodium chloride at pressures to 65 kbar. Physical Review, 185, 1135–1140.

An, Q., Zheng, L., Fu, S., Ni, S., and Luo, S. (2006) Solid-liquid transitions of sodium chloride at high pressures. The Journal of Chemical Physics, 125, 154510.

Anzellini, S., Dewaele, A., Mezouar, M., Loubeyre, P., and Morard, G. (2013) Melting of iron at Earth's inner core boundary based on fast X-ray diffraction. Science, 340, 464-466.

Belonoshko, A.B., and Dubrovinsky, L.S. (1996) Molecular dynamics of NaCl (B1 and B2) and MgO (B1) melting: Two-phase simulation. American Mineralogist, 81, 303-316.

Belonoshko, A.B. and Rosengren, A. (2012) High-pressure melting curve of platinum from ab initio Z method. Physics Review B, 85, 174104.

Birch, F. (1939) Thermoelectric measurement of high temperature in pressure apparatus. Review of Scientific Instruments, 10, 137-140.

Birch, F. (1986) Equation of state and thermodynamic parameters of NaCl to 300 kbar in the high-temperature domain. Journal of Geophysical Research, 91, B5, 4949-4954.

Boehler, R., Ross, M., and Boercker, D.B. (1997) Melting of LiF and NaCl to 1 Mbar: systematics of ionic solids at extreme conditions. Physical Review Letters, 78, 4589-4592.

Bohlen, S.R., and Boettcher, A.L. (1982) The quartz ⇆ coesite transformation: a precise determination and the effects of other components. Journal of Geophysical Research: Solid Earth, 87(B5), 7073-7078.

Campbell, A.J. (2008) Measurement of temperature distributions across laser heated samples by multispectral imaging radiometry. Review of Scientific Instruments, 79, 015108.

Chen, B., Gao, L., Leinenweber, K., Wang, Y., Sanehira, T., and Li, J. (2008) *In situ* investigation of high-pressure melting behavior in the Fe-S system using synchrotron X-ray radiography. High Pressure Research, 28(3), 315-326.

Chen, Q., Cai, L., Duan, S., and Chen, D. (2004) Melting and Grüneisen parameters of NaCl at high pressure. Chinese Physics, 13(07), 1091-1095.

Cheng, X., Liu, Z., Cai, L., and Zhang, F. (2003) Simulated melting curve of NaCl up to 200 kbar. Chinese Physics Letters, 20, 2078-2080.

Clark, S. P. J. (1959) Effect of pressure on the melting points of eight alkali halides. Journal of Chemical Physics, 31, 1526-1531.

Decker, D. L. (1971), High-pressure equation of state for NaCl, KCl, and CsCl, Journal of Applied Physics, 42(8), 3239-3244.

Decker, D.L., Bassett, W.A., Merrill, L., Hall, H.T., and Barnett, J.D. (1972) High-pressure calibration: A critical review. Journal of Physical and Chemical Reference Data, 1, 773–835.

Fei, Y., Li, J., Hirose, K., Minarik, W., Van Orman, J., Sanloup, C., Van Westrenen, W., Komabayashi, T., and Funakoshi, K. (2004a) A critical evaluation of pressure scales at high temperatures by *in situ* X-ray diffraction measurements. Physics of the Earth and Planetary Interiors, Vol. 143-144, 515-526.

Fei, Y., Van Orman. J., Li, J., Van Westrenen, W., Sanloup, C., Minarik, W., Hirose, K., Komabayashi, T., Walter, M., and Funakoshi, K. (2004b) Experimentally determined postspinel transformation boundary in Mg_2SiO_4 using MgO as an internal pressure standard and its geophysical implications. Journal of Geophysical Research: Solid Earth, 109(B2), B2305.

Gaillard, F., Malki, M., lacono-Marziano, G., Pichavant, M., and Scaillet, B. (2008) Carbonatite melts and electrical conductivity in the asthenosphere. Science, 322, 1363-1365.

Galiński, M., Lewandowski, A., and Stępniak, I. (2006) Ionic liquids as electrolytes. Electrochimica Acta, 51, 5567-5580.

Gilvarry, J.J. (1956) The Lindemann and Grüneisen laws. Physical Review, 102, 308-316.
——— (1966) Lindemann and Grüneisen laws and a melting law at high pressure. Physical Review Letters, 16, 1089-1091.

Jackson, J.M., Sturhahn, W., Lerche, M., Zhao, J., Toellner, T.S., Alp, E.E., Sinogeikin, S.V., Bass, J.D., Murphy, C.A., and Wicks, J.K. (2013) Melting of compressed iron by monitoring atomic dynamics, Earth and Planetary Science Letters, 362, 143-150.

Katsura, T., and Ito, E. (1989) The system Mg_2SiO_4-Fe_2SiO_4 at high pressures and temperatures: precise determination of stabilities of olivine, modified spinel and spinel. Journal of geophysical Research, 94, 15663–15670.

Kraut, E.A., and Kennedy G.C. (1966) New melting law at high pressures. Physical Review Letters, 16, 608-609.

Lindemann, F.A. (1910) The calculation of molecular vibration frequencies. Physikalische Zeitschrift, 11, 609-612.

Leinenweber, K.D., Tyburczy, J.A., Sharp, T.G., Soignard, E., Diedrich, T., Petuskey, W.B., Wang, Y., and Mosenfelder, J.L. (2012) Cell assemblies for reproducible multi-anvil experiments (the COMPRES assemblies). American Mineralogist, 97, 353-368.

Li, J., Hadidiacos, C., Mao, H., Fei, Y., and Hemley, R. (2003) Behavior of thermocouples under high pressure in a multi-anvil apparatus. High Pressure Research, 23 (4), 389-401.

Martin, C.J., and O'Connor, D.A. (1977) An experimental test of Lindemann's melting law. Journal of Physics C: Solid State Physics, 10, 3521-3526.

Pistorius, C. W. F. T. (1966) Effect of pressure on the melting points of the sodium halides. Journal of Chemical Physics, 45, 3513-3519.

Poirier, J-P. (2000) Introduction to the Physics of the Earth's interior, 2nd ed., Cambridge University Press, 312pp.

Shen, G., Rivers, M.L., Wang, Y., and Sutton, S.R. (2001) Laser heated diamond cell system at the Advanced Photon Source for *in situ* X-ray measurements at high pressure and temperature. Review of Scientific Instruments, 72(2), 015130.

Simon, F.E., and Glatzel, G. (1929) Fusion-pressure curve. zeitschrift fur anorganische und allgemeinechemie, 178, 309-312.

Stixrude, L., Koker, N.D., Sun, N., Mookherjee, M., and Karki, B.B. (2009) Thermodynamics of silicate liquids in the deep Earth. Earth and Planetary Science Letters, 278, 226-232.

Susaki, J., Akaogi, M., Akimoto, S., and Shimomura, O. (1985) Garnet-perovskite transformation in $CaGeO_3$: *in-situ* X-ray measurements using synchrotron radiation. Geophysical Research Letters, 12, 729-732.

Vočadlo, L., and Price, G.D. (1996) The melting of MgO – computer calculations via molecular dynamics. Physics and Chemistry of Minerals, 23, 42-49.

Walker, D. (1991) Lubrication, gasketing and precision in multianvil experiments. American Mineralogist, 76, 1092-1100.

Yoshino, T., Laumonier, M., Mcisaac, E., and Katsura, T. (2010) Electrical conductivity of basaltic and carbonatite melt-bearing peridotites at high pressures: implications for melt distribution and melt fraction in the upper mantle. Earth and Planetary Science Letters, 295, 593-602.

Zhang, J., Li, B., Utsumi, W., and Liebermann, R.C. (1995) *In situ* X-ray observations of the coesite-stishovite transition: reversed phase boundary and kinetics. Physics and Chemistry of Minerals, 23, 1-10.

Chapter IV

Melting temperature of calcium carbonate up to 22 GPa and implications for carbon cycle in the mantle

4.1 Introduction

Carbon is one of the most important volatile elements in the Earth's mantle, which plays a key role in mantle magmatism. Carbon exists mostly as CO_2, CH_4 fluids in the shallow lithosphere, as carbonates in the upper mantle and as diamonds and carbides in the lower mantle (Dasgupta and Hirschmann 2010). Carbon enters the mantle mainly as carbonates through subduction (Alt et al. 2012) and can go back to the surface through partial melting of carbonated silicate as carbonatitic and kimberlitic melts (Jones et al. 2013). Carbonates may sink into the deep mantle with subducted slabs and sometimes recycled back to upper mantle through mantle upwelling, during which the carbonates might experience redox freezing and melting depends on the local oxygen fugacity (Rohrback and Schmidt, 2011). The knowledge of melting of carbonates can help us understand the origin of carbonate melt such as carbonatitic and kimberlitic melts and the pathways of carbon cycle in the mantle. Previous experiments on melting of carbonates focused on the melting of complex system such as CaO-MgO-Al_2O_3-SiO_2-CO_2 (e.g. Dalton and Presnall,1998; Canil and Scarfe,1990; Keshav et al. 2011) and CaO-MgO-Al_2O_3-SiO_2-Na_2O-K_2O-CO_2 (e.g. Dasgupta and Hirschmann, 2006; Litasov and Ohtani, 2009; Ghosh et al. 2009) up to 26 GPa, but these results had large discrepancies up to 400 K, which were probably due to the variance in the starting materials. These large discrepancies lead to

different scenarios for the process and influence of carbonate induced melting in the mantle, especially in the transition zone. Another approach to studying melting of carbonated mantle rock is thermodynamic modeling (Ghiorso, 2004), which requires complete thermodynamic parameters (such as heat capacity, enthalpy of fusion, molar volume and its pressure dependence) of every species in the melting system.

The $CaCO_3$ will experience a series of metastable phase transitions with cold compression: calcite I to calcite II, calcite II to calcite III (Fiquet et al. 1994), calcite III to calcite VI (Merlini et al. 2011). However, calcite I/calcite V will transform to aragonite at 1-8 GPa depending on different temperature (Suito et al. 2001). Aragonite will transform to post-aragonite at around 40 GPa (Ono et al. 2005). Calcite I will transform to calcite IV at ~985 K and then calcite V at ~1240 K when heated at ambient pressure, and calcite V has a unique structure that the oxygen triangles of the CO_3 group do not sit still at specified positions in the space group R -3 m, but migrate along the undulated circular orbital about carbon (Ishizawa et al., 2013). However, the solid phase transitions of $CaCO_3$ below 20 GPa have not been fully resolved. The phase boundary between calcite and aragonite phases was inconsistent among several studies (Irving and Wyllie, 1973; Mirwald, 1976; Suito et al., 2001) and the pressure and temperature of the invariant point of calcite V, aragonite and melt or the existence of other high pressure polymorph of $CaCO_3$ above 8 GPa is not known.

$CaCO_3$ does not melt but decompose to CaO and CO_2 around 900 °C, but with only 0.1 GPa pressure, it is stabilized and melt congruently (Wyllie and Boettcher, 1969). The melting temperature of $CaCO_3$ under high pressure has been studied by Irving and Willey (1975) in a piston cylinder and by Suito et al. (2001) in a multi-anvil apparatus. Irving and Willey checked melting by observing the quenched texture in a recovered sample and bracketed the melting

temperatures of $CaCO_3$ in a small range up to 3 GPa. Suito et al. combined *in situ* X-ray diffraction and X-ray diffraction on retrieved sample to bracket the melting temperatures up to 9 GPa, but the results did not constrain the melting temperature tightly which will results in a large range of possible volume of $CaCO_3$ melt. In addition more data needed to tell the melting behavior of $CaCO_3$ to the transition zone and even lower mantle pressure, which is crucial for understanding deep carbon cycle.

In this chapter, the melting curve of pure $CaCO_3$ to the transition zone pressure (up to ~ 22 GPa) is reported, which revealed the unique melting behavior of $CaCO_3$ and its possible influence on carbonated mantle rock. The melting curve of $CaCO_3$ also helps resolve the solid phase diagram of $CaCO_3$ below 22 GPa and calculate the density of $CaCO_3$ melt. The *in situ* electrical method described in Chapter II and III was used to determine the melting temperature of $CaCO_3$.

4.2 Method

The high pressure experiment used in this study is identical to the experiment in Chapter III (Fig. 4.1). The sample is 99.99% $CaCO_3$ powder from Alfa Aesar (Stock # 43073, Lot # J15N26) and was dried in vacuum oven at 120 °C for more than 1 week before experiment. After loading the sample into the assembly, the assemblies were dried in the vacuum oven at 120°C for 24 hours before experiments. 3 control group experiments with their samples exposed in controlled 70% relative humidity environment were conducted to investigate the influence of moisture to the results (Table 4.1).

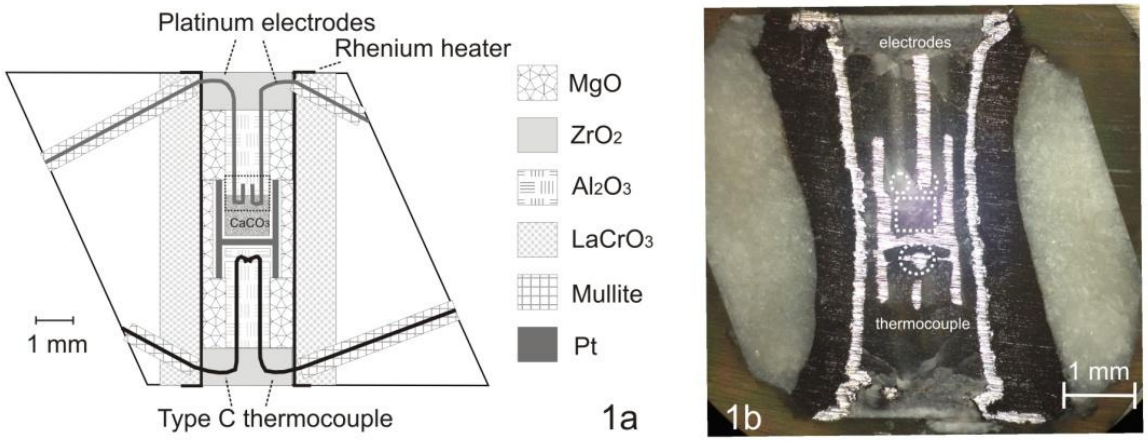

Figure 4.1 Experimental configurations for $CaCO_3$ melting detection using capacitive current method.
(a) Schematic configuration of the 5-mm assembly used in this study.
(b)Reflected light microscopic images of recovered charges of Experiment 110113 showing symmetric placement of the electrode tips and thermocouple (TC) junction (circles) with respect to the equator of the heater (horizontal line) and the sample position (box).

After experiments, the run products were recovered and inspected for the positioning of the electrode tips and thermocouple junctions with a Zeiss petrographic microscope. A number of run products were semi-quantitatively examined for chemical contamination using the CAMECA SX100 electron microprobe in energy dispersive mode at the University of Michigan.

4.3 Results and discussions

The melting temperatures of $CaCO_3$ were determined between 2.7 and 22 GPa (Table 4.1, 4.2). In a typical experiment, we saw a rise in the current during heating from a few μA at temperatures below 1000 K to a few hundred μA upon melting (Fig. 4.2). Assuming that melting leads to the sharpest rise in the measured current, we took the starting point of the steepest segment of the current-temperature curve as the melting point. As the heating cycle was repeated multiple times in the same experiment, melting was detected within ± 5 K. The measured melting temperatures from duplicate experiments at the same condition agree within ± 30 K. The error resulted from the pressure shift upon heating should be equal or smaller to that of NaCl experiments described in Chapter III, because the melting curve of $CaCO_3$ is flat over 4-20 GPa, so a maximum 2 GPa pressure shift (Fei et al. 2004a, 2004b; Leinenweber et al. 2012) only cause a temperature shift of 10-15 °C, smaller than that of NaCl experiments. The combined uncertainties in the measured melting temperature, including the precision of the type C thermocouple, the reproducibility within a single experiment and among duplicate experiments, and the pressure drift at high temperature, are estimated at ±40 K, assuming that the sources of uncertainties are random and independent.

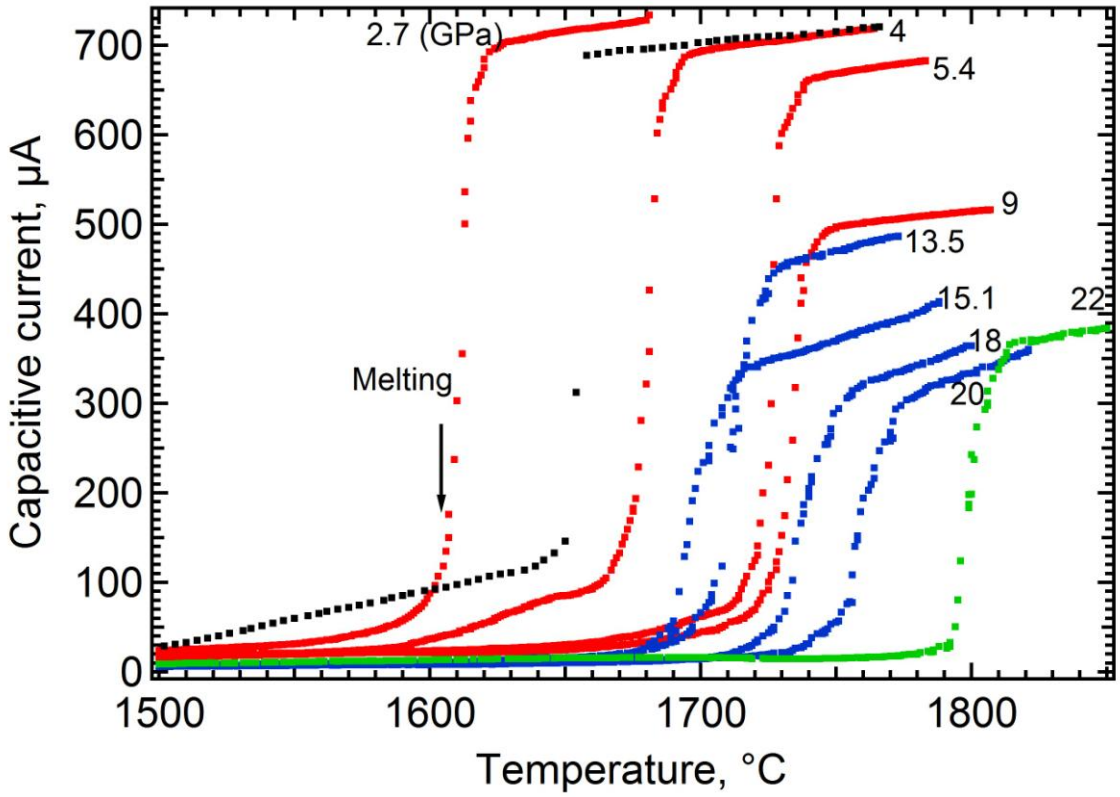

Figure 4.2 Representative current-temperature curves of $CaCO_3$ at selected pressures. Melting is located the abrupt take-off point of each curve. Red curves are data collected from Experiment 110113; blue curves are from Experiment 042414; the green curve is from Experiment 110113. All color curves are along heating path. The black curve represents data collected along the cooling path at 4 GPa in Experiment 110113.

The current-temperature relation was reversed upon cooling at up to 20-30 K lower in temperature (Fig. 4.2). The hysteresis between the heating and cooling cycle can be attributed to super-cooling, which is caused by kinetic barrier in nucleation, but there is not a counterpart effect upon melting (Galiński et al. 2006), so the melting temperatures in the study were all picked up from heating ramps. Electron microprobe analyses of several recovered samples showed no contamination from the four-bore alumina, which was in direct contact with the sample, or from any other components in the assembly, which might diffuse into the sample.

Results from 8mm TEL and 5 mm TEL experiments (Fig. 4.3) show the melting temperature of $CaCO_3$ increases continuously from 2.7 GPa to ~7 GPa, where the melting curve gradually flattens out. After reaching a peak of 1760 °C at ~7 GPa, the melting temperature starts to decrease at a rate of -7.5 °C/GPa until 15 GPa, where a sharp turn makes the melting temperature turn from decreasing to increasing again at a rate of 15 °C/GPa till our highest experiment pressure 22 GPa. The 3 control group experiments with humid samples all had melting at 200-300 °C lower than experiments with carefully dried sample, and all of them failed quickly after melting because of sample leaking out of capsule, which suggests the presence of water decreases the viscosity of $CaCO_3$ melt.

The results agree well with Irving and Wyllie (1975)'s measurements (Fig. 4.3), with the melting curve closely going through their brackets. Irving and Wyllie's experiments used the piston cylinder which bears much smaller temperature and pressure error than the multi-anvil apparatus, and their brackets of melting temperatures were narrow as well, so the agreement of our data with theirs demonstrated the accuracy and validity of our experimental method and measurements. Our melting curve also goes through most of the brackets of Suito et al. (2001)'s, and only 30°C higher than their upper bound at 6.1 GPa, which is within the experimental errors

of both experiments. Considering Suito et al. had only one data point to bracket the upper bound of melting temperature at 6.1 GPa but we have repeated measurements, our measurement should be more convincing.

Table 4.1 Experimental conditions and results

Experiment ID	Pressure, GPa	Melting Temperature, °C	Note
042414_5	9.0[1]	1744 ± 40[2]	
	10.5	1739	
	13.5	1706	
	14.3	1699	
	15.1	1694	
	16.0	1706	
	17.0	1720	
	18.0	1732	
	19.0	1741	
	20.0	1756	
	21.0	1765	
031414_5[3]	9.0	1452	Sample leak after melting
032214_5[3]	9.0	1357	Sample leak after melting
032514_5[3]	9.0	1410	Sample leak after melting
	15.0	1671	
	17.0	1697	
	19.0	1717	
121813_8	2.7	1596	
	4.1	1679	
	5.4	1726	
	6.8	1740	
	7.7	1745	

	9.0	1733
112513_8	2.7	1592
	4.1	1694
	5.4	1744
	6.8	1760
	7.7	1758
	9.0	1746
110113_5	9.0	1757
	12.0	1739
	15.0	1712
	19.0	1766
	22.0	1795

[1] The pressure uncertainty can be 2 GPa at maximum at ~20 GPa and generally smaller than 2 GPa at lower pressure;
[2] The temperature error applies for all temperature data in this table and includes the error caused by pressure shift during heating;
[3] The samples were exposed in 70% relative humidity air for 2 days.

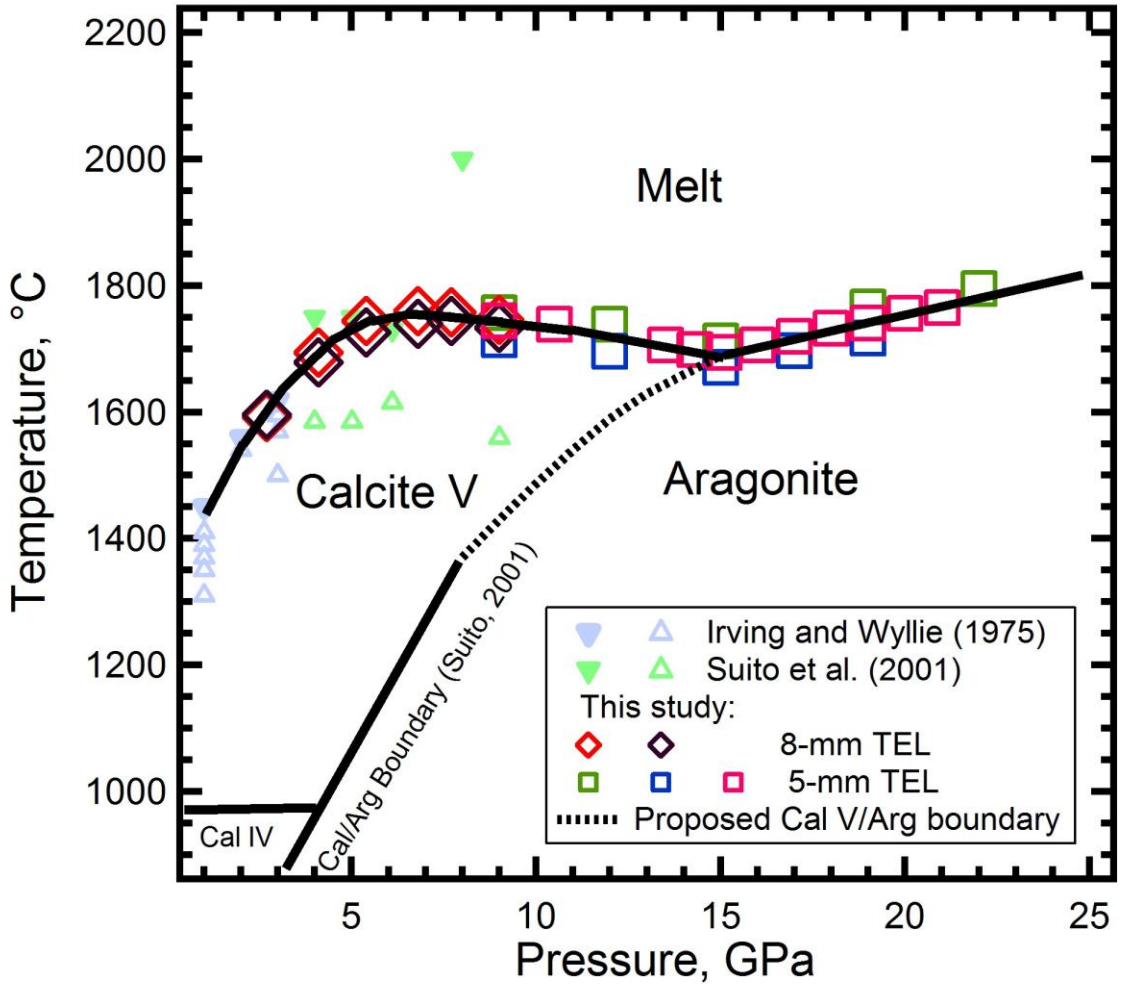

Figure 4.3 Melting curve and related phase diagram of $CaCO_3$. The diamonds represent melting temperatures collected from 8mm TEL experiments, and the squares represent melting temperatures collected from 5mm TEL experiments. Red, black, green, blue and pink colors of diamonds and squares indicate data from multiple experiments. Upward and downward triangles represent melting temperature brackets from Irving and Wyllie (1975) (light purple) and Suito et al. (2001) (light green). Solid curves represent phase boundaries, and the dotted curve represents proposed phase boundary. The calcite V/aragonite boundary is adapted from Suito et al. (2001) and the calcite IV/calcite V boundary is adapted from Redfern et al. (1989).

The flattened melting curve at ~7 GPa reflected the relative change of solid and melt volume. When the pressure is smaller than 7 GPa, the slope of the melting curve, which is also a Clapeyron slope, is positive, indicating the volume of the melt is smaller than that of solid. However, when the pressure is between 7 GPa and 15 GPa, the negative melting slope reflected a higher density of melt than the solid. A denser melt than its solid form is most likely caused by a higher compressibility of the melt than that of the solid (calcite V). With a higher compressibility the melt reduces the volume difference with the solid with increasing pressure and eventually catches up with calcite V in density at ~7 GPa and exceed the solid between 7 and 15 GPa. Another possibility is that a liquid-liquid transition, possibly caused by coordination number change of the melt, happens in the melt which decreases the volume of the melt around 7 GPa. But without any further evidence to support this hypothesis, the first explanation is more possible. The sharp change of the slope from negative to positive at 15 GPa suggests a sudden filp of volume of melt versus solid, which is mostly likely caused by solid phase transition. Considering $CaCO_3$ will experience calcite I or calcite V→ aragonite transition between 2-9 GPa depends on temperature (Suito et al. 2001), and aragonite → post-aragonite transition around 40 GPa (Ono et al. 2004), the most possible solid phase transition at 15 GPa close to melting is calcite V → aragonite transition. If the phase boundary determined by Suito et al. (2001) is extrapolated to higher temperature, it can reach the melting curve of $CaCO_3$ at around 15 GPa (Fig. 4.3), which forms a invariant point of calcite, aragonite and melt. The density jump associated with calcite → aragonite phase transition can cause the deflection of the melting curve at 15 GPa.

The high melting temperature of calcite V around 7 GPa forms a ‘bump’ (Fig. 4.3) on the melting curve, which may be caused by the unique structure of calcite V (Ishizawa et al. 2013).

The rotational disorder probably increases the stability of calcite structure, so the melting temperature of calcite V can be even higher than aragonite between 15-20 GPa.

The local melting temperature minimum at 15 GPa found in this study coincides in pressure (Fig. 4.4) with the dips in the solidus curves of CMS-CO_2 and CMAS-CO_2 found by Keshva et al. (2011). But the dips were not found in CMASN-CO_2 system (Ghosh et al. 2009; Litasov and Ohtani, 2009). A further examination of results of these studies (Keshva et al. 2011; Ghosh et al. 2009; Litasov and Ohtani, 2009) revealed that an increase of calcium composition around 15-20 GPa (Fig. 4.4) in the melt also coincides with the local melting temperature minimum of $CaCO_3$ around 15 GPa. The low melting temperature of $CaCO_3$ may cause the dips in solidus curves of CMS-CO_2 and CMAS-CO_2 (Keshva et al. 20011) and the high calcium composition in the melt also indicates the low melting point of $CaCO_3$ around 15 GPa promotes calcium go into the melt preferentially. The absence of dips in the solidus curves in the CMASN-CO_2 system may be caused by alkaline contents. Na_2CO_3 and K_2CO_3 prefer more strongly going to melt than $CaCO_3$, so they will form the first melt when partial melting happens, covering the effect of $CaCO_3$ on solidus.

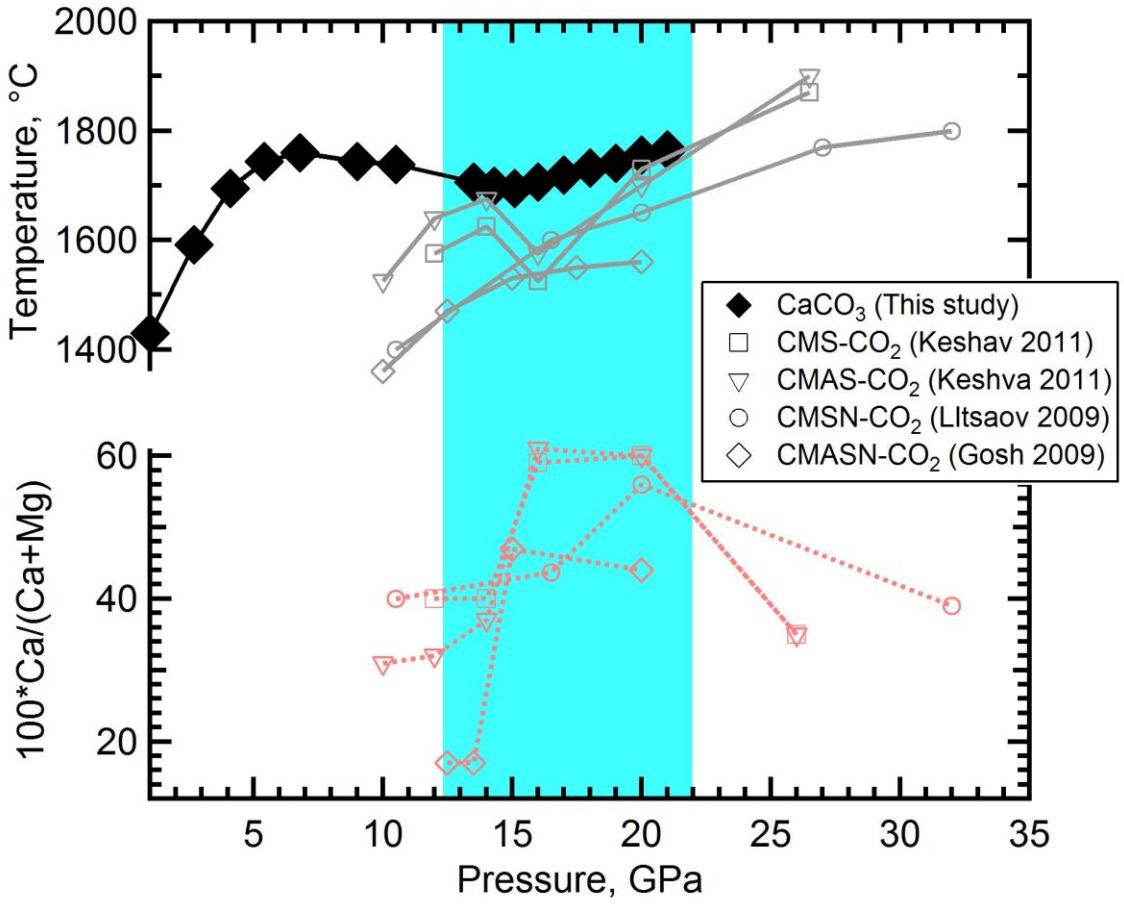

Figure 4.4 Melting curve of $CaCO_3$ (black diamonds and curves) and solidus curves of simplified carbonated peridotite (grey symbols and curves) and calcium number of melts from melting experiments of simplified carbonated peridotite (red symbols and doted curves). Black diamonds represent the best estimated melting temperatures from this study. The light blue shade highlights the pressure correlation between the melting temperature minimum of $CaCO_3$ around 15 GPa and the dips of solidus curves from Keshav et al. (2001) and the increased calcium number. CMS, CMAS, CMSN, CMASN represent the ingredients of simplified peridotite (C—CaO, M—MgO, A—Al_2O_3, S—SiO_2, N—Na_2O).

4.4 Implications

The melting curve of $CaCO_3$ (Fig. 4.5) along with solidus curves of carbonated mantle rock (Fig. 4.4) are much higher than the geotherm in a 'hot' subduction system (Schilling, 1991), which may indicate little or none carbonate melting along with subduction. Thus carbonates may enter into transition zone and lower mantle through subduction. If we consider the influence of possible low oxygen fugacity of the lower mantle (McCammon, 1997), the carbonates in the subduction slab may be reduced to diamond in the lower mantle (Rohrbach and Schmidt, 2011), by which carbon is stabilized in the lower mantle. The melting temperature of $CaCO_3$ keeps in a narrow range between 1700 and 1800 °C in a large pressure range of 4-22 GPa because of high melting temperature of calcite V and a minimum melting temperature around 15 GPa. This flat segment of melting curve is likely to cross over a hot mantle geotherm (Fig. 4.5 T_p=1550°C), such as upwelling regions like mantle plumes or hotspots. Because the melting temperature of $CaCO_3$ can be viewed as the upper limit of solidus temperature of carbonated peridotite, so the partial melting of carbonated peridotite in the upwelling system is very likely. In the case of upwelling mantle, carbonate induced melting likely happened at around 660 km where diamonds in the lower mantle enters the transition zone and experience redox melting (Rohrbach and Schmidt, 2012). If the geotherm is a normal one (Fig. 4.5, T_p=1350°C), melting may not happen intermediately when diamonds get oxidized to carbonates above 660 km depth, but likely continue ascending and melt around 410 km depth where the solidus of carbonated peridotite has a minimum temperature (Keshav et al. 2011). Recent seismic observations of low velocity zones around 410 km (Tauzin et al. 2010) and 660 km (Schmandt et al. 2014) are mostly explained as caused by dehydration melting due to lower water storage capacity of mantle minerals above and below transition zones (Bercovici and Karato, 2003; Schmandt et al. 2014), however at these

depth carbonate induced melting can be alternate explanations. The water filter model restricts the depth of melting around 410 km and 660 km depth, however, there are low S-wave velocity areas within the transition zone (Ritsema et al. 2011) which are mostly associated with hotspots. These low velocity areas cannot be explained by water filter model, but may be caused by carbonate induced melting.

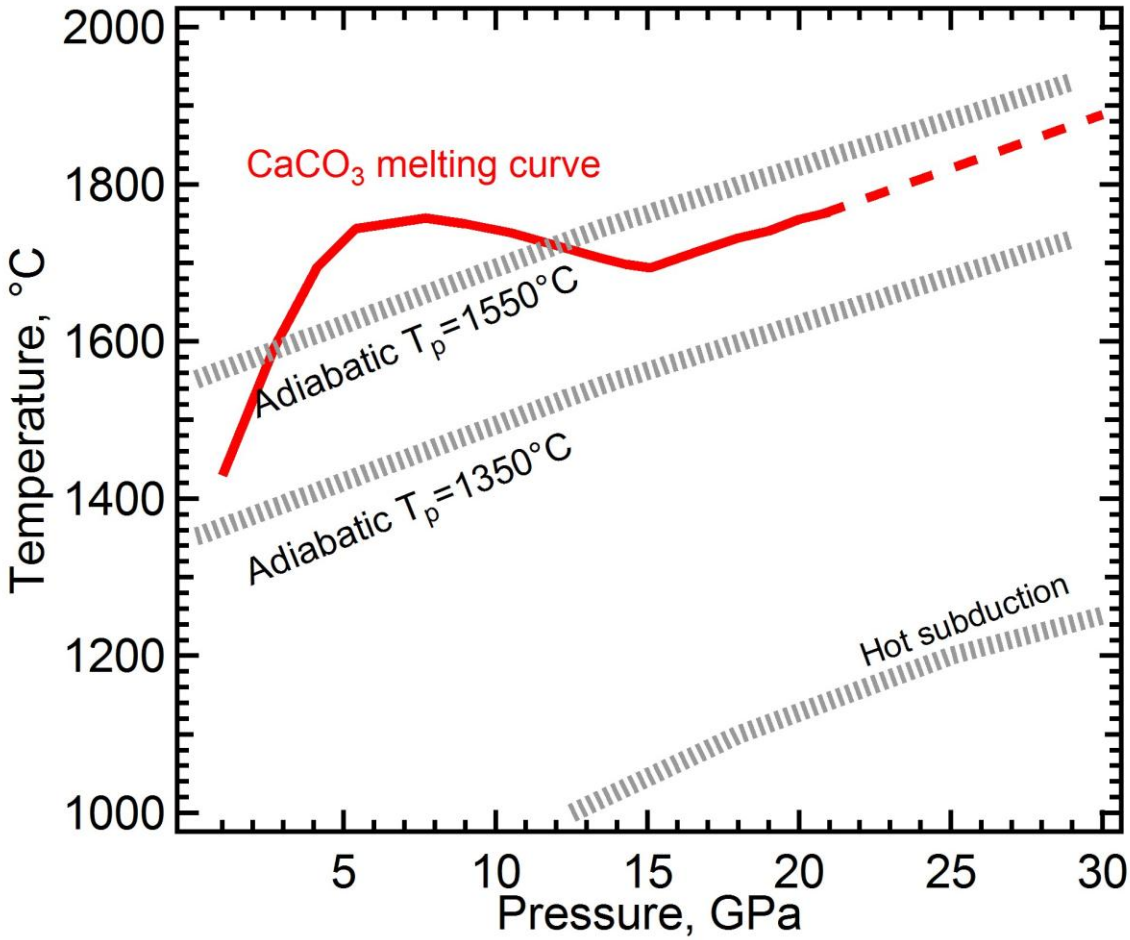

Figure 4.5 Comparison of the melting curve of $CaCO_3$ (red curve), with various geotherms (dotted lines): hot subduction is after Bina et al. 2001; the adiabat for a normal mantle with a potential temperature (Tp) of 1350 °C and a plume adiabat for a potential temperature of 1550 °C (Schilling, 1991), both with a gradient of 10 °C/GPa (Katsura et al., 2009).

References

Alt, J. C., and D. A. H. Teagle (1999), The uptake of carbon during alteration of ocean crust, Geochim. Cosmochim. Acta, 63(10), 1527-1535.

Bercovici, D., and Karato, S. (2003), Whole mantle convection and transition-zone water filter, Nature, 425, 39-44.

Bina, C.R., Stein S., Marton F.C., and Van Ark, E.M. (2001) Implications of slab mineralogy for subduction dynamics. Phys Earth Planet Inter, 127,51–66.

Boettcher, A.L., and Wyllie, P.J. (1969) Liquidus phase relationships in the system CaO-CO_2-H_2O to 40 kilobars pressure with petrological applications. American Journal of Science, 267, 489-508.

Dalton, J.A., and Presnall, D.C. (1998) The continuum of primary carbonatitic-kimberlitic melt compositions in equilibrium with lherzolite: data from the system CaO-MgO-Al_2O_3-SiO_2-CO_2 at 6 GPa. Journal of Petrology, 39, 1953 – 1964.

Dasgupta, R., and Hirschmann, M.M. (2006) Melting in the Earth's deep upper mantle caused by carbon dioxide: Nature, 440, 659–662.

Dasgupta, R. and Hirschmann, M. M. (2010). The deep carbon cycle and melting in Earth's interior. Earth and Planetary Science Letters (Frontiers) 298, 1-13.

Fiquet, G., Guyot, F., and Itié, J.-P. (1994) High-pressure X-ray diffraction study of carbonates: $MgCO_3$, $CaMg(CO_3)_2$, and $CaCO_3$. American Mineralogist, 79, 15-23.

Fei, Y., Li, J., Hirose, K., Minarik, W., Van Orman, J., Sanloup, C., Van Westrenen, W., Komabayashi, T., and Funakoshi, K. (2004a) A critical evaluation of pressure scales at high temperatures by *in situ* X-ray diffraction measurements. Physics of the Earth and Planetary Interiors, Vol. 143-144, 515-526.

Fei, Y., Van Orman. J., Li, J., Van Westrenen, W., Sanloup, C., Minarik, W., Hirose, K., Komabayashi, T., Walter, M., and Funakoshi, K. (2004b) Experimentally determined postspinel transformation boundary in Mg_2SiO_4 using MgO as an internal pressure standard and its geophysical implications. Journal of Geophysical Research: Solid Earth, 109(B2), B2305.

Galiński, M., Lewandowski, A., and Stępniak, I. (2006) Ionic liquids as electrolytes. Electrochimica Acta, 51, 5567-5580.

Ghiorso, M.S. (2004) An equation of state for silicate melts. III analysis of stoichiometric liquids at elevated pressure: shock compression data, molecular dynamics simulations and mineral fusion curves. American Journal of Science, 304, 752-810.

Ghosh, S., Ohtani, E., Litasov, K.D., Terasaki, H. (2009) Solidus of carbonated peridotite form 10 to 20 GPa and origin of magnesiocarbonatite melt in the Earth's deep mantle. Chemical Geology, 262, 17-28.

Irving, A. J., and Wyllie P. J. (1975), Subsolidus and melting relationships for calcite, magnesite and join $CaCO_3$-$MgCO_3$ to 36 kb, Geochim. Cosmochim. Acta, 39(1), 35-53.

Irving, A.J., and Wyllie P.J. (1973) Melting relationships in CaO-CO_2 and MgO-CO_2 to 36 kilobars with comments on CO_2 in the mantle. Earth and Planetary Science Letters, 20, 220-225.

Ishizawa, N., Setoguchi, H., and Yanagisawa, K. (2013) Structural evolution of calcite at high temeperatures: Phase V unveiled. Nature Scientific Reports, 3, 2832.

Jones, A.P., Genge, M., and Carmody, L. (2013) Carbonate melts and carbonatites. Reviews in Mineralogy & Geochemistry, 75, 289-322.

Katsura T., Shatskiy A., Manthilake G., Zhai S., Fukui H., Yamazaki D., Matsuzaki T., Yoneda A., Ito E. Kuwata A., Ueda A., Tange Y., Nozawa A., and Funakoshi K. (2009) Thermal expansion of forsterite at high pressures determined by *in situ* X-ray diffraction: The adiabatic geotherm in the upper mantle, Physics of the Earth Planetary Interior, 174, 86 – 92.

Keshav S., Gudfinnsson Gudmundur H., Presnall Dean (2011) Melting Phase Relations of Simplified Carbonated Peridotite at 12-26 GPa in the Systems CaO-MgO-SiO_2-CO_2 and CaO-MgO-Al_2O_3-SiO_2-CO_2: Highly Calcic Magmas in the Transition Zone of the Earth, Journal Of Petrology, vol. 52 p.2265-2291.

Leinenweber, K.D., Tyburczy, J.A., Sharp, T.G., Soignard, E., Diedrich, T., Petuskey, W.B., Wang, Y., and Mosenfelder, J.L. (2012) Cell assemblies for reproducible multi-anvil experiments (the COMPRES assemblies). American Mineralogist, 97, 353-368.

Litasov, K.D., and Ohtani, E. (2009) Solidus and phase relations of carbonated peridotite in the system CaO-Al_2O_3-MgO-SiO_2-Na_2O-CO_2 to the lower mantle depths: Physics of the Earth and Planetary Interiors, 177, 46–58,

McCammon, C. (1997) Perovskite as a possible sink for ferric iron in the lower mantle, Nature, 387, 694-696.

Merlini, M. Crichton, W., Handfland, M., and Crichton, W. (2012) $CaCO_3$-III and $CaCO_3$-VI, high-pressure polymorphs of calcite: possible host structures for carbon in the Earth's mantle. Earth and Planetary Sciences Letters, 333, 265-271.

Mirwald, P.W. (1976) A differential thermal analysis study of the high-temperature polymorphism of calcite at high pressure. Contributions to Mineralogy and Petrology, 59, 33-40.

Ono, S., Kikegawa, T., Ohishi, Y., and Tsuchiya, J. (2005) Post-aragonite phase transformation in $CaCO_3$ at 40 GPa. American Mineralogist, 90, 667-671

Redfern, S.A.T., and Angel, R.J. (1999) High-pressure behavior and equation of state of calcite, $CaCO_3$. Contributions to Mineralogy and Petrology. 134, 102-106.

Ritsema, J. van Heijst, H.J., Deuss, A., and Woodhouse, J.H. (2011) S40RTS: a degree-40 shear-velocity model for the mantle from new Rayleigh wave dispersion, teleseismic traveltimes, and normal-mode splitting function measurements, Geophysical Journal International, 184, 1223-1236.

Rohrback, A., and Schmidt M.W. (2011) Redox freezing and melting in the Earth's deep mantle resulting from carbon-iron redox coupling. Nature, 472, 209-212.

Schilling, J. G., (1991) Fluxes and excess temperatures of mantle plumes inferred from their interaction with migrating midocean ridges, Nature, 352, 397-403.

Schmandt, B., Jacobsen, S.D. and Becker, T.W. and Liu, Z., and Dueker, K.G. (2014) Dehydration melting at the top of the lower mantle. Science, 344, 1265-1268.

Suito, K., et al. (2001), Phase relations of $CaCO_3$ at high pressure and high temperature, Am. Miner., 86(9), 997-1002.

Tauzin, B., Debayle, E. and Wittingger, G. (2010) Seismic evidence for a global low-velocity layer within the Earth’s upper mantle. Nature Geoscience, 3, 718-721.

Chapter V

Melting curves and phase diagrams of Na_2CO_3 and K_2CO_3 up to 20 GPa

5.1 Introduction

Alkaline carbonates are important carbonate species that promote melting processes in the mantle. Experiments have demonstrated that even a small amount of alkaline content significantly lowers the solidus temperature of carbonated peridotite or eclogite (e.g. Dasgupta and Hirschmann, 2006; Ghosh et al., 2009; Litasov and Ohtani, 2009). The near solidus melt of carbonated mantle rock would be alkaline enriched and may be the origin of carbonatitic and kimberlitic melt (Jones et al. 2013). Alkaline carbonates are also important agents for metasomatism (Green and Wallace 1988) and crucial for the diamond formation (Schrauder and Navon 1994). Previous studies about alkaline carbonates were mostly on alkaline-bearing carbonated mantle rocks or binary carbonates (e.g. Dalton and Presnall, 1998; Shatskiy et al. 2013a, 2013b; Litasov et al. 2013). However, melting behaviors and high pressure mineral phases of pure Na_2CO_3 and K_2CO_3 are unclear yet. So it is important to study the melting behaviors from end member Na_2CO_3 and K_2CO_3.

In this chapter melting curves of Na_2CO_3 and K_2CO_3 were measured up to 20 GPa. The high pressure polymorphs of K_2CO_3 were investigated as well.

5.2 Method

5.2.1 Melting curve measurement

The melting curves of Na_2CO_3 and K_2CO_3 were measured by the capacitive current based measurement described in Chapter II, III and IV. The high pressure experiments were identical to those in Chapter III and IV. Different from experiments in Chapter II, III and IV, only 10 mm TEL modified COMPRES assemblies (Leinenweber et al. 2012) were used for the entire pressure range from ~ 3 GPa to 20 GPa. The relationship between pressure and ram force can be found in Chapter IV.

The samples were 99.99% Na_2CO_3 and 99.9% K_2CO_3 from Alfa Aesar. Because both Na_2CO_3 and K_2CO_3 are highly hydroscopic, extra carefulness were taken to ensure the samples were dry. Before experiments, samples and half-finished pressure assemblies were kept in a vacuum oven at 120 °C for 2-3 weeks. When the samples were loaded into the platinum capsule (see chapter II and III), the capsule and sample were heated up to 500 °C for 10 min in a furnace. Then the capsule was quickly put into the pressure assembly. Then the pressure assembly was closed and kept in the vacuum oven at 120 °C for a week before experiments. During experiments, the pressure-temperature path was the same with those in Chapter III and Chapter IV. At one pressure, the melting measurements were repeated at least once. After experiments, the sample was mounted into epoxy and oil grounded. The samples were inspected for the positioning of the electrode tips and thermocouple junctions with a Zeiss petrographic microscope.

5.2.2 *In situ* X-ray diffraction

To further investigate the high pressure phase transitions of K_2CO_3, angular dispersive X-ray diffraction experiments on K_2CO_3 under high pressure with double-sided laser-heated symmetric

diamond anvil cell (with cutlet size of 300 μm) (Fig. 5.1) were conducted at Beamline 16-ID-B of HPCAT, the Advanced Photon Source at the Argonne National Lab. X-ray was monochromatized to a wavelength of 0.4066 μm and focused to an area of 5 μm by 10 μm. Diffraction images were recorded over 5s with a Pilatus-1M pixel array detector and were integrated and corrected for distortions using the FIT2D software (Hammersley et al. 1996). The sample detector distance was 218.7318 mm.

K_2CO_3 mixed with 4% wt platinum power was loaded in Rhenium gaskets with a pressure chamber of 180 μm in diameter and 40 μm thick. The sample has been dried in vacuum oven at 120 °C for 1 week before loaded. After loaded, the diamond anvil cell was half-closed and put in the vacuum oven for 24 hours. Platinum power was added to enhance the heat adsorption of the sample and as pressure standard. To maximize the signal, no other pressure medium and thermal insulator were added, and K_2CO_3 itself was used as the pressure transmitting medium and thermal insulator besides as the sample.

K_2CO_3 samples were *in situ* double-sided laser-heated using the laser-heating system at HPCAT consisting of two identical Nd:YLF lasers (λ = 1053 nm). Temperatures were determined by fitting the thermal radiation to the black body radiation function, and the measurement had an accuracy of ±100 K (Errandonea et al. 2003). The pressure was determined by the diffraction lines of platinum in the sample chamber based on Fei et al.'s EOS (2007). The pressure error was ±1 GPa based on the standard deviation of the lattice parameter.

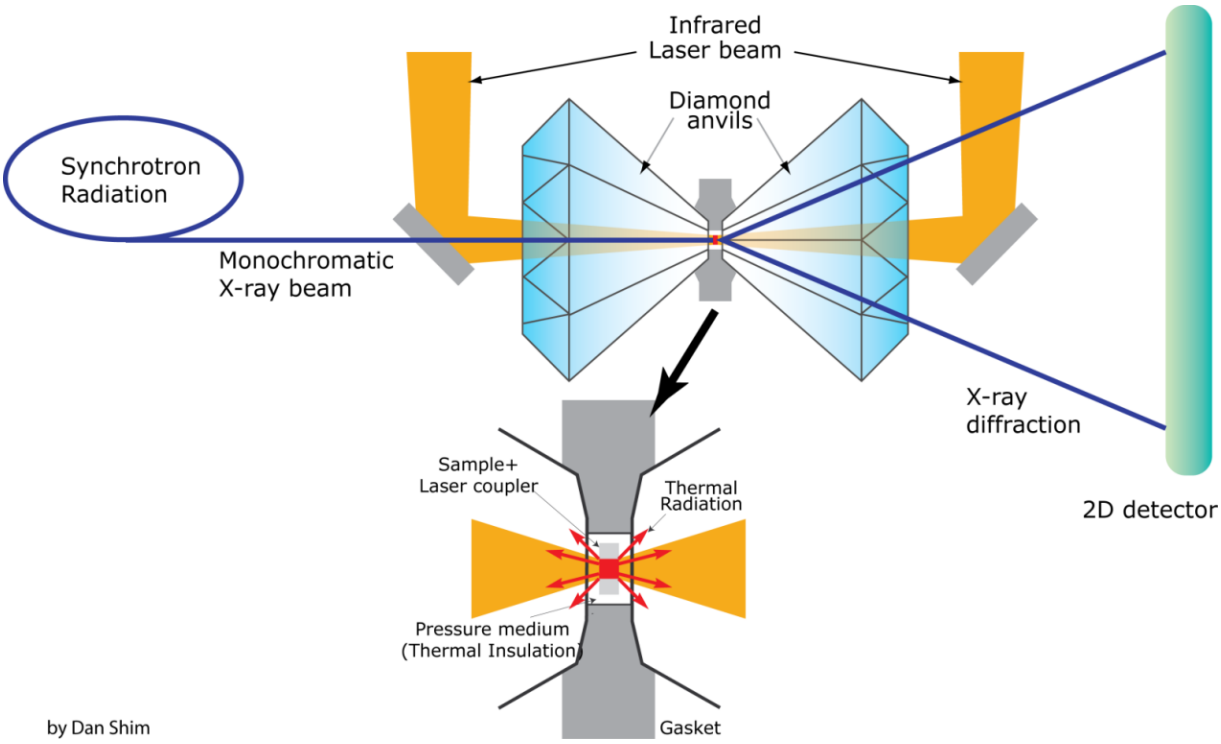

Figure 5.1 Schematic diagram of *in situ* X-ray diffraction with double-sided laser heating (photo courtesy of S.-H. Dan Shim).

5.3 Results and discussions

5.3.1 Melting curve of Na_2CO_3

The melting curve of Na_2CO_3 was determined between 3 and 18 GPa. Similarly with phenomena (Fig. 4.2) happened with melting of $CaCO_3$, we saw a rise in the current during heating from a few μA at temperatures below 1000 K to a few hundred μA upon melting. Assuming that melting leads to the sharpest rise in the measured current, we took the starting point of the steepest segment of the current-temperature curve as the melting point. As the heating cycle was repeated multiple times in the same experiment, melting was detected within ± 5 K. The measured melting temperatures from duplicate experiments at the same condition agree within ± 35 K. With a steeper melting curve than NaCl at 18 GPa, the error resulted from the pressure shift upon heating should be larger than that of NaCl experiments described in Chapter III, so a maximum 2 GPa pressure shift (Fei et al. 2004a, 2004b; Leinenweber et al. 2012) cause a temperature shift of 25-30 K. The combined uncertainties in the measured melting temperature, including the precision of the type C thermocouple, the reproducibility within a single experiment and among duplicate experiments, and the pressure drift at high temperature, are estimated at ± 45 K, assuming that the sources of uncertainties are random and independent.

The melting curve of Na_2CO_3 is rather smooth over the measured pressure range and its slope becomes smaller with increasing pressure. The *in situ* X-ray diffraction experiments of Shatskiy et al. (2013) showed that β-Na_2CO_3 is the stable high pressure phase up to ~ 10 GPa. Cancarevic et al. (2006) predicted based on simulation that Na_2CO_3 would have a phase transition from β-Na_2CO_3 (C2/m) to a phase with space group P -62 m at 16 – 19 GPa. However, the smoothness of Na_2CO_3's melting curve suggests no phase transitions happens and β-Na_2CO_3

is probably stable up to 18 GPa. The melting temperature of Na_2CO_3 keeps low over the entire upper mantle pressure range compared with other carbonates (Fig. 5.6).

Table 5.1 Experimental conditions and results of high pressure melting experiments

Run ID	Sample	Pressure, GPa	Melting Temperature, °C	Solidification temperature, °C
051114_5	Na_2CO_3	3.0[1]	1268 ± 45[2]	
		4.5	1343 ± 45	
		6.0	1403 ± 45	
		7.5	1453 ± 45	
		9.0	1493 ± 45	
		10.5	1521 ± 45	
		12.0	1548 ± 45	
		13.5	1574 ± 45	
		15.0	1590 ± 45	
080414_5	Na_2CO_3	3.0	1249 ± 45	
		6.0	1436 ± 45	1423
		9.0	1541 ± 45	
		12.0	1612 ± 45	
		15.0	1665 ± 45	
		18.0	1709 ± 45	1708
081814_5	K_2CO_3	3.0	1342 ± 85	
		4.5	1447 ± 85	
		6.0	1518 ± 85	
		9.0	1613 ± 85	1613
		12.0	1788 ± 85	
		15.0	1929 ± 85	
		18.0	2041 ± 85	2037
		20.0	2106 ± 85	
090214_5	K_2CO_3	3.0	1348 ± 85	
		4.5	1475 ± 85	1469
		6.0	1557 ± 85	
		9.0	1687 ± 85	
		10.0	1746 ± 85	
		12.0	1876 ± 85	
		16.0	2043 ± 85	
		20.0	2208 ± 85	2201

[1] The pressure uncertainty can be 2 GPa at maximum at ~20 GPa and generally smaller than 2 GPa at lower pressure;
[2] The temperature error includes the error caused by pressure shift during heating.

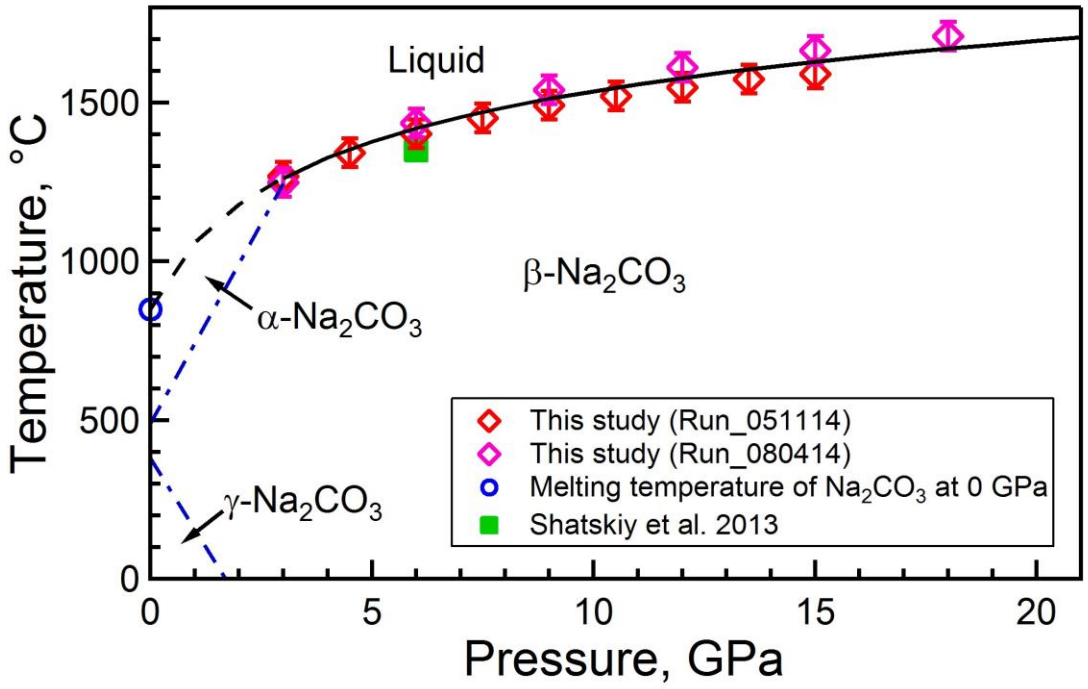

Figure 5.2 Melting curve of Na_2CO_3. The blue dash-dot lines are phase boundaries between α-Na_2CO_3, β-Na_2CO_3 and γ-Na_2CO_3 proposed by Shatskiy et al. (2013). The black solid curve is the polynomial fit of our data. The black dash line is the interpolated melting curve based on our data and ambient temperature melting temperature. The error bar of our data is ± 45 °C.

5.3.2 Melting curve of K_2CO_3

The melting temperatures of K_2CO_3 were determined between 3 and 18 GPa (Table 5.1). Also similar with phenomena (Fig. 4.2) happened with melting of $CaCO_3$ and Na_2CO_3, melting led a sharp rise in the measured current, we took the starting point of the steepest segment of the current-temperature curve as the melting point. As the heating cycle was repeated multiple times in the same experiment, melting was detected within ± 5 K. The measured melting temperatures from duplicate experiments at the same condition agree within ± 45 K. The melting curve of K_2CO_3 is much steeper than NaCl, so the error resulted from the pressure shift upon heating should be larger that of NaCl experiments described in Chapter III, so a maximum 2 GPa pressure shift (Fei et al. 2004a, 2004b; Leinenweber et al. 2012) cause a temperature shift up to 75 K. The combined uncertainties in the measured melting temperature, including the precision of the type C thermocouple, the reproducibility within a single experiment and among duplicate experiments, and the pressure drift at high temperature, are estimated at ± 85 K, assuming that the sources of uncertainties are random and independent.

The melting temperature of K_2CO_3 is similar to that of Na_2CO_3 below 9 GPa. However, above 9 GPa, the slope of the melting curve of K_2CO_3 becomes rather steep, which is most likely caused by a high pressure phase transition of K_2CO_3 at 9 GPa. Based on Clapeyron equation, a prominent volume reduction of solid K_2CO_3 is associated with the phase transition (Walker et al. 1988). Around 15 GPa, the melting temperature of K_2CO_3 has exceeded that of $MgCO_3$. This high melting temperature of K_2CO_3 above 15 GPa indicates a fast increase of eutectic temperature of K_2CO_3 with $MgCO_3$ and $CaCO_3$ above 9 GPa. Shatskiy et al. (2013a, 2013b) found almost identical binary phase diagrams for Na_2CO_3+$MgCO_3$ and K_2CO_3+$MgCO_3$, which is not surprise at 6.5 GPa, because K_2CO_3 and Na_2CO_3 have similar geochemical behavior and

melting temperature. But above 9 GPa, the melting temperature of K_2CO_3 increases much faster than Na_2CO_3, so the eutectic melting behavior of K_2CO_3 should be differentiated from that of Na_2CO_3. It would be expected above 9 GPa, sodium would be more strongly partitioned into the melt than potassium. Actually, Litasov et al. (2013) found that solidus and stability field of potassium bearing carbonates become much higher in temperature than sodium bearing carbonates above 15 GPa. Along with a single melting temperature measurement of Shatskiy (2013b) at 6.5 GPa, our results were ~180 °C higher than results of Liu et al. (2007) at 3 GPa, and the melting curve of Liu's seems already flattened at 3 GPa. This discrepancy is most likely caused by a phase transition around 3 GPa, as we have demonstrated later. The phase transition increases the slope of the melting curve above 3 GPa. Liu et al. may just measure the melting temperature before the phase transition, and we with Shatskiy et al. (2013b) measured the melting temperature after the phase transition.

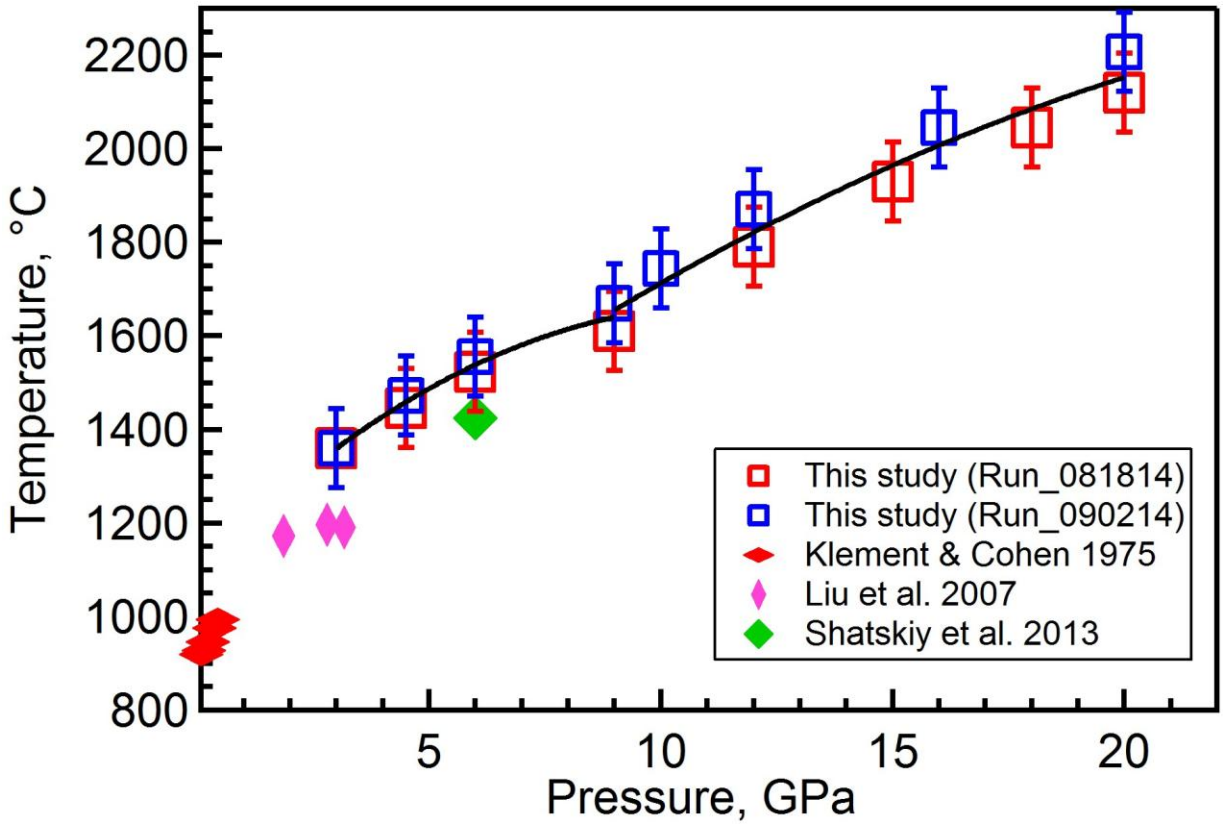

Figure 5.3 Melting curve of K_2CO_3. The black curves are piece-wise polynomial fits of our data at 3-9 GPa and 9-20 GPa. The error bar of our data is ± 85 °C.

5.3.3 *In situ* X-ray diffraction and phase diagram of K_2CO_3

The X-ray diffraction patterns (Fig. 5.4) show that before compression, the K_2CO_3 was in γ-K_2CO_3 phase (Müller, 2013). After compressed to ~3 GPa and heated to over 1000 °C, K_2CO_3 turned into a new phase. The new phase is in low symmetry (monoclinic or orthorhombic), but cannot be indexed by either β-K_2CO_3 or α-K_2CO_3. When compressed to above 4 GPa, K_2CO_3 transformed to another new phase, which is likely in a hexagonal symmetry. In the end, when the sample was compressed up to ~ 25 GPa, K_2CO_3 had another phase transition. All 3 new phases about K_2CO_3 were not documented before. And their crystal structures needs to be solved. Cancarevic et al. (2006, 2007) predicted K_2CO_3 would have a $CO_3^{2-} \rightarrow CO_4^{4-}$ transition at ~ 23 GPa, if the phase transition in our experiment around 20 GPa is this phase transition, K_2CO_3 is the carbonate with the lowest transition pressure to orthocarbonate.

Table 5.2 List of *in situ* X-ray diffraction experiments

Experiment ID	Pressure, GPa	Temperature, °C	Crystal phase*
K2CO3_1	3.7-4.1	1066-1057	New phase 1
K2CO3_2	4.8-6.5	1047-1267	New phase 2
K2CO3_3	7.3-10.1	958-1451	New phase 2
K2CO3_4	9.9-12.8	956-1291	New phase 2
K2CO3_5	24.66-27.1	927-1779	New phase 3

*See Figure 5.4, 5.5.

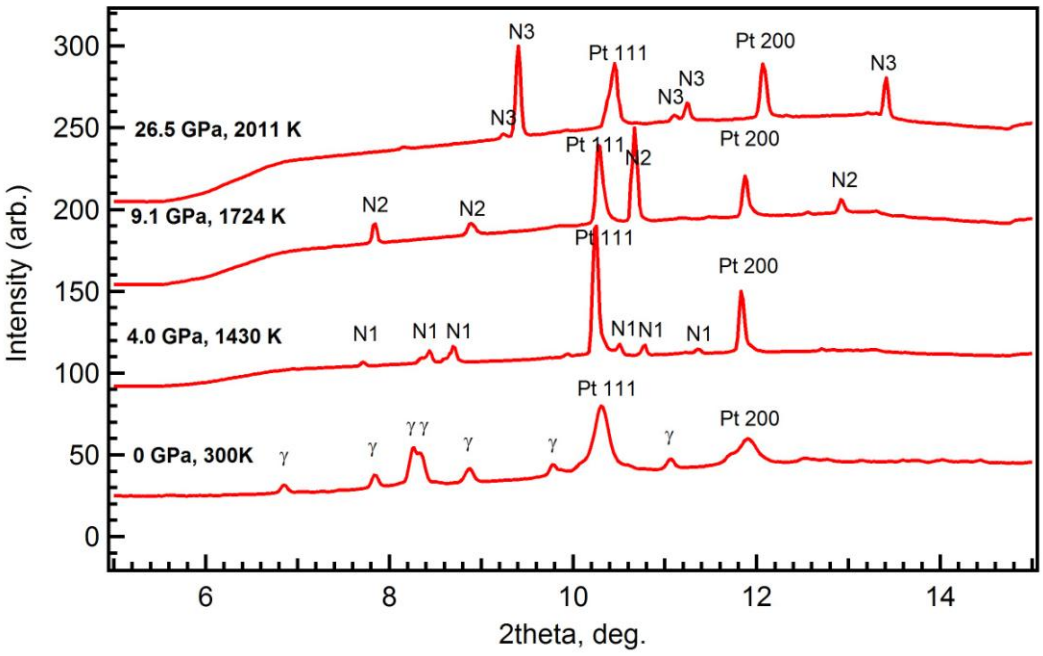

Figure 5.4 X-ray diffraction patterns of K_2CO_3 at different temperature and pressure conditions. The temperature and pressure of every pattern are indicated in the figure. The pattern at the bottom has been identified as that of γ-K_2CO_3. And the other 3 pattern are the 3 new high pressure K_2CO_3 phases. (Pt-Platinum; γ-γ K_2CO_3; N1-new phase 1; N2-new phase 2; N3-new phase 3)

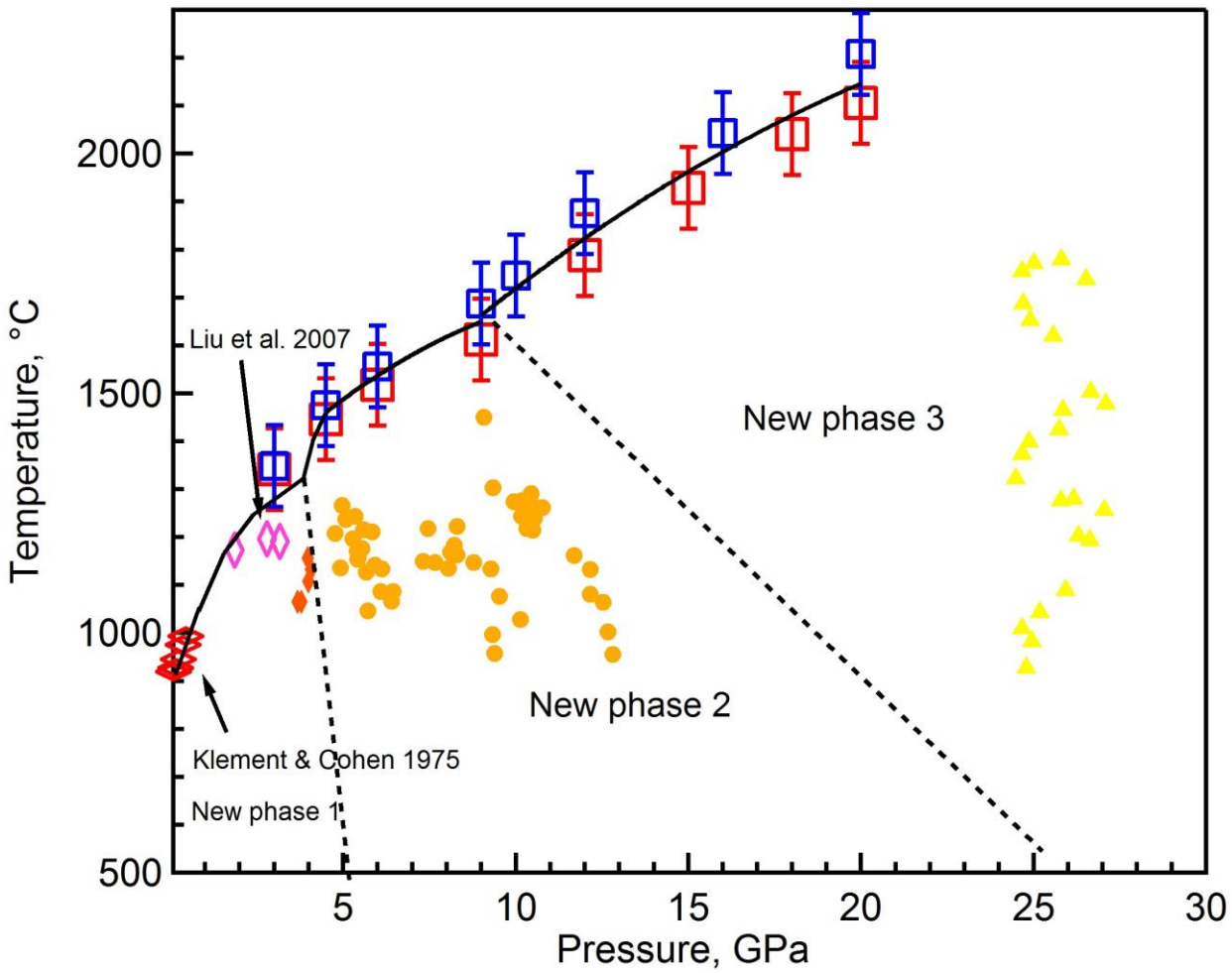

Figure 5.5 Phase diagram based on *in situ* X-ray diffraction experiments. All solid symbols represent the pressure and temperature conditions of an X-ray diffraction measurement, and the different shapes of the solid symbols denote different high pressure phases of K_2CO_3 identified from X-ray diffraction patterns. All open symbols are temperature measurements (Liu et al. 2007; Klement and Cohen, 1975). The dashed lines are the proposed phase boundaries of K_2CO_3.

5.4 Implications

Compared with melting curves of other carbonates (Fig. 5.6), the melting curves of Na_2CO_3 and K_2CO_3 are lower than those of $MgCO_3$ and $CaCO_3$, similar to that of FeCO3. This is consistent with the experimental results (Ghosh et al., 2009) that adding K_2CO_3 and Na_2CO_3 lowers the solidus of carbonated peridotite and produces alkaline-rich melt in low degree partial melting. However, the melting temperature of K_2CO_3 exceeds that of $MgCO_3$ above 15 GPa, which indicates K_2CO_3 would not partition into melt so easy in the depth of the transition zone. Even there seem no stable silicate minerals to host potassium in the transition zone, with such a high melting temperature potassium maybe exist as carbonate form in the transition zone. If some K_2CO_3 can survive the decarbonation during subduction, these K_2CO_3 would become more and more stable with increasing pressure. Reversely, if some K_2CO_3 in the transition zone rises with upwelling mantle, their eutectic melting temperature may decrease rapidly with decreasing pressure, which will lead to a speeded melt above a certain depth. Experiments to measure eutectic melting temperatures of potassium bearing carbonated mantle rock above 15 GPa can test this scenario.

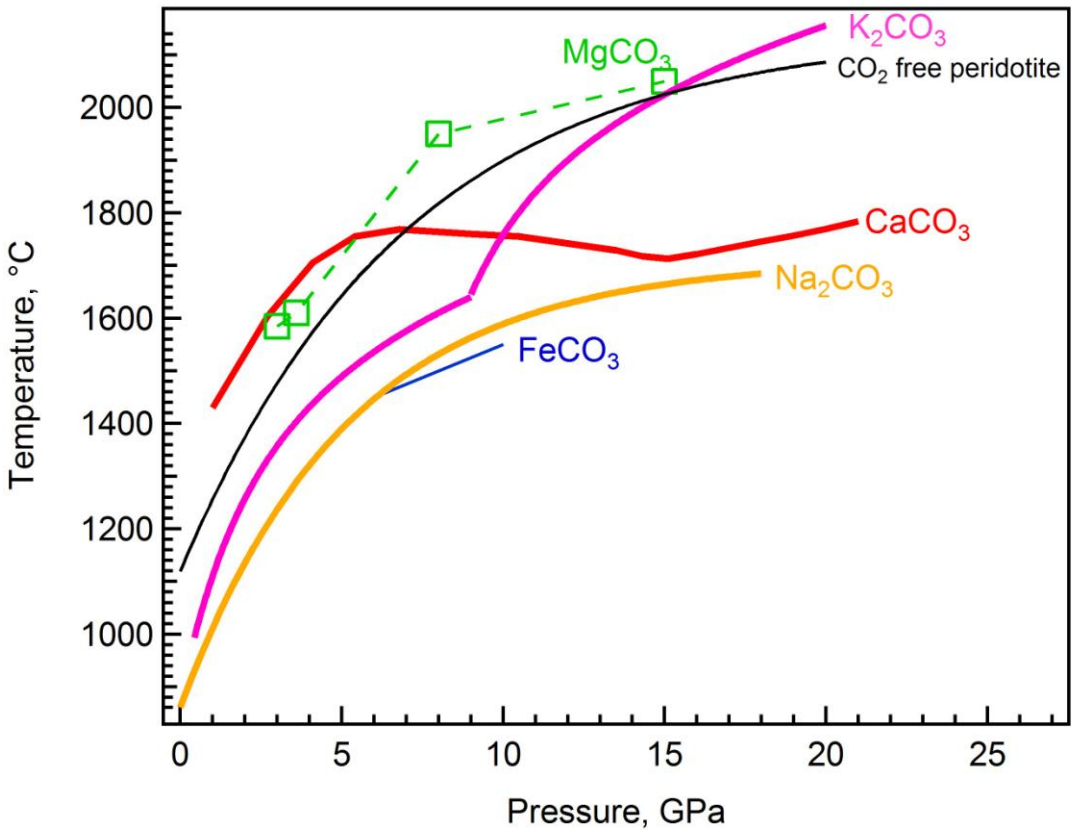

Figure 5.6 Comparison of melting curves of $MgCO_3$ (Irving and Wyllie 1975; Katsura and Ito, 1990), $CaCO_3$ (Chapter IV), FeCO3 (Tao et al. 2013), Na2CO3 and K2CO3. The Black curve is the solidus of dry peridotite (Herzberg et al., 2000).

References

Cancarevic, Z.P., Schon, J.C., and Jansen, M. (2006) Alkali metal carbonates at high pressure. Zeitschrift für anorganische und allgemeine Chemie. 632, 1437–1448.

Cancarevic, Z.P., Schon, J.C. and Jansen, M. (2007) Possible existence of alkali metal orthocarbonates at high pressure. Chemistry – A European Journal, 13, 7330–7348.

Dasgupta, R., and Hirschmann, M.M. (2006) Melting in the Earth's deep upper mantle caused by carbon dioxide: Nature, 440, 659–662.

Errandonea, D., Somayazulu, M., and Häusermann, D., and Mao, H.K. (2003) Melting of tantalum at high pressure determined by angle dispersive X-ray diffraction in adouble-sided laser-heated diamond-anvil cell. Journal of Physics: Condensed Matter, 15, 7635-7649.

Fei, Y., Li, J., Hirose, K., Minarik, W., Van Orman, J., Sanloup, C., Van Westrenen, W., Komabayashi, T., and Funakoshi, K. (2004a) A critical evaluation of pressure scales at high temperatures by *in situ* X-ray diffraction measurements. Physics of the Earth and Planetary Interiors, Vol. 143-144, 515-526.

Fei, Y., Van Orman. J., Li, J., Van Westrenen, W., Sanloup, C., Minarik, W., Hirose, K., Komabayashi, T., Walter, M., and Funakoshi, K. (2004b) Experimentally determined postspinel transformation boundary in Mg_2SiO_4 using MgO as an internal pressure standard and its geophysical implications. Journal of Geophysical Research: Solid Earth, 109(B2), B2305.

Fei, Y., Ricolleau, A., Frank, M., Mibe, K., Shen, G., and Prakapenka, V. (2006) Toward an internally consistent pressure scale, Proceedings of the National Academy of Sciences of the United States of America, 104, 9182-9186,

Green, D.H., and Wallace, M.E. (1988) Mantle metasomatism by ephemeral carbonatite melts. Nature, 336, 459–462.

Ghosh, S., Ohtani, E., Litasov, K.D., Terasaki, H. (2009) Solidus of carbonated peridotite form 10 to 20 GPa and origin of magnesiocarbonatite melt in the Earth's deep mantle. Chemical Geology, 262, 17-28.

Hammersley, A.P., Svensson, S.O., Hanfland, M., Fitch, A.N., and Hausermann, D. (1996) Two-dimensional detector software: from real detector to idealized image or two-theta scan. High Pressure Research, 14, 235.

Irving, A. J., and P. J. Wyllie (1975), Subsolidus and melting relationships for calcite, magnesite and join $CaCO_3$-$MgCO_3$ to 36 kb, Geochim. Cosmochim. Acta, 39(1), 35-53.

Jones, A.P., Genge, M., and Carmody, L. (2013) Carbonate melts and carbonatites. Reviews in Mineralogy & Geochemistry, 75, 289-322.

Katsura, T., and Ito, E. (1990) Melting and subsolidus phase relations in the $MgSiO_3$-$MgCO_3$ system at high pressures – Implications to evolution of the Earth's atmosphere. Earth and Planetary Science Letters, 99, 110-117.

Klement, W., and Cohen, L.H. (1975) Solid–solid and solid–liquid transitions in K_2CO_3, Na_2CO_3 and Li_2CO_3—investigations to greater than – 5 kbar by differential thermal analysis—thermodynamics and structural correlations. Ber Bunsenges 79, 327–334.

Leinenweber, K.D., Tyburczy, J.A., Sharp, T.G., Soignard, E., Diedrich, T., Petuskey, W.B., Wang, Y., and Mosenfelder, J.L. (2012) Cell assemblies for reproducible multi-anvil experiments (the COMPRES assemblies). American Mineralogist, 97, 353-368.

Liu, Q., Tenner, T.J., and Lange, R. (2007) Do carbonate liquids become denser than silicate liquids at pressure? Constraints from fusion curve of K_2CO_3 to 3.2 GPa. Contributions to Mineralogy and Petrology, 153, 55-66.

Litasov, K.D., and Ohtani, E. (2009) Solidus and phase relations of carbonated peridotite in the system CaO-Al_2O_3-MgO-SiO_2-Na_2O-CO_2 to the lower mantle depths: Physics of the Earth and Planetary Interiors, 177, 46–58,

Müller, U. (2013) Symmetry relationships between crystal structures: applications of crystallographic group theory in crystal chemistry. Cambridge University Press, 160pp.

Schrauder, M., and Navon, O. (1994) Hydrous and carbonatitic mantle fluids in fibrous diamonds from Jwaneng, Botswana. Geochimica et Cosmochimica Acta, 58, 761–771.

Shatskiy, A., Gavryushkin, P.N., Sharygin, I.S., Litasov, K.D., Kupriyanov, I.N., Higo, Y., Borzdov, Y.M., Funakoshi, K., Palyanov, Y.N., Ohtani, E. (2013a) Melting and subsolidus phase relations in the system Na_2CO_3–$MgCO_3$±H_2O at 6 GPa and the stability of $Na_2Mg(CO_3)_2$ in the upper mantle. American Mineralogist, 98, 2172–2182.

Shatskiy, A., Sharygin, I.S., Gavryushkin, P.N., Litasov, K.D., Borzdov, Y.M., Shcherbakova, A.V., Higo, Y., Funakoshi, K., Palyanov, Y.N., and Ohtani, E. (2013b) The system K_2CO_3–$MgCO_3$ at 6 GPa and 900–1450 °C. American Mineralogist, 98, 1593–1603.

Tao, R., Fei, Y., and Zhang, L. (2013) Experimental determination of siderite stability at high pressure. American Mineralogist, 98, 1565-1572.

Walker, D., Agee, C.B. and Zhang, Y. (1988) Fusion curve slope and crystal/liquid buoyancy. Journal of Geophysical Research, 93, 312-323.

Chapter VI

Phase relations of dense hydrous germanates (DHMG)

6.1 Introduction

Dense hydrous magnesium silicates (DHMS) are a group of minerals that contain chemical bound water and can be stable in mantle pressure temperature conditions. They include a series of minerals with alphabet names, such as phase A, phase B (Ringwood and Major, 1967), phase superhydrous B (Gasparik, 1990), phase D (Liu, 1986), phase E (Kudoh et al. 1993), phase H (Nishi et al. 2014) and δ phase (Suzuki et al. 2000) and etc. These DHMS can carry water in their crystal structures and survive the dehydration associated with subduction. They can take water all the way to the lower mantle (Ohtani et al. 2014). The nominally anhydrous minerals, wadsleyite and ringwoodite, were found to able to contain up to a few weight percent H_2O in their structures (Smyth, 1987; Kohlstedt et al. 1996). The role of DHMS in mantle hydrogen cycle was studied through their phase equilibrium (e.g. Irifune et al. 1998; Ohtani et al. 2000; Shieh et al. 2000; Angel et al. 2001), crystal structures (e.g. Yang et al. 1997; Bindi et al., 2014) and physical properties (e.g. Sanchez-Valle et al. 2008; Mao et al. 2012). However, studies about rheology, calorimetry and neutron diffraction of DHMS are limited by current technology in which these experiments require large sample volume (Dupas-Bruzek et al., 1998; Rubie and Ross II, 1994; Klotz, 2013). Syntheses of most DHMS require more than 10 GPa pressure, which inevitably limits the sample volume to a few mm^3. The recently discovered phase H (Nishi et al.

2014) requires up to 40 GPa to synthesize, so the studies of this phase are limited in only a few labs.

One way to circumvent this limited volume problem is to use germanium instead of silicon. Germanates are widely used as analogues of silicates in studies of high pressure mineral phases because germanium has similar chemical characteristics with silicon, but its larger ionic radius makes germanates the lower pressure analogues of their silicate equivalents. Dachille and Roy (1959) used Mg_2GeO_4 to study the olivine → spinel transition. More recently Hirose et al. (2005) used $MgGeO_3$ to study perovskite → post-perovksite transition. In these cases germanate analogues can be synthesized under considerable lower pressure and in large volume, and their properties can be adequately projected to those equivalent silicates.

Hydrous germanantes have been used to imitate DHMS. Blanchard et al. (2005a, 2005b) modeled OH defects in germanium ringwoodite and suggested using germanium analogues to study the protonation of nominally anhydrous minerals. Thomas et al. (2008) synthesized germanium analogues of anhydrous B and superhydrous B to study the protonation of dense hydrous magnesium silicates (DHMS). To date only germanium anhydrous B (e.g., Von Dreele et al. 1970), germanium ringwoodite containing 5 to 10 ppm water by weight (Hertweck and Ingrin, 2005) and germanium superhydrous B (Thomas et al. 2008) have been synthesized and phase relations among germanium analogues of DHMS are not clear. The lack of knowledge limits the applications of germanium analogues of DHMS. So it is necessary to study the phase relations of germanium analogues of DHMS over a large pressure and temperature domain. The knowledge about germanium analogues of DHMS will contribute fundamental knowledge to future studies using the germanium analogues of DHMS, and will provide insight into the effect

of Ge-Si substitution of structural transformations in an important group of silicate phases in the Earth's mantle.

In this chapter, results from *in situ* X-ray diffraction experiments with hydrothermal diamond anvil cells on hydrous germanates are reported. The phase diagram of Mg_2GeO_4+H_2O is proposed based on X-ray diffraction results.

6.2 Method

Angular dispersive X-ray diffraction experiments on Mg_2GeO_4+H_2O under high pressure with resistively heated hydrothermal diamond anvil cell (with cutlet size of 300 μm) were conducted at Beamlines 16-ID-B and 16-BM-D of HPCAT, the Advanced Photon Source at the Argonne National Lab (Table 6.2). X-ray was monochromatized to a wavelength of 0.4066 μm (16-ID-B) or 0.4246 μm (16-BM-D) and focused to an area of 5 μm by 10 μm. Diffraction images were recorded over 0.1s with a Pilatus-1M pixel array detector or 1-10s with a MarCCD and were integrated and corrected for distortions using the FIT2D software (Hammersley et al. 1996).

The sample Mg_2GeO_4 was synthesized by multi-anvil apparatus at 6 and 9 GPa, 800 °C (Table 6.1, Fig. 6.3) with a starting material of GeO_2 + $Mg(OH)_2$. The $Mg_2GeO_4$from high pressure syntheses were 200-500 μm euhedral crystals and their compositions were checked by electron microprobe at the EMAL of the University of Michigan. Mg_2GeO_4 was loaded into rhenium gaskets with a pressure chamber of 180 μm in diameter and 40-50 μm thick. Excess amount of water and a small amount of gold power were loaded as well.

Hydrothermal diamond anvil cells used in this study were round Bassett-type (Bassett et al. 1993). Samples were resistively heated by two heaters attached onto the diamonds. Temperatures

were determined by two type-K thermocouples attached to two diamonds. The pressure was determined by the diffraction lines of gold powder in the sample chamber based on Fei et al.'s EOS (2007). The pressure error was ±1 GPa based on the standard deviation of the lattice parameter.

In a typical experiment, the sample was compressed to a target pressure and then temperature was raised at a rate of 10-20 °C/min. On route of heating, X-ray diffractions were taken every 50-100 °C.

6.3 Results and disscusions

From the X-ray diffraction patterns (Fig. 6.1, Fig. 6.2), reactions and phase transitions of Mg_2GeO_4+H_2O system were found. The phase diagram about the stability region of DHMG minerals is presented in Fig. 6.3.

Before heating, X-ray diffraction pattern indicated Mg_2GeO_4 sample was in ringwoodite (spinel) structure (Dachille and Roy, 1959). Upon heating to 300 – 400 °C, the first reaction happened: the diffraction peaks of germanium ringwoodite disappeared and new diffraction peaks emerged (Fig. 6.1, Fig. 6.2). The new diffraction peaks included two doublets at ~ 5.8 and 6.7 ° two-theta angles, which were similar with the X-ray diffraction pattern of germanium superhydrous B at ambient condition(Thomas et al. 2008), but this new phase was not persevered after heating to higher temperature, further composition analysis of this phase cannot be done. The boundary between ringwoodite and the possible germanium superhydrous B almost overlaps with the phase boundary between ice VII and H_2O fluid (Fig. 6.3). This is possibly because H_2O fluid is much easier than ice VII to react with germanium ringwoodite to form hydrous phases.

Heated to 500 – 600 °C, the sample experienced two different phase transitions depending on pressure. When the pressure was below 8 GPa, the sample had an phase transition and turned

into germanium phase D (Fig. 6.1). It was the first time that germanium phase D was discovered. X-ray diffraction peak indexing by Jade® 5.0 suggested that germanium phase D had the same space group P-31m with silicate phase D (Yang et al. 1993), and its lattice parameter was a=4.818 , c=4.164 (Å). A crystal structure refinement on germanium phase D needs to be done to get its accurate atom coordinates. When the pressure was above 8 GPa, at 500 – 600 °C, the possible germanium superhydrous B had another phase transition and became another new phase (Fig. 6.2). This new phase had similar diffraction peaks with the newly discovered silicate phase H (Nishi et al. 2014), but cannot be indexed by similar lattice parameters of silicate phase H. This is probably because the possible germanium phase H has a distorted structure of silicate phase D.

Table 6.1 List of high pressure synthesis experiments

Experiment ID	Starting materials	Pressure, GPa	Temperature, °C	Heating duration, hour	Products
091911_8	$Mg(OH)_2$+GeO_2	6.0	800	24	$MgGeO_3$(illmenite), GeO_2(rutile), H_2O
102611_8	2$Mg(OH)_2$+GeO_2 +3H_2O	6.0	800	24	Mg_2GeO_4(ringwoodite), $MgGeO_3$(illmenite), $Mg(OH)_2$(brucite), H_2O
041412_8	2$Mg(OH)_2$+GeO_2	9.0	800	24	Mg_2GeO_4(ringwoodite), $MgGeO_3$(illmenite), $Mg(OH)_2$(brucite), H_2O
052512_8	2$Mg(OH)_2$+GeO_2 + excess H_2O	9.0	600	24	$MgGeO_4H_2$(phase H?), $Mg(OH)_2$(brucite), H_2O

Table 6.2 Conditions and results of high pressure phase equilibrium experiments on dense hydrous germanates

Experiment ID	Starting materials	Pressure, GPa	Temperature, °C	Final equilibrium phases
MgGeOH_P1	Mg_2GeO_4+H_2O	0-3.8	25-600	phase D + brucite
MgGeOH_S1	Mg_2GeO_4+H_2O	4.0-7.4	25-600	phase D + brucite
MgGeOH_S2	Mg_2GeO_4+H_2O	2.1-18.5	25-500	Ringwoodite + H_2O
MgGeOH_S3	Mg_2GeO_4+H_2O	8.9-10.7	25-600	phase H(?) +brucite
MgGeOH_S4	Mg_2GeO_4+H_2O	9.3-14.6	30-570	phase H(?) +brucite
MgGeOH_S5	Mg_2GeO_4+H_2O	5.0-10.5	30-623	phase H(?) +brucite
MgGeOH_S6	Mg_2GeO_4+H_2O	2.7-8.9	23-615	phase D + brucite
MgGeOH_S7	Mg_2GeO_4+H_2O	0.78-8.9	25-611	superhydrous B(?)
MgGeOH_S8	Mg_2GeO_4+H_2O	11.1-36.0	30-592	ringwoodite + H_2O

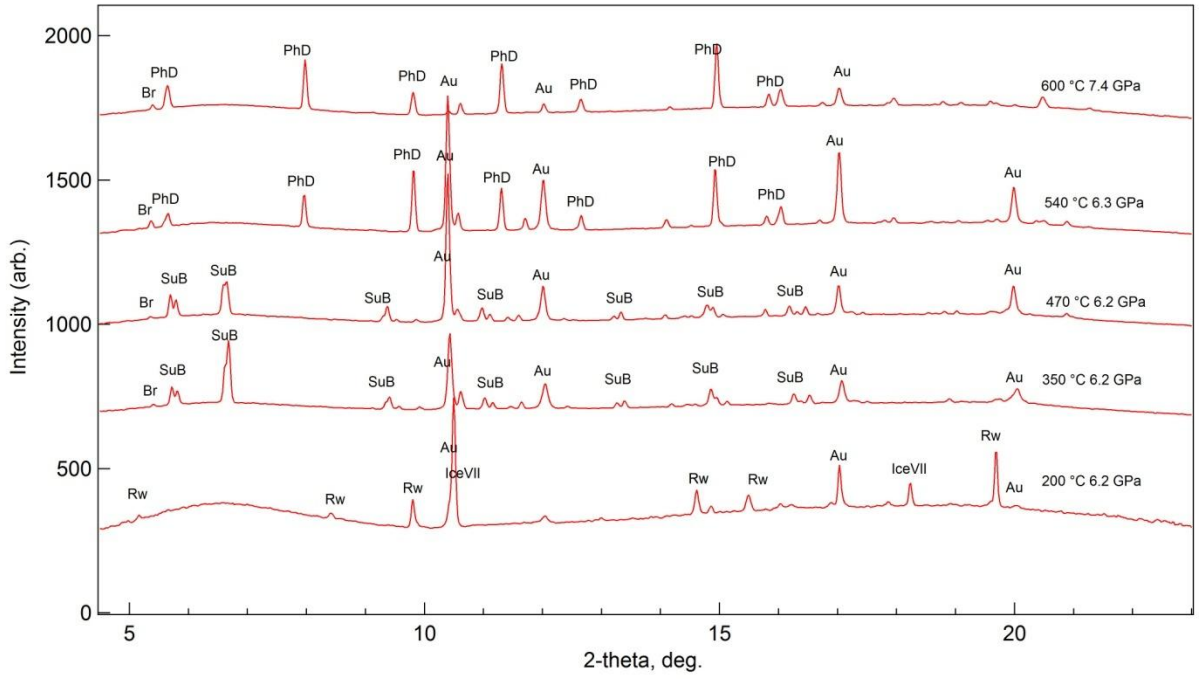

Figure 6.1 X-ray diffraction patterns of Mg_2GeO_4+H_2O system below 8 GPa. (Br-brucite, Rw-germanium ringwoodite, PhD-germanium phase D, Au-gold, IceVII-ice VII, SuB-germanium superhydrous B)

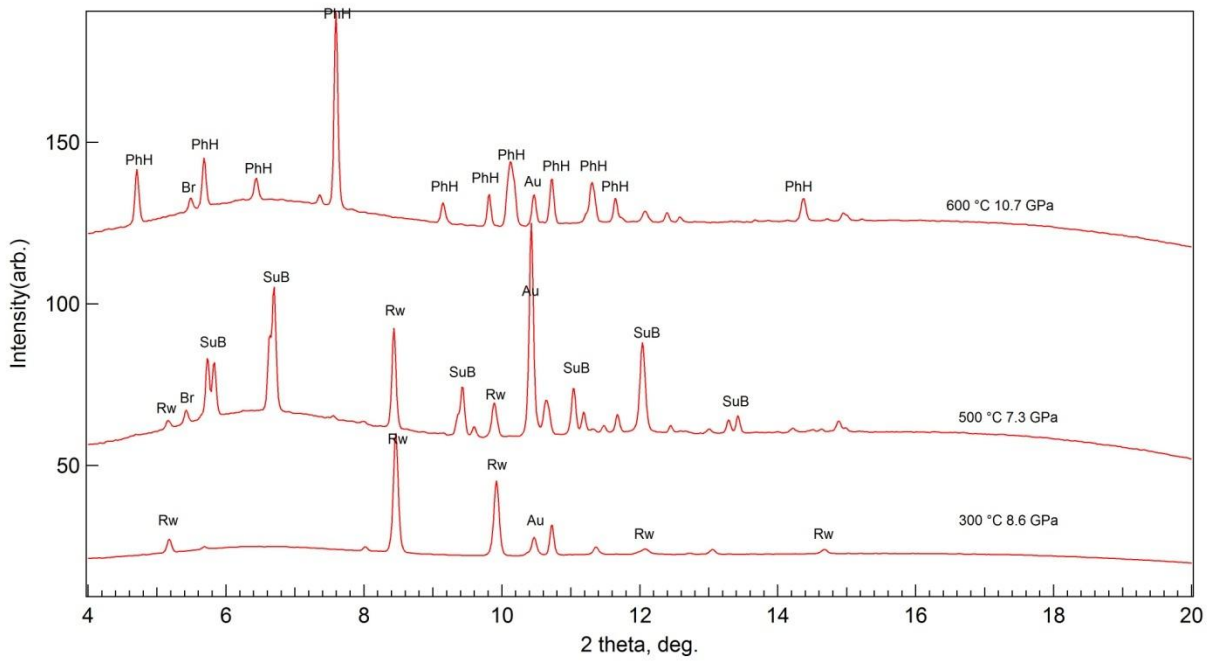

Figure 6.2 X-ray diffraction patterns of Mg_2GeO_4+H_2O system above 8 GPa. (Br-brucite, Rw-germanium ringwoodite, PhH-germanium phase H, Au-gold, SuB-germanium superhydrous B)

All the experiments stopped around 600 °C because softening of the rhenium gaskets at this temperature caused pressure drops. The samples were quenched by turning off the power. Both germanium phase D and possible germanium phase H can be quenched to ambient pressure and temperature. The multi-anvil syntheses by us and Thomas et al. (2008) had starting materials with similar bulk compositions, but at temperatures ≥ 800 °C (Fig. 6.3) the products of these syntheses were Mg_2GeO_4 ringwoodite and liquid water. However, a multi-anvil synthesis by us at 9 GPa and 600 °C produced the possible germanium phase H. This indicates germanium phase D and possible phase H are only stable below 800 °C. Above 800 °C, they will lose water and turn to Mg_2GeO_4 ringwoodite.

The germanium phase D and possible phase H has the same phase transition sequence as silicate phase D and phase H (Ohtani et al. 2014), but at much lower pressure (Fig. 6.4). Germanium phase D only requires at most 6 GPa to be synthesized, comparing with at least 20 GPa of silicate phase D. With only 6 GPa, germanium phase D can synthesized in 0.1 -1 gram quantity, which opens a lot of experimental possibilities, such as neutron diffraction, accurate composition analysis, calorimetry, etc.

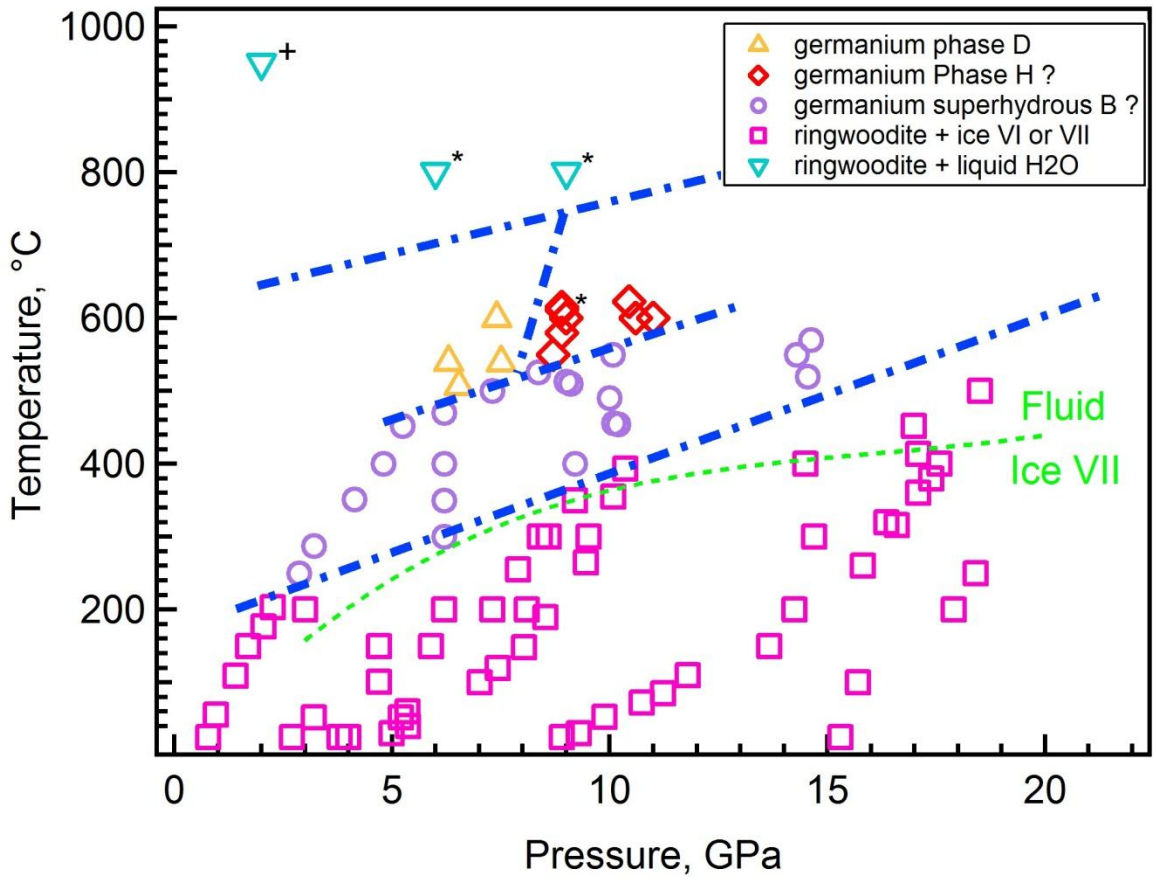

Figure 6.3 Phase diagram of Mg_2GeO_4+H_2O under high pressure and temperature. The cross denotes multi-anvil synthesis of Thomas et al. (2012); the stars denote multi-anvil syntheses of this study; the green dashed line is the phase boundary between ice VII and fluid (Fei et al. 1993).

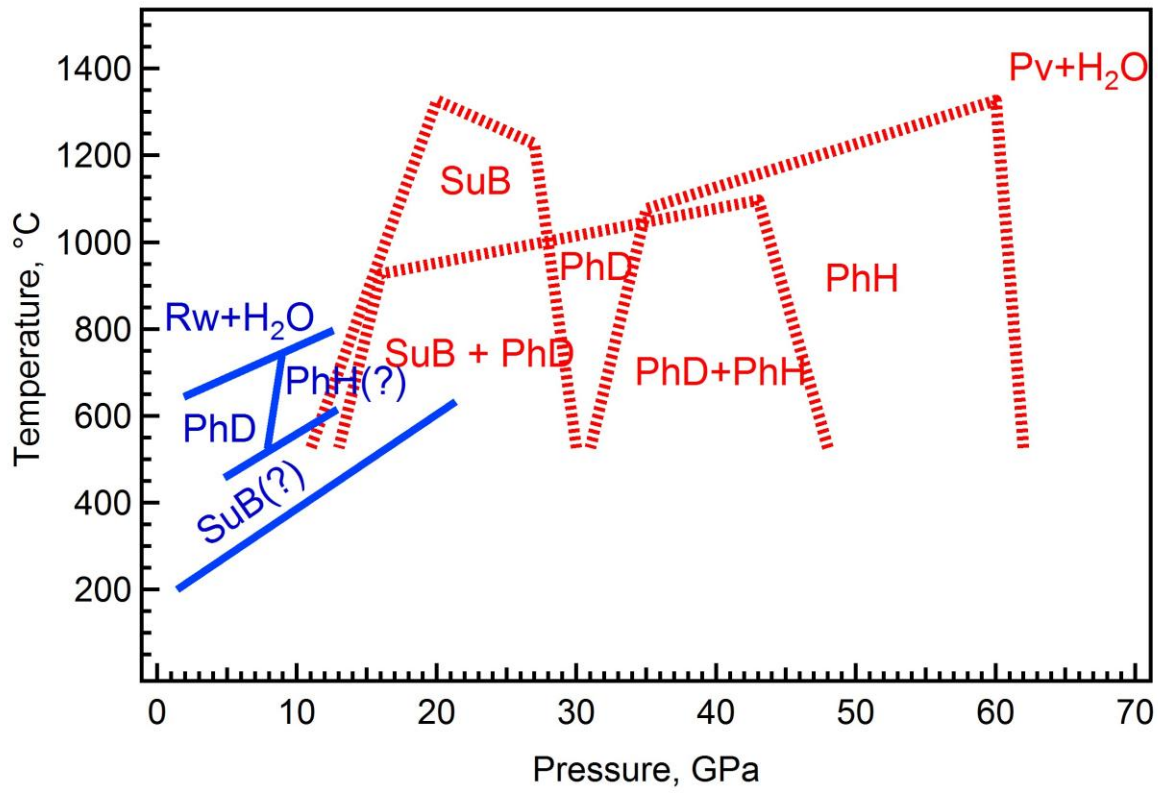

Figure 6.4 Comparison of stability ranges of dense hydrous magnesium germanates (DHMG) and dense hydrous magnesium silicates (DHMS). Red dotted lines draw stability boundary for DHMS (Ohtani et al. 2014); blue solid lines draw for DHMG. (Rw-ringwoodite; SuB-superhydrous B; phD-phase D; PhH-phase H; Pv-perovskite)

References

Angel, R.J., Forst, D.J., Ross, N.L., and Hemley, R.J. (2001) Stabilities and equations of state of dense hydrous magnesium silicates. Physics of the Earth and Planet Interiors,127, 181-196.

Bassett, W.A., Shen, A.H., Bucknum, M., and Chou, I. (1993) A new diamond anvil cell for hydrothermal studies to 2.5 GPa and from -190 to 1200 °C. Review of Scientific Instruments, 64, 2340-2345.

Bindi, L., Nishi, M., Tsuchiya, J., and Irifune, T. (2014) Crystal chemistry of dense hydrous magnesium silicates: The structures of phase H, $MgSiH_2O_4$, synthesized at 45 GPa and 1000 °C. American Mineralogist, 99, 1802-1805.

Blanchard, M., Wright, K., and Gale, J.D. (2005a), Atomistic simulation of Mg_2SiO_4 and Mg_2GeO_4 spinels: A new model. Physics and Chemistry of Minerals, 32, 332–338.

——— (2005b), A computer simulation study of OH defects in Mg_2SiO_4 and Mg_2GeO_4 spinels. Physics and Chemistry of Minerals, 32, 585–593.

Dachille, D., and Roy, R. (1959) The spinel–olivine inversion in Mg_2GeO_4, Nature,183, 1257.

Dupas-Bruzek, C., Tingle, T.N., Green II, H.W., Doukhan, N., and Doukhan, J.-C. (1998), The Rheology of Chem Minerals, 25, 501-514.

Fei, Y., Mao, H.K., and Hemley, R.J., 1993. Thermal expansivity, bulk modulus, and melting curve of H_2O-Ice VII to 20 GPa. Journal of Chemical Physics 99, 5369–5373.

Fei, Y., Ricolleau, A., Frank, M., Mibe, K., Shen, G., and Prakapenka, V. (2006) Toward an internally consistent pressure scale, Proceedings of the National Academy of Sciences of the United States of America, 104, 9182-9186,

Hammersley, A.P., Svensson, S.O., Hanfland, M., Fitch, A.N., and Hausermann, D. (1996) Two-dimensional detector software: from real detector to idealized image or two-theta scan. High Pressure Research, 14, 235.

Hertweck, B. and Ingrin, J. (2005) Hydrogen incorporationin a ringwoodite analogue: Mg_2GeO_4 spinel. Mineralogical Magazine, 69, 337–343.

Herzberg, C., Raterron, P., Zhang, J., 2000. New experimental observations on the anhydrous solidus for peridotite KLB-1. Geochemistry Geophysics Geosystem, 1, 11. doi:10.1029/2000GC000089.

Hirose, K., Kawamura, K., Ohishi, Y.,Tateno, S., and Sata, N. (2005) Stability and equation of state of $MgGeO_3$ post-perovskite phase, American Mineralogist, 90, 262-265.

Gasparik, T. (1990) Phase relations in the transition zone. Journal of Geophysical Research, 95, 1575 l-15769.

Irifune, T., Kubo, N., Isshiki, M., and Yamasaki, Y. (1998) Phase transformations in serpentine and transportation of water into the lower mantle. Geophysical Research Letters, 25, 203-206.

Klotz, F. (2013) Techniques in High Pressure Neutron Scattering. CRC Press, 60pp.

Kohlstedt, D. L., Keppler, H. & Rubie, D. C. (1996) Solubility of water in the α, β and γ phases of $(Mg,Fe)_2SiO_4$. Contributions to Mineralogy Petrology, 123, 345–357.

Kudoh, Y., Finger, L.W., Hazen, R.M., Prewitt, C.T., Kanzaki, M., and Veblen, D.R. (1993) Phase E: a high pressure hydrous silicate with unique crystal chemistry. Physics and Chemistry of Minerals, 19, 357- 360.

Liu, L. (1986) Phase transformations in serpentine at high pressures and temperatures and implications for subducting lithosphere. Physics of the Earth and Planetary Interiors, 42, 255-262.

Mao, Z., Lin, L., Jacobsen, S.D., Duffy, T.S., Chang, Y., Smyth, J.R., Forst, D.J., Hauri, E.H., Prakapenka, V.B. (2012) Sound velocities of hydrous ringwoodite to 16 GPa and 673 K. Earth and Planetary Science Letters, 331-332, 112-119.

Nishi, M., Irifune, T., Tsuchiya, J. Tange, Y., Nishihara, Y. Fujino, K., and Higo, Y. (2014) Stability of hydrous silicate at high pressures and water transport to the deep lower mantle, Nature Geoscience, 7, 224-227.

Ohtani, E., Mizobata, H., and Yurimoto, H. (2000) Stability of dense hydrous magnesium silicate phases in the systems Mg_2SiO_4-H_2O at pressures up to 27 GPa, 27, 533-544.

Ohtani, E., Amaike, Y., Kamada, S., Sakamaki, T., and Hirao, N. (2014) Stability of hydrous phase H $MgSiO_4H_2$ under lower mantle conditions. Geophysical Research Letters, 41, 8283-8287.

Ringwood, A.E., and Major, A. (1967) High-pressure reconnaissance investigations in the system Mg_2SiO_4-MgO-H_2O Earth Planetary Science Letters, 2, 130-133.

Rubie, D.C., and Ross II, C.R. (1994) Kinetics of the olivine-spinel transformationin subducting lithosphere: experimental constraintsand implications for deep slab processes, Physics of the Earth and Planetary Interiors, 86, 223-241.

Sanchez-Valle, C., Sinogeikin, S.V., Smyth, J.R., and Bass, J.D. (2008) Sound velocities and elasticity of DHMS phase A to high pressure and implications for seismic velocities and anisotropy in subducted slabs. Physics of the Earth and Planetary Interiors, 170, 229-239.

Shieh, S.R., Mao, H., Hemley, R.J. and Ming, L. (2000) *In situ* X-ray diffraction studies of dense hydrous magnesium silicates at mantle conditions. Earth Planetary Science Letters, 177, 69-80.

Suzuki, A., Ohtani, E., and Kamada., T. (2000) A new hydrous phase δ-AlOOH synthesized at 21 GPa and 1000 °C. Physics and Chemistry of Minerals, 10, 689-693.

Smyth, J.R. (1987) Beta-Mg_2SiO_4 – a potential host for water in the mantle. American Mineralogist, 72, 1051-1055.

Thomas, S., Koch-Müller, M., Kahlenberg, V., Thomas, R., Ehede, D., Wirth, R., and Wunder, B. (2008) Protonation in germanium equivalents of ringwoodite, anhydrous phase B , and superhydrous phase B. American Mineralogist, 93, 1282-1294.

Von Dreele, R.B., Bless, P.W., Kostiner, E., and Hughes, R.E. (1970), The crystal structure of magnesium germanate: A reformulation of Mg_4GeO_6 as $Mg_{28}Ge_{10}O_{48}$. Journal of Solid State Chemistry, 2, 612–618.

Yang, H., Prewitt, C.T., and Frost D.J. (1997) Crystal structure of the dense hydrous magnesium silicate, phase D. American Mineralogist, 82, 651-6

Chapter VII

Conclusions and Future Directions

In the past two decades, advances from ocean drillings and high pressure experiments have revealed the exchange path way and flux between surface carbon and deep carbon. The developments of high pressure techniques and spectroscopy have led to discoveries of numerous high pressure mineral phases that are potentially carbon carriers in the Earth's mantle and core (Oganov et al. 2013). This dissertation focuses on the problems related to carbonate melting in the upper mantle. It addresses the issues of how to accurately measure melting temperature at high pressure and how the unique melting behaviors of pure end member carbonates influence the overall carbonate melting and carbon storage in the upper mantle. Below I summarize how my findings impact broad issues of mantle geochemical and geophysical studies and point out directions for future work on nature and dynamics of deep carbon.

7.1 Measure melting temperature at high pressure

The new experimental technique described in Chapter II and III provides an unprecedentedly accurate and efficient way to measure melting temperature in the pressure range of the upper mantle. In addition the technique used simple instruments, an AC power source and an ammeter which every laboratory can afford to have. This capacitive current based measurement can be combined with other high pressure technique, such as piston cylinder and diamond anvil cell, to further extend its working pressure range and increase its accuracy. With

this technique, the melting curve of a mineral can be measured over a large pressure range easily, and much information can be deduced from the melting curve. As described in Chapter IV and V, solid phase transitions can be identified from abnormal changes of melting curve slope, which supplements the conventional way to determine solid phase boundary by *in situ* X-ray diffraction, especially when X-ray diffraction patterns of crystals become weak at a temperature close to melting. The slope of the melting curve can also be used to estimate or calculate the density of melt under high pressure, which is difficult to measure directly. Based on Clapeyron equation, the density difference between solid and melt along melting curve is equal to the entropy change of melting multiplied by the melting curve slope. With an accurate density of the solid from X-ray diffraction experiments, a relatively accurate melt density can be calculated. The melt density upon high pressure is valuable information for building and testing theories of melt structure (Wang et al. 2014) and thermodynamic modeling of deep magma generation (Ghiorso et al. 2002).

The capacitive current based measurement can be further developed to extend the compositional and pressure range of its application. In this dissertation, all studied subjects were single pure carbonates. However, in principle this technique should also work on silicates, which are ionic crystals as well. Due to relative high viscosities of some acid silicates, the capacitive current through these silicate melts is expected to be lower than that of carbonate melts and the hysteresis of melting temperatures upon melting and cooling is also expected to be larger than that of carbonates. Similar experiments can be done on semiconductors such as iron carbides and iron sulfides to test whether this technique also works on semiconductors. Another direction of development is towards measuring the eutectic temperature of multiple component system and liquidus/solidus temperatures of solid solution. For a real mantle melting system, melting always

happens as partial melting controlled by eutectic and/or liquidus/solidus temperatures. The interactions between multiple components decide these eutectic and liquidus /solidus temperatures. However, these interactions cannot be predicted well yet. Being able to measure eutectic and liquidus/solidus temperatures provides a more direct way to study mantle melting and is also crucial for studying those interactions affecting partial melting phenomena. In this dissertation, the melting curves of $CaCO_3$, Na_2CO_3 and K_2CO_3 have been precisely determined. With other works on $FeCO_3$ (Tao et al. 2013) and $MgCO_3$ (Katsura and Ito, 1990), the melting behaviors of major carbonates under the upper mantle pressure have been figured out. There were also studies about melting of binary and ternary carbonate systems such as $MgCO_3$-$CaCO_3$(Boub et al. 2006), Na_2CO_3-$MgCO_3$ (Shatskiy et al. 2013a), K_2CO_3-$MgCO_3$(Shatskiy et al. 2013b) and etc., but these studies were limited at one pressure due to the requirement of enormous non-*in-situ* experiments to cover large pressure range. Our *in situ* technique can significantly reduce the number of experiments to study the eutectic and liquidus/solidus temperatures over a large pressure range. However, there are still a few expected problems. For example, the partial melting usually results in segregation of different components, which may render the repeated experiments inaccurate, so a way to rehomogenize the sample may be needed before repeated experiments on the same sample. Another problem may be how to distinguish solidus and liquidus temperatures from the capacitive current curve.

7.2 Melting behaviors of carbonates

The new data on melting curves of $CaCO_3$, K_2CO_3 and Na_2CO_3 described in Chapter V and VII show their unique melting behaviors, which will prompt us to rethink the distributions of

different carbonate species in the mantle. $CaCO_3$ shows a relatively low melting curve with small variations over 5-20 GPa (Fig. 5.6), which suggests melting in the transition zone.

Low velocity zones and areas from geophysical observations (Ritsema et al. 2011) may be caused by melting of carbonates, but cannot rule out other explanations such as dehydration melting (Bercovici and Karato, 2003; Schmandt et al. 2014), segregated basalt, metastability, underplating and interaction of the seismic waves with phase changes (Anderson, 2007). Another way to study melting in the transition zone is through the electrical structure by magnetotelluric measurements (e.g. Baba et al. 2006). Gaillard et al. (2008) has demonstrated the electrical structure of asthenosphere is best explained by carbonate melt. The development of magnetotelluric measurement is needed to probe deeper to the transition zone.

However, the melting curve of K_2CO_3 displays opposite behavior: its melting temperature rises very fast above 9 GPa and even catches up with the solidus temperatures of volatile free peridotite around 15 GPa (Fig. 5.6). The melting of carbonates and silicates are usually eutectic melting (Katsura and Ito, 1990). Normally the solidus temperatures of carbonated silicate rocks and partial melt composition are essentially controlled by melting phase relations in carbonates because the melting temperature of carbonates are usually much lower than those of silicates, resulting in a solidus temperature close to the melting temperature of carbonates and a eutectic melt composition dominated by carbonates (Fig. 7.1). However, the melting curve of K_2CO_3 indicates melting of K_2CO_3 in the transition zone depth may shift from K_2CO_3 dominated partial melting to silicate dominated, which suggests deep storage of K_2CO_3. The change of K_2CO_3 melting curve slope at 9 GPa may be caused by a phase transition as described in Chapter V. Because first principle calculations predicted a carbon atom coordination number change from 3 to 4 happens at around 10-20 GPa for K_2CO_3 (Cancarevic et al. 2007). This phase transition at 9-

25 GPa may be associated with carbon atom coordination change. A recent study have discovered the coordination number change in $(Mg,Fe)CO_3$ at around 80 GPa (Boulard et al. 2015). If this phase transition of K_2CO_3 is indeed related to the carbon atom coordination number change, the K_2CO_3 would be the carbonate requiring the lowest pressure to have this change, and this coordination change may be the cause of the high melting temperature of K_2CO_3. Other carbonates may also increase their melting temperatures after their carbon atom coordination change. Because X-ray diffraction does not work well for light carbon atom, infrared spectroscopy and first principle calculations are needed to find the evidence of CO_4 bounding and possible crystal structure (Boulard et al. 2015).

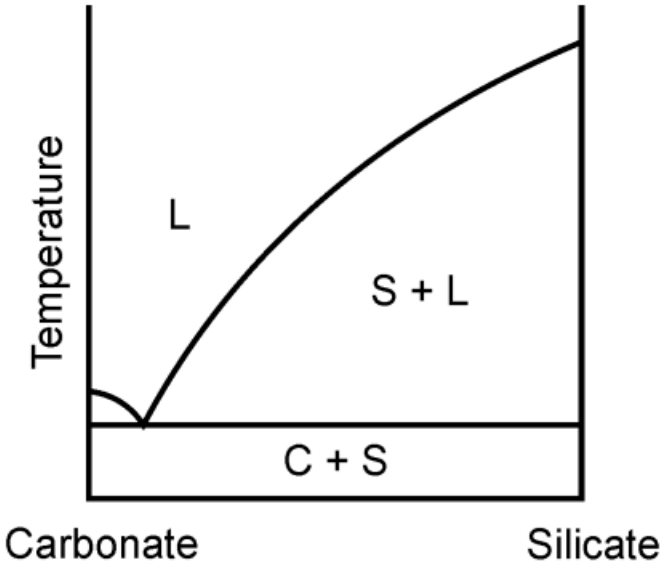

Figure 7.1 Eutectic melting of carbonated silicates (L-liquid, S-silicate, C-carbonate).

With a possible deep storage of K_2CO_3 in the transition zone or even the lower mantle, our understanding of geochemistry and thermal structure of the transition and lower mantle may be changed. Before, only hollandite II was known to be a stable potassium carrier in the lower mantle (Hirao et al. 2007), but how much its precursor K-feldspar can be subducted into the lower mantle was questionable. However, K_2CO_3 is a mineral that exists in subducted slabs and can be subdcuted into the lower mantle, so it is more likely a potassium host in the transition zone and lower mantle. ^{40}K is a major heat source of the Earth's lower mantle. If relatively large amount of heat is produced in the lower mantle due to the presence of K_2CO_3, the geodynamo model, the core formation model and the thermal history of the mantle and core need to be revised. The deep storage of K_2CO_3 may also be the cause of ultra-potassic rocks. Ultra-potassic rocks include kimberlite, lamprolite, lamprophyres, which are all deeply originated. The high potassium over sodium reflects the enrichment of potassium over sodium in their sources (Foley and Peccerillo 1992). And these rocks are all also rich in CO_2, which indicates that the source of potassium may be K_2CO_3.

References

Anderson, D.L. (2007) New Theory of the Earth. Cambridge University Press , New York. ISBN 9780521849593

Baba, K., Tarits, P., Chave, A.D., Evan, R.L. Hirth, G., and Mackie, R.L. (2006) Electrical structure beneath the northern MELT line on the East Pacific Rise at 15°45'S. Geophysical Research Letters, 33, L22301.

Bercovici, D., and Karato, S. (2003) Whole mantle convection and transition-zone water filter. Nature, 425, 39-44.

Boulard, E., Pan, D., Galli, G. Liu, Z., and Wendy, W.L. (2015) Tetrahedrally coordinated carbonates in Earth's lower mantle. Nature Communications, 6, 6311.

Buob, A., Luth, R.W., Schmidt, M.W., and Ulmer, P. (2006) Experiments on $CaCO_3$–$MgCO_3$ solid solutions at high pressure and temperature. American Mineralogist, 91, 435–440.

Cancarevic, Z.P., Schon, J.C. and Jansen, M. (2007) Possible existence of alkali metal orthocarbonates at high pressure. Chemistry – A European Journal, 13, 7330–7348.

Foley, S. and Peccerillo, A. (1992) Potassic and ultrapotassic magmas and their origin. Lithos, 28,181-185.

Gaillard, F., Malki, M., Iacono-Marziano, G., Pichavant, M. and Scaillet, B. (2008) Carbonatite melts and electrical conductivity in the asthenosphere. Science, 322, 1363–1365.

Ghiorso M.S., Hirschmann, M.M, Reiners, P.W., and Kress, V.V. III (2002) The pMELTS: A revision of MELTS for improved calculation of phase relations and major element partitioning related to partial melting of the mantle to 3 GPa. Geochemistry Geophysics Geosystems, 3, 10.1029/2001GC000217.

Hirao, N., Ohtani, E., Kondo, T., Sakai, T., and Kikegawa, T. (2007) Hollandite II phase in $KAlSi_3O_8$ as a potential host mineral of potassium in the Earth's lower mantle. Physics of the Earth and Planetary Interiors, 166, 97-104.

Katsura, T., and Ito, E. (1990) Melting and subsolidus phase relations in the $MgSiO_3$-$MgCO_3$ system at high pressures – Implications to evolution of the Earth's atmosphere. Earth and Planetary Science Letters, 99, 110-117.

Oganov, A.R., Hemley, R.J., Hazen, R.M., and Jones, A.P. (2013) Structure, bonding and mineralogy of carbon at extreme conditions. Reviews in Mineralogy & Geochemistry, 75, 47-77.

Ritsema, J. van Heijst, H.J., Deuss, A., and Woodhouse, J.H. (2011) S40RTS: a degree-40 shear-velocity model for the mantle from new Rayleigh wave dispersion, teleseismic traveltimes, and normal-mode splitting function measurements, Geophysical Journal International, 184, 1223-1236.

Schmandt, B., Jacobsen, S.D. and Becker, T.W. and Liu, Z., and Dueker, K.G. (2014) Dehydration melting at the top of the lower mantle. Science, 344, 1265-1268.

Shatskiy, A., Gavryushkin, P.N., Sharygin, I.S., Litasov, K.D., Kupriyanov, I.N., Higo, Y., Borzdov, Y.M., Funakoshi, K., Palyanov, Y.N., Ohtani, E. (2013a) Melting and subsolidus phase relations in the system Na_2CO_3–$MgCO_3$±H_2O at 6 GPa and the stability of $Na_2Mg(CO_3)_2$ in the upper mantle. American Mineralogist, 98, 2172–2182.

Shatskiy, A., Sharygin, I.S., Gavryushkin, P.N., Litasov, K.D., Borzdov, Y.M., Shcherbakova, A.V., Higo, Y., Funakoshi, K., Palyanov, Y.N., and Ohtani, E. (2013b) The system K_2CO_3–$MgCO_3$ at 6 GPa and 900–1450 °C. American Mineralogist, 98, 1593–1603.

Tao, R., Fei, Y., and Zhang, L. (2013) Experimental determination of siderite stability at high pressure. American Mineralogist, 98, 1565-1572.

Wang, Y., Sakamaki, T., Skinner, L.B., Jing, Z.,Yu, T., Kono, Y., Park, C., Shen, G., Rivers, M.L. and Sutton, S.R. (2014) Atomistic insight into viscosity and density of silicate melts under pressure. Nature Communications, 5, 3241.